Numerical Investigation of Vertical-Axis Wind Turbines at Low Reynolds Number

Thesis by

Hsieh-Chen Tsai

In Partial Fulfillment of the Requirements

for the Degree of

Doctor of Philosophy

Caltech

California Institute of Technology

Pasadena, California

2016

(Defended April 18, 2016)

Acknowledgements

I would like to first thank my advisor, Professor Tim Colonius, for his support and teachings over the past six years. I am inspired by his passion for research and sharp eyes for analyzing flow physics. I have enjoyed my brief time in the Colonius group. My research experience would not have been this fruitful without the help from my laboratory members, especially, Sebastian Liska and Jeesoon Choi, for their helpful comments on programming and interesting thought on my research. It's been an honor and a privilege working with you.

I would also like to thank Professors John Dabiri, Beverley McKeon, and Guillaume Blanquart for serving on my committee, reviewing my thesis, and providing their insight on my work. I am also fortunate to have collaborated with Reeve Dunne and Daniel Araya. They have provided interesting challenges and insight in this thesis and I truly enjoyed the moments discussing research with them. Furthermore, I would like to acknowledge that this study was financially supported by the Gordon and Betty Moore Foundation (No. GBMF2645).

To my Taiwanese friends in Association of Caltech Taiwanese, especially, Ho-Cheng Tsai, Wen-Hao Lee, and Kuang-Wei Yang, who started with me in 2010, I cannot thank you enough for your friendship. Furthermore I would like to thank Yu-Hung Lai. You have made my life at Caltech enjoyable and unforgettable. I cannot mention everyone here but I am thankful to all of those who have influenced me during my years at Caltech.

I would like to thank my parents, Po-Wen Tsai and Yu-Chen Tsai Sung, and my brother, Hsieh-Fu Tsai. I would not been able to come this far without your love, care, and tireless support.

Finally, I owe more than I can express to my wife, Hsian Han (Sandy) Hwang, for her unconditional love. I am indebted to Sandy for her moving from Taiwan to Los Angeles to offer me warm

support. To Sandy, thank you for bringing me joy, standing by me, and encouraging me. I cherish the time with you and look forward to our new life in Taiwan.

Abstract

This thesis is aimed at numerically investigating the aerodynamics and the starting of a vertical-axis wind turbine at low Reynolds number using the immersed boundary method. The influence of the Coriolis effect on dynamic stall is isolated by comparing the rotating airfoil to one undergoing an equivalent planar motion that is composed of surging and pitching motions that produce an equivalent speed and angle of attack variation over a cycle. At lower tip-speed ratios, the Coriolis force leads to the capture of a vortex pair which results in a significant decrease in lift when the angle of attack of a rotating airfoil begins to decrease in the upwind half cycle. In the absence of the wake-capturing, the equivalent planar motion is a good approximation to a rotating blade in a vertical-axis wind turbine.

Analysis on the starting torque shows that when the turbine solidity is lower than about 0.5, the starting torque distribution can be well-modeled by considering a single blade at different orientations, and starting torque distributions for multi-bladed turbines can be constructed by linearly combining the torques at the respective positions of the blades. Using this model, optimal configurations to start a multi-bladed low-solidity vertical-axis wind turbine is proposed.

A preliminary study is made to determine an optimal blade pitch for a single-bladed motor-driven turbine using optimal control theory. When the input power is minimized directly, the solution seems to converge to only a local minimum due to a lower input power reduction than that obtained by maximizing the mean tangential force. After a transient, both controls converge to time-invariant pitch angles of about the same magnitude but with opposite signs. The wake-capturing phenomenon observed in the uncontrolled case necessitates large input power. Under active control, the disappearance of wake-capturing and attendant changes in the flow field collectively result in a

reduction of required input power.

Contents

List of Figures

List of Tables

Nomenclature

a	vector formed by the controlled variables
A	mass matrix with implicit velocity term
B	rotation matrix
bc_1	boundary terms in the discretized momentum equation
bc_2	boundary terms in the discretized continuity equation
bc_γ	boundary terms in the discretized vorticity equation
c	airfoil chord length
C	discrete curl operator
C_D	drag coefficient
C_L	lift coefficient
C_M	moment coefficient
C_P	power coefficient
C_T	tangential force coefficient
C_μ	momentum coefficient of the actuator, $((\bar{u}_{\text{jet}}^2 \Delta x)/(\frac{1}{2} U_\infty^2 c))$
$d(r)$	discrete delta function
d_{ctrl}	distance multiplied to the control gradient
D	discrete divergence operator
E	interpolation operator
$E(m)$	the complete elliptic integral of the second kind, $(E(m) = \int_0^{\pi/2} \sqrt{1 - m^2 \sin^2 \theta}\ d\theta)$
f_{bf}	force exerted by the body on the fluid
f_{fb}	force exerted by the fluid on the body $(f_{fb} = -f_{bf})$

f_i	integrand of the cost function
F	friction coefficient
F_D	drag
F_L	lift
F_N	normal force
F_T	tangential force
G	discrete gradient operator
H	regularization operator
I	identity matrix
I_O	moment of inertia of the blade about point O
k	reduced frequency, $(\Omega c/(2U_\infty) = \lambda/(2\ell))$
L	discrete (vector) Laplacian
n_b	number of points of a body
$N(q, \gamma)$	the discrete nonlinear term $(N(q, \gamma) = q \times \gamma)$
N_b	number of blades
N_g	number of the grid levels
p	pressure
p_∞	static pressure at infinity
$P^{(k+1) \to (k)}$	boundary value interpolation operator from $(k+1)$th-level to kth-level
q	discrete velocity flux
q_a	discrete velocity flux of $\mathbf{u}_a(\mathbf{x}, t)$
$q_{a,s}$	discrete velocity flux of $\mathbf{u}_a(\mathbf{x}_s, t)$
q_U	discrete velocity flux of $\mathbf{u}_U(t)$
q_Ω	discrete velocity flux of $\mathbf{u}_\Omega(\mathbf{x}_r, t)$
$q_{\Omega,s}$	discrete velocity flux of $\mathbf{u}_\Omega(\mathbf{x}_s, t)$
r	right-hand side of the discretized governing equations
R	radius of the turbine

$\mathbf{R}(t)$	distance between the Newtonian frame and the rotating frame
Re	Reynolds Number, $(U_\infty c/\nu)$
Ro	Rossby Number, $(U_\infty/(2\Omega c) = \ell/(2\lambda))$
S	discrete Fourier sine transform matrix
$\tilde{S}$	integration matrix
t	time
T	period of the rotation of VAWT
T_H	control horizon
$\mathbf{u}$	velocity of the fluid
$\mathbf{u}_a$	relative velocity of the rotating frame to the inertial frame$(\mathbf{u}_a = \mathbf{u}_U + \sum_i \mathbf{u}_{\Omega_i})$
$\mathbf{u}_U$	relative velocity of the rotating frame due to translation
$\mathbf{u}_\Omega$	relative velocity of the rotating frame due to rotation
$\bar{u}_{\mathrm{jet}}$	average velocity of the jet injected by the actuator
$\mathbf{U}(t)$	translational velocity between the Newtonian frame and the rotating frame
U_∞	freestream velocity
W	incoming velocity
$\mathbf{x}$	position vector of the Eulerian grid
$\mathbf{x}_s$	position vector of the body
z	distance from the discrete delta function center
α	angle of attack
β	constant in the discrete (vector) Laplacian
δ	Dirac delta function
δ_{ij}	Kronecker delta
γ	discrete circulation in each dual cell
λ	tip-speed ratio
ν	fluid kinematic viscosity
ρ	fluid density

ρ_b	density field of the blade
ϕ_ρ	density ratio (ρ_s/ρ)
σ	solidity, $((N_b\,c)/(2\pi R))$
θ	azimuthal angle
θ_0	initial azimuthal angle for starting
τ	backward running time $(\tau = T_H - t)$
τ_{fb_j}	torque exerted by the fluid on the body about O_j
τ_{m_j}	torque exerted by the motor on O_j
τ_L	torque generated by a load
τ'_j	dummy torque exerted on O_j
$\boldsymbol{\omega}$	vorticity of the fluid
ΔF	difference of calculated forces to the targeted value
Δs	Lagrangian grid spacing
Δt	time step
Δx	Eulerian grid spacing
Δz	the cell width of the staggered grid in the z-direction
Λ	diagonal matrix with eigenvalues of discrete Laplacian
Ω	angular velocity of the turbine
ψ	static pitch angle
Π	modified pressure
ℓ	ratio of the radius of the turbine to the chord length, (R/c)
$\mathcal{J}$	cost function
$\mathcal{F}$	integrand of the cost function
$\mathcal{H}$	Hamiltonian of the PDE-constrained optimization problem
$\mathcal{L}$	Lagrangian of the PDE-constrained optimization problem

Subscripts

avg	average velocity
n	vectors or operators in the Newtonian frame
g	vectors or operators in the blade-fixed rotating frame of reference
inst	instantaneous velocity
max	maximum
opt	optimal value
r	vectors or operators in the vawt-fixed rotating frame of reference
ref	reference (targeted) value
rel	relative value
sin	sinusoidal variation
surge	surge velocity
EPM	the equivalent planar motion
SPM	the sinusoidal pitching motion
SSPM	the sinusoidal surging-pitching motion
VAWT	vertical axis wind turbine

Superscripts

n	discrete variables at $t = t^n$
T	transpose of the matrix
(k)	discrete variables in the k th-level
$[p]$	discrete variables in the p th-iteration
†	adjoint variables

Chapter 1

Introduction

1.1 Motivation

Over the last decade, the desire to address the issue of climate change and global warming has made flow energy harvesting an active research topic. Our interest here is in the H-rotor Darrieus wind turbine, which is also called vertical-axis wind turbines (VAWT). Kirke (1998) and Pawsey (2002) have summarized the relative strengths and weaknesses of VAWT and horizontal-axis wind turbines (HAWT). VAWT have several interesting features: their low sound emission (a consequence of their operation at lower tip speed ratios), their insensitivity to wind direction (because they are omnidirectional), their high accessibility (because the generator can be placed on the ground), and their increased power output in skewed flow (Mertens et al., 2003; Ferreira et al., 2006). However, VAWT suffer disadvantages like a lower-efficiency than comparable HAWT, and they can be difficult to start (Kirke, 1998). Despite the low efficiency of individual VAWT, Dabiri (2011) and Kinzel et al. (2012) showed that an array of counter-rotating VAWT can achieve higher power output per unit land area and a shorter velocity recovery distance than existing wind farms consisting of HAWT. Araya et al. (2014) developed a low-order model of the mean flow through an array of VAWT using leaky Rankine bodies. The model correctly predicts the ranking of array performances to within statistical uncertainty with significantly less computational expense and therefore provides an efficient tool to find the optimal turbine array configurations. In this thesis, we are interested in numerically investigating the aerodynamics and the starting of a VAWT in order to improve the

efficiency and self-starting capability of a VAWT.

In many computational studies of VAWT, simulations of parametric studies and the starting of a VAWT have been done with steady/unsteady Reynolds-averaged Navier-Stokes (RANS/URANS) and large-eddy simulation (LES) at Reynolds numbers of $O(10^5 - 10^6)$. Reynolds number is scaled by the chord length of the blade and the freestream velocity. Hansen and Sresen (2001) and Nobile et al. (2011) investigated flows around a multi-bladed 2D VAWT at $Re \sim O(10^5)$ using RANS with various turbulence models. Duraisamy and Lakshminarayan (2014) and Bremseth and Duraisamy (2016) numerically analyzed the performance of isolated, pairs, columns, and arrays of VAWT using RANS at $Re = 67000$. However, although RANS and URANS are able to solve for flow at such a high Reynolds number, they suffer from inaccuracies for separated flow and unknown modeling errors for turbulence (Alfonsi, 2009). LES is a good choice for simulating three-dimensional and separated flow at such a high Reynolds number. Ferreira et al. (2007) simulated dynamic stall in a section of a VAWT using LES and detached-eddy simulation (DES) at $Re = 50,000$ and validated the results by comparing the vorticity in the rotor area with particle image velocimetry (PIV) data. Barsky et al. (2014) investigated the fundamental wake structure of a single VAWT computationally by LES and experimentally by PIV. However, studies using LES are only with limited parameter space because of computational expense. In this thesis, flows around a VAWT are simulated using direct numerical simulation (DNS), which solves the incompressible Navier-Stokes equations directly without any models. However, in order to explore a comparatively large region of parametric space in relatively short computational time, flows are restricted to low Reynolds numbers, $Re \sim O(10^3)$, and to a two-dimensional cross section of an otherwise planar turbine geometry. Nevertheless, at the expense of studying a sub-scale regime, where the physics are thought to be qualitatively similar to full-scale regime (Choi et al., 2015), the computational expense is relatively inexpensive. As we will discuss in section 3.5, comparisons with experiments at high Reynolds numbers show qualitative agreement, but a precise accounting for three-dimensional effects awaits future simulations.

Many researchers have shown that motions of a wing such as pitching, surging, and plunging can be combined to harvest energy in a flow (Lissaman, 2005; Langelaan, 2009; Zhu and Peng, 2009;

Zhu, 2011; Peng and Zhu, 2009; Williams et al., 2011). Energy is extracted from the work done by aerodynamic forces generated by the unsteady flow past around the wing. Since the flow experienced by the blades of a VAWT is inherently unsteady, we are interested in taking advantage of this unsteady flow and maximizing the power output of a VAWT through the pitching motion of the blades. For example, engineers at Brown University inspired by bat's flight designed a device to generate power from the tides. The device contains flat, rigid wings which are allowed to pivot and move along the vertical axis. When water flows over the wings, they oscillate perpendicularly to the flow, and generate electricity. Furthermore, the device was made more efficient by controlling the pitch angle of the wing. However, designing the motion of the wing to maximize the power generation is presently done by a time-consuming and sub-optimal trial-and-error process. Therefore, we propose to find an optimal motion that maximizes the power output using optimization technique. The proposed optimization procedure will also provide a mathematically rigorous, systematic approach to design efficient devices for energy harvesting in the future.

1.2   Aerodynamics of VAWT

The aerodynamics of VAWT are complicated by the inherently unsteady flow produced by the large variations in both angle of attack and incident velocity magnitude of the blades, which can be characterized as a function of the tip-speed ratio. Typically, commercial VAWT operate at a tip-speed ratio around 2 to 5 (Kirke, 1998), which produces an angle of attack variation from $11.5°$ to $30°$ and an incident velocity variation with an amplitude of 21.5% to 49% of its mean. Due to large variations in the angle of attack, dynamic stall has been found to occur on VAWT blades at low tip speed ratios (Ferreira et al., 2009). Dynamic stall refers to the delay in the stall of airfoils that are rapidly pitched beyond the static stall angle, and is associated with a substantially higher lift than is obtained quasi-statically. Dynamic stall has been an active research topic in fluid dynamics for more than 60 years, largely because of the helicopter applications (Corke and Thomas, 2015). Several attempts have been made to model dynamic stall in a VAWT (Paraschivoiu and Allet, 1988; Paraschivoiu and Beguier, 1998; Allet et al., 1999) and the results have demonstrated success of

accurately predicting the aerodynamic load of a VAWT.

When dynamic stall in the context of VAWT is investigated using PIV, due to the rotational nature of the problem and the static field of view in PIV measurement, the experimentally visualized flow field is always partially obstructed or shadowed as the turbine blades rotate about the axis. In order to circumvent this issue, Wang et al. (2010) introduced a simplified model of an airfoil undergoing an equivalent planar motion, which is composed of a surging and pitching motion that produces an equivalent speed and angle-of-attack variation over the cycle. They further simplified the equivalent planar motion to a sinusoidal pitching motion to investigate dynamic stall in a 2D VAWT numerically. The results obtained using URANS matched the experiments done by Lee and Gerontakos (2004), where flow over an oscillating airfoil was investigated. More recently, Dunne and McKeon (2014, 2015a,b) experimentally investigated the separated flow over a sinusoidally pitching and surging airfoil at $Re = 10^5$ and proposed a low-order model of dynamic stall using dynamic mode decomposition. The physics of dynamic stall was successfully captured with the interaction between the primary and secondary dynamic separation mode identified by the model.

However, the simplified model proposed by Wang et al. lacks the appropriate forces needed to account for the non-inertial reference frame, which are the forces associated with angular acceleration, the Coriolis force, and the centrifugal force. Forces associated with angular acceleration do not depend on the fluid velocity and can be ignored by fixing the angular velocity. The centrifugal force, which is also independent of fluid velocity, only changes the pressure field in the radial direction. Only the Coriolis force depends on the fluid velocity and can locally affect the dynamic stall. Therefore, in this thesis, we focus on investigating the effect of the Coriolis force to the dynamic stall. The differences between the simplified model and VAWT will be discussed in more detail in Chapter 3.

1.3 Self-starting of a VAWT

The difficulties associated with self starting of a VAWT are well known (Baker, 1983; Kirke, 1998; Pawsey, 2002; Hill et al., 2009). Kirke (1998) have stated that the self-starting of VAWT is possible

with a careful selection of blade geometry. Dominy et al. (2007) experimentally showed that a three-bladed VAWT can self-start even using fixed-geometry, symmetric airfoils, but that two-bladed designs can only self-start under particular conditions. Hill et al. (2009) experimentally investigated the starting of VAWT at $Re \approx 5 \times 10^5$ and discussed the physics of self-starting through a simple numerical model. Untaroiu et al. (2011) numerically investigated the self-starting capability of VAWT using URANS at $Re \approx 5 \times 10^5$. The method has been demonstrated to predict terminal operating speed within 12% of the measured value. However, the turbine performance during the starting, which is important to the study of self-starting problems, was not accurately captured due to the lack of near-wall and transitional turbulence models.

Several solutions to the starting issue have been suggested regarding the design of the blade. Baker (1983) recommended several blade designs for VAWT that are favorable for self-starting. Beri and Yao (2011a,b) numerically investigated the self-starting of VAWT with cambered airfoils and airfoils with modified trailing edge. They showed that the VAWT with cambered airfoils has potential to self-start with reduced coefficient of power and the VAWT with tailing-edge-modified airfoils has better performance in self-starting at lower tip-speed ratios with normal coefficient of power. Chen and Kuo (2013) studied the effects of pitch angle and blade camber on the self-starting. The results show that the maximum root-mean-square moment occurs at a pitch angle equal to 5° outward from the tangential direction for all the blades examined. Moreover, blades with appropriate camber generate a higher root-mean-square moment at all pitch angles.

1.4 Flow control on vertical axis wind turbine

Flow control has been an active research topic in reducing bluff-body form drag and wake fluctuations by suppressing flow instabilities and preventing flow separation. Choi et al. (2008) reviewed some of the most important and successful approaches. Usually, flow control strategies are categorized into *passive* and *active* methods. Passive methods, such as splitter plates (Anderson and Szewczyk, 1997) and the deliberate arrangement of fixed rigid bodies (Michael et al., 1994; Strykowski and Sreenivasan, 1990), do not require an energy input, and active methods, such as body rotation

(Tokumaru and Dimotakis, 1991), cross-flow body displacement (Siegel et al., 2006), and synthetic jets, do. Early studies on post-stall flow control focused on *open-loop* active control (Greenblatt and Wygnanski, 2000; Glezer and Amitay, 2002; Raju et al., 2008), which does not use feedback to determine if the desired goal has been achieved. More recently, there has been an increasing interest in *closed-loop* active control, which modifies the behavior of actuation based on the real time information from the flow. The closed-loop active control has the potential to stabilize a system about an unstable operating condition so that only a small amount of energy input is required after transients (Pinier et al., 2007; Ahuja and Rowley, 2010; Taira et al., 2010). The feedback control approach used in this thesis is adjoint-based optimal control, which finds the control that locally minimizes a cost function over a given time horizon. The fact that adjoint-based optimal control does not require an a priori knowledge of the physical mechanism that will minimize the cost function (Joe et al., 2010; Flinois and Colonius, 2015) makes the optimal control useful in discovering unsuspected but effective control strategies.

Most of the passive control methods on VAWT concern subtle changes to the design of the VAWT, such as blade profile (e.g., thickness and camber)(Roh and Kang, 2013; Chen and Kuo, 2013), blade fixed pitch angle (Fiedler and Tullis, 2009; Chen and Kuo, 2013), and blade offset (Fiedler and Tullis, 2009). The improvement in power generation using the passive control methods is usually about 10% to 15%. On the other hand, active control methods are difficult to implement on VAWT but it can be more effective in enhancing the performance. Hwang et al. (2006) adopted two variable pitch systems, namely the cycloidal blade system and the individual active blade control system, to improve the performance of the power generation of a 1kW class VAWT. First, the cycloidal blade system changes the pitch angle and phase based on the cycloidal motion according to changes in wind speed and wind direction. The corresponding power generation is improved by about 30% compared to fixed-pitch VAWT. Second, the individual active blade control system is shown to be more effective in enhancing performance. This system pitches each blade with a optimal motion obtained by maximizing the tangential force at the position of that blade. The corresponding improvement in power generation is 60%.

Several control strategies were implemented. Paraschivoiu et al. (2009) obtained the optimal variation of the blades' pitch angle of a 7kW VAWT using the CARDAAV code. The code is based on the *Double-Multiple Stream* tube model and is coupled with a genetic algorithm optimizer. A gain of almost 30% in the power production was reported. Greenblatt et al. (2013) used pulsed dielectric barrier discharge plasma actuators in a feed-forward configuration to control the dynamic stall on a double-bladed VAWT. A net power increase of 10% was achieved and there is a potential for a even greater improvement with more powerful plasma actuation.

1.5 Outline of this thesis and the resulting publications

This thesis is aimed at numerically investigating the two-dimensional incompressible flow around a VAWT to provide insight into the aerodynamics of a VAWT, the mechanism of the starting of a VAWT, and the potential to apply a control to enhance the efficiency of a VAWT.

In Chapter 2, we derive the mathematical formulation, introduce numerical algorithms, and describe procedures of optimal control that are used in this thesis.

In Chapter 3, we investigate the differences between VAWT and the equivalent planar motion proposed by Wang et al. (2010). In particular, we investigate the effect of the Coriolis force on dynamic stall. Airfoils undergoing a sinusoidal pitching motion and a sinusoidal surging-pitching motion are also computed and compared to the full VAWT and equivalent planar motions. The effect of solidity on the wake of VAWT has been investigated by collaborators Araya and Dabiri in Araya (2016). The effect of tip-speed ratio, Reynolds number, and Rossby number on dynamic stall is discussed in Chapter 3. Moreover, comparisons are made with the water-tunnel experiments performed by collaborators Dunne and McKeon (2014, 2015a,b) in Dunne et al. (2015) to further investigate the effect of the rotating frame, Reynolds number, and the Coriolis force. Based on these works, the following archival papers have been written:

- Tsai, H.-C. and Colonius, T. (2014). Coriolis effect on dynamic stall in a vertical axis wind turbine at moderate Reynolds number. In *32nd AIAA Applied Aerodynamics Conference,*

Atlanta, GA. AIAA paper 2014-3140

- Tsai, H.-C. and Colonius, T. (2016). Coriolis effect on dynamic stall in a vertical axis wind turbine. *AIAA Journal*, 54(1):216-226.

- Dunne, R., Tsai, H.-C., Colonius, T., and McKeon, B. J. (2015). Leading edge vortex development on pitching and surging airfoils: A study of vertical axis wind turbines. In *Int. Conf. Wake Jets Separated Flows, Stockholm, Sweden.*

In Chapter 4, we investigate the starting capability of a VAWT. A simple quasi-steady model is proposed to analyze the starting torque of a multi-bladed VAWT. Moreover, the comparisons between a flow-driven VAWT after self-starting and a motor-driven VAWT are discussed. Moreover, comparisons of flow-driven and motor-driven VAWT are made with the water-tunnel experiments performed by collaborators Araya and Dabiri (2015) to validate the load model. These studies are documented in the following reference paper which will also be submitted to an archival journal in the near future:

- Tsai, H.-C. and Colonius, T. (2016). Numerical investigation of self-starting capability of vertical-axis wind turbines at low Reynolds numbers. In *34th AIAA Applied Aerodynamics Conference, Washington, D.C.* (Accepted)

In Chapter 5, we investigate the optimal control of time-dependent blade pitch of a motor-driven single-bladed VAWT to minimize the input power as a preliminary study to enhance the efficiency of VAWT.

Finally, we conclude and discuss about future works in Chapter 6.

Chapter 2

Mathematical formulation and numerical methods

In this chapter, we derive an alternative form of the incompressible Navier-Stokes equations in the non-inertial frame, which is used to solve for the flow in the airfoil-fixed frame. The fast immersed boundary projection method is then introduced to simulate the two-dimensional incompressible flow around a VAWT. In order to study the flow-structure interaction in the starting of a VAWT, we introduce a predictor-corrector method to couple the equation of the motion of a VAWT to the incompressible Navier-Stokes equations. Finally, adjoint equations are derived and procedures for optimal control are discussed.

2.1 Alternative form of the incompressible Navier-Stokes equations in the non-inertial frame

Kim and Choi (2006) developed an immersed boundary method in a non-inertial reference frame that is fixed to the body. The Navier-Stokes equations is formulated in a conservative form such that the force terms due to the rotation and the translational and rotational accelerations are included in the nonlinear term. Following the same approach, we derive an alternative form of the incompressible Navier-Stokes equations in the non-inertial reference frame in this section.

We consider incompressible flows external to a rigid wing (figure 2.1) undergoing arbitrary motion. In this analysis, the motion of the accelerating wing is simplified to a unsteady translation with

velocity $\mathbf{U}(t)$ and a rotation with angular velocity $\mathbf{\Omega(t)}$ about a point O. $\boldsymbol{x}_s$ are the coordinates of the points on the surface of the body. The subscripts n and r denote variables or differentiations in the Newtonian inertial frame and the rotating frame, respectively.
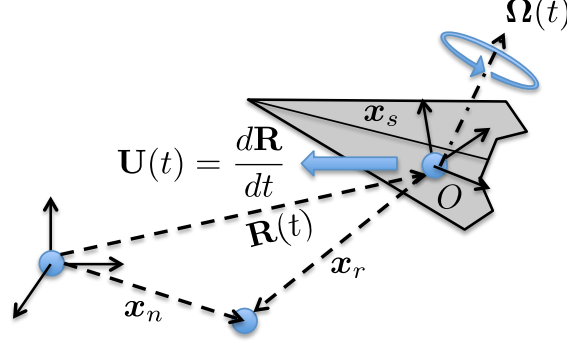
Figure 2.1: Rotating coordinates for accelerating wing.

With the relation of the time differentiation in the Newtonian frame and the rotating frame,

$$\left(\frac{d(\cdot)}{dt}\right)_n = \left(\frac{d(\cdot)}{dt}\right)_r + \mathbf{\Omega}(t) \times (\cdot) \ ,$$

the relations of the position, velocity, and acceleration vectors between two coordinates can be derived in the following:

$$\mathbf{x}_n = \mathbf{x}_r + \mathbf{R}(t) \ , \tag{2.1}$$

$$\mathbf{u}_n = \mathbf{u}_r + \mathbf{\Omega}(t) \times \mathbf{x}_r + \mathbf{U}_n(t) \ , \tag{2.2}$$

$$\mathbf{a}_n = \mathbf{a}_r + \left(\frac{d\mathbf{\Omega}}{dt}(t)\right)_r \times \mathbf{x}_r + 2\mathbf{\Omega}(t) \times \mathbf{u}_r + \mathbf{\Omega}(t) \times (\mathbf{\Omega}(t) \times \mathbf{x}_r)$$
$$+ \left(\frac{d\mathbf{U}_n}{dt}(t)\right)_r + \mathbf{\Omega}(t) \times \mathbf{U}_n(t) \ , \tag{2.3}$$

where $\mathbf{U}_n(t) = \left(\frac{d\mathbf{R}}{dt}(t)\right)_n$ is the velocity of the moving frame relative to the Newtonian frame.

By taking the curl of equation (2.2), we obtain the relation of the vorticity fields between two coordinates:

$$\boldsymbol{\omega}_n = \boldsymbol{\omega}_r + 2\mathbf{\Omega}(t) \ . \tag{2.4}$$

Therefore the dimensionless Navier-Stokes equations in the non-inertial frame become

$$\left(\frac{\partial \mathbf{u}_r}{\partial t}\right)_r + (\mathbf{u}_r \cdot \nabla)\,\mathbf{u}_r = -\nabla p + \frac{1}{Re}\nabla^2 \mathbf{u}_r - \left(\frac{d\mathbf{\Omega}}{dt}(t)\right)_r \times \mathbf{x}_r - 2\mathbf{\Omega}(t) \times \mathbf{u}_r$$

$$- \mathbf{\Omega}(t) \times (\mathbf{\Omega}(t) \times \mathbf{x}_r) - \left(\frac{d\mathbf{U}_n}{dt}\right)_r - \mathbf{\Omega}(t) \times \mathbf{U}_n(t) \ . \tag{2.5}$$

The boundary conditions for equation (2.5) are

$$\begin{cases} \mathbf{u}_r \longrightarrow -\mathbf{U}_n(t) - \mathbf{\Omega}(t) \times \mathbf{x}_r \\[2mm] \boldsymbol{\omega}_r \longrightarrow -2\mathbf{\Omega}(t) \qquad\qquad \text{as } |\mathbf{x}_r| \longrightarrow \infty \\[2mm] p \longrightarrow p_\infty \end{cases} \tag{2.6}$$

$$\mathbf{u}_r = 0 \qquad\qquad \text{on the surface of the body, i.e., } \mathbf{x}_r = \mathbf{x}_s \ .$$

Note that $\mathbf{\Omega}(t) \times (\mathbf{\Omega}(t) \times \mathbf{x}_r) = -\nabla(\frac{1}{2}\,|\mathbf{\Omega}(t) \times \mathbf{x}_r|^2)$ and $\mathbf{\Omega}(t) \times \mathbf{U}_n(t) = -\nabla\,[(\mathbf{\Omega}(t) \times \mathbf{x}_r) \cdot \mathbf{U}_n(t)]$.

We apply the following vector calculus identities and the incompressibility condition:

$$\mathbf{u}_r \cdot \nabla \mathbf{u}_r = \nabla\left(\frac{1}{2}|\mathbf{u}_r|^2\right) - \mathbf{u}_r \times (\nabla \times \mathbf{u}_r) = \nabla\left(\frac{1}{2}|\mathbf{u}_r|^2\right) - \mathbf{u}_r \times \boldsymbol{\omega}_r \ , \tag{2.7}$$

$$\nabla^2 \mathbf{u}_r = \nabla\,(\nabla \cdot \mathbf{u}_r) - \nabla \times (\nabla \times \mathbf{u}_r) = -\nabla \times \boldsymbol{\omega}_r = -\nabla \times \boldsymbol{\omega}_n \ . \tag{2.8}$$

Equation (2.5) becomes

$$\left(\frac{\partial \mathbf{u}_n}{\partial t}\right)_r = -\nabla\Pi + (\mathbf{u}_n - \mathbf{u}_a(\mathbf{x}_r,t)) \times \boldsymbol{\omega}_n - \frac{1}{Re}\nabla \times \boldsymbol{\omega}_n \ , \tag{2.9}$$

where $\mathbf{u}_a(\mathbf{x}_r,t)$ is the relative velocity of the point in the non-inertial frame to the inertial (laboratory) frame:

$$\mathbf{u}_a(\mathbf{x}_r,t) = \mathbf{u}_U(t) + \mathbf{u}_\Omega(\mathbf{x}_r,t) \ , \tag{2.10}$$

$\mathbf{u}_U(t) = \mathbf{U}_n(t)$ is the relative velocity due to translation, $\mathbf{u}_\Omega(\mathbf{x}_r,t) = \mathbf{\Omega}(t) \times \mathbf{x}_r$ is the relative velocity

due to rotation, and Π is a modified pressure given by

$$\Pi = p + \frac{1}{2}|\mathbf{u}_n - \mathbf{u}_a(\mathbf{x}_r, t)|^2 - \frac{1}{2}|\mathbf{u}_a(\mathbf{x}_r, t)|^2 \ . \tag{2.11}$$

The boundary conditions become

$$\begin{cases} \mathbf{u}_n \longrightarrow 0 \\[2ex] \boldsymbol{\omega}_n \longrightarrow 0 \qquad \text{as } |\mathbf{x}_r| \longrightarrow \infty \\[2ex] \Pi \longrightarrow p_\infty \end{cases} \tag{2.12}$$

$$\mathbf{u}_n = \mathbf{u}_a(\mathbf{x}_s, t) \quad \text{on the surface of the body, i.e., } \mathbf{x}_r = \mathbf{x}_s \ .$$

Note that equations (2.9) and (2.12) are not the standard accelerating-frame form of the variables and equations, but are computationally convenient because they render the governing equations free from body forces, and because the dependent variables decay at infinity. The price for this simplicity is that we must now impose a time-dependent velocity at each point along the immersed surface. Fortunately, this velocity can be readily imposed in the immersed boundary method. Moreover, we can easily extend the alternative form of the non-inertial, incompressible Navier-Stokes equations to two successively rotating frames as illustrated in Appendix A.

2.2 Fast immersed boundary projection method using multi-domain far-field boundary conditions

In this study, the immersed boundary method introduced by Peskin (1972) is used to simulate two-dimensional incompressible flow around a rotating body. The alternative form of the incompressible Navier-Stokes equations in the non-inertial frame, equation (2.9), with the immersed boundary force

term and the corresponding boundary conditions, equation (2.12), are given by

$$\left(\frac{\partial \mathbf{u}_n}{\partial t}\right)_r = -\nabla\pi + (\mathbf{u}_n - \mathbf{u}_a(\mathbf{x}_r, t)) \times \boldsymbol{\omega}_n - \frac{1}{Re}\nabla \times \boldsymbol{\omega}_n + \int_s f_{bf}(\mathbf{x}_s(s))\delta(\mathbf{x}_s(s) - \mathbf{x}_r)ds \ , \quad (2.13)$$

$$\nabla \cdot \mathbf{u}_n = 0 \ , \quad (2.14)$$

$$\int_{\mathbf{x}_r} \mathbf{u}_n(\mathbf{x}, t)\delta(\mathbf{x} - \mathbf{x}_s(t))d\mathbf{x} = \mathbf{u}_a(\mathbf{x}_s, t) \ . \quad (2.15)$$

The spatial and temporal discretization of equations (2.13), (2.14), and (2.15) follows from Taira and Colonius (2007). The discrete equations are first formulated spatially on a formally unbounded staggered Cartesian grid with equal grid spacing. The temporal discretization uses the implicit Crank-Nicolson integration for the viscous terms and the explicit second-order Adams-Bashforth scheme for the convective terms. This produces an algebraic system of equations,

$$\begin{bmatrix} A & G & -H \\ D & 0 & 0 \\ E & 0 & 0 \end{bmatrix} \begin{pmatrix} q^{n+1} \\ \pi \\ f_{bf} \end{pmatrix} = \begin{pmatrix} r^n \\ 0 \\ q_{a,s}^{n+1} \end{pmatrix} + \begin{pmatrix} bc_1 \\ bc_2 \\ 0 \end{pmatrix} , \quad (2.16)$$

where q is the discretized velocity flux, π is the discretized modified pressure vectors, and f_{bf} is the force that body exerts on the fluid. It has the same magnitude but the opposite direction of the force that fluid exerts on the body, i.e., $f_{fb} = -f_{bf}$. Moreover, q_a, q_U, and q_{Ω_i} are the discretized velocity fluxes of $\mathbf{u}_a(\mathbf{x}, t)$, $\mathbf{u}_U(t)$, and $\mathbf{u}_{\Omega_i}(\mathbf{x}_{r_i}, t)$, respectively. Similarly, $q_{a,s}$ and $q_{\Omega_i,s}$ are the discretized velocity fluxes of $u_a(\mathbf{x}_s, t)$ and $\mathbf{u}_{\Omega_i}(\mathbf{x}_s, t)$, respectively.

The discrete velocity can be recovered by $u^n = q^n/\Delta x$. Sub-matrices G and D correspond to the discrete gradient and divergence operators, respectively. It is interesting to note that $G = -D^T$ for the staggered grid formulation. The *nullspace* or *discrete streamfunction* technique of Chang et al. (2002) is used to satisfy the incompressibility constraint. The discretized streamfunction, s^n, is introduced such that $q^n = Cs^n$, where C is the discrete curl operator. This operator is constructed with column vectors corresponding to the basis of the nullspace of D. Hence, these

operators have the relation, $DC \equiv 0$, which automatically enforces incompressibility at all time, i.e., $Dq^n = DCs^n = 0$. This discrete relation is consistent with the continuous version of the vector identity: $\nabla \cdot \nabla \times \equiv 0$. We note that the operator C^T is another discrete curl operation, and that $\gamma^n = C^T q^n$ is a second-order-accurate approximation to the circulation in each dual cell.

The operators resulting from the implicit velocity term is $A = \frac{1}{\Delta t} I - \frac{1}{2} L$, where L is the discrete (vector) Laplacian. Providing that $Dq^n = 0$, we construct a symmetric Laplacian such that $Lq^n = -\frac{1}{Re \Delta x^2} CC^T q^n = -\frac{1}{Re \Delta x^2} C \gamma^n \equiv -\beta C \gamma^n$, where $\beta = \frac{1}{Re \Delta x^2}$. This identity mimics the continuous identity $\nabla^2 \mathbf{u} = \nabla(\nabla \cdot \mathbf{u}) - \nabla \times \nabla \times \mathbf{u} = -\nabla \times \nabla \times \mathbf{u}$. Therefore, A is symmetric and positive-definite. The right-hand side of equation (2.16) consists of the inhomogeneous terms from the boundary conditions, bc_1 and bc_2, and the explicit terms from the momentum equation, r^n, given by

$$r^n = \left[\frac{1}{\Delta t} I + \frac{1}{2} L \right] q^n + \frac{3}{2\Delta x^2} N(q^n - q_a^n, \gamma^n) - \frac{1}{2\Delta x^2} N(q^{n-1} - q_a^{n-1}, \gamma^n) , \qquad (2.17)$$

where $N(q, \gamma) = q \times \gamma$ is the nonlinear term.

H and E are the regularization and interpolation operator, respectively. These operators are constructed from the regularized discrete delta function. Among the variety of discrete delta functions available, we choose to use the one by Roma et al. (1999) which is specifically designed for use on staggered grids. This function has the form

$$d(z) = \begin{cases} \frac{1}{6\Delta z} \left(5 - 3\frac{|z|}{\Delta z} - \sqrt{-3\left(1 - \frac{|z|}{\Delta z}\right)^2 + 1} \right) & \text{for } 0.5\Delta z \leq |z| \leq 1.5\Delta z , \\ \frac{1}{3\Delta z} \left(1 + \sqrt{-3\left(\frac{|z|}{\Delta z}\right)^2 + 1} \right) & \text{for } |z| \leq 0.5\Delta z , \\ 0 & \text{otherwise} , \end{cases} \qquad (2.18)$$

where Δz is the cell width of the staggered grid in the z-direction. The interpolation operator can

be derived by discretizing equation (2.15), yielding

$$q_{a_j}^n = \Delta x^2 \sum_i q_{n_i}^n d(x_{r_i} - x_{s_j}^n) d(y_{r_i} - y_{s_j}^n) = E_{j,i}^n q_{n_i}^n . \tag{2.19}$$

For the three-dimensional case an extra factor of $\Delta x \, d(z_{r_i} - z_{s_j}^n)$ is needed. Thus, the interpolation operator is given by $E_{j,i}^n = \Delta x^2 d(x_{r_i} - x_{s_j}^n) d(y_{r_i} - y_{s_j}^n)$. Similarly, the regularization operator is given by $H_{i,j}^n = \Delta s \Delta x d(x_{s_j}^n - x_{r_i}) d(y_{s_j}^n - y_{r_i}) = \frac{\Delta s}{\Delta x} E_{j,i}^{n^T}$, where Δs is the Lagrangian grid spacing. If we choose $\Delta s \approx \Delta x$, then $H^n = E^{n^T}$, or $H^n f_{bf} = -E^{n^T} f_{fb}$.

Considering the frame of reference is rotating together with the body, the body is then stationary in the rotating frame, i.e., $\mathbf{x}_s$ is time-independent. Therefore, the interpolation and the regularization matrices are also time-independent, i,e, $E^n = E$ and $H^n = H$. Following the work done by Colonius and Taira (2008), we pre-multiply the momentum equation in equation (2.16) with C^T, and the pressure gradient term is removed from the formulation since $C^T G \pi = -(DC)^T \pi = 0$, which results in the following new algebraic equations:

$$\begin{bmatrix} C^T A C & C^T E^T \\ E C & 0 \end{bmatrix} \begin{pmatrix} s^{n+1} \\ f_{fb} \end{pmatrix} = \begin{pmatrix} C^T r^n \\ q_{a,s}^{n+1} \end{pmatrix} + \begin{pmatrix} bc_1 \\ 0 \end{pmatrix} . \tag{2.20}$$

The form of equation (2.20) is known as the Karush-Kuhn-Tucker (KKT) system that appears in constrained optimization problem (Nocedal and Wright, 2006). The left-hand-side matrix is symmetric but in general indefinite, which makes a direct solution less efficient. However, we can do it in another way. Applying the same spatial discretization but no temporal discretization on equations (2.13) and (2.15) and pre-multiplying the spatial discretized momentum equation with C^T:

$$\frac{d\gamma}{dt}(t) = \frac{1}{\Delta x^2} C^T N \left(q(t) - q_a(t), \gamma(t) \right) - \beta C^T C \gamma(t) - C^T E^T f_{fb} , \tag{2.21}$$

$$E C (C^T C)^{-1} \gamma(t) = q_{a,s}(t) . \tag{2.22}$$

Then the same temporal discretization (the implicit Crank-Nicolson integration for the viscous terms and the explicit second-order Adams-Bashforth scheme for the convective terms) is applied to equations (2.21) and (2.22), which results in a algebraic equations that can be rewritten as

$$
\begin{bmatrix} \frac{1}{\Delta t}I + \frac{\beta}{2}C^T C & C^T E^T \\ EC(C^T C)^{-1} & 0 \end{bmatrix} \begin{pmatrix} \gamma^{n+1} \\ f_{fb} \end{pmatrix} = \begin{pmatrix} C^T r^n \\ q_{a,s}^{n+1} \end{pmatrix} + \begin{pmatrix} bc_\gamma \\ 0 \end{pmatrix} . \tag{2.23}
$$

It can be shown that with the current choice of the discrete Laplacian, equation (2.23) is equivalent to equation (2.20). $C^T C$ can be transformed into a diagonal matrix, Λ, using the discrete sine transform, S, i.e., $C^T C = S\Lambda S$, where $S^{-1} = S$, and the eigenvalues of Λ are known. By performing discrete Fourier sine transform, equation (2.23) can be efficiently solved using the projection (fractional step) approach:

$$
S\left(\frac{1}{\Delta t}I + \frac{\beta}{2}\Lambda\right)S\gamma^* = S\left(\frac{1}{\Delta t}I - \frac{\beta}{2}\Lambda\right)S\gamma^n
$$
$$
+ \frac{3}{2\Delta x^2}C^T N(q^n - q_a^n, \gamma^n) - \frac{1}{2\Delta x^2}C^T N(q^{n-1} - q_a^{n-1}, \gamma^n) + bc_\gamma , \tag{2.24}
$$
$$
EC\left(S\Lambda^{-1}\left(\frac{1}{\Delta t}I + \frac{\beta}{2}\Lambda\right)^{-1}S\right)C^T E^T f_{fb} = ECS\Lambda^{-1}S\gamma^* - q_{a,s}^{n+1} , \tag{2.25}
$$
$$
\gamma^{n+1} = \gamma^* - S\left(\frac{1}{\Delta t}I + \frac{\beta}{2}\Lambda\right)^{-1}SC^T \hat{E}^T f_{fb} . \tag{2.26}
$$

Note that equations (2.24) and (2.25) are Poisson-like equations. We first solve equation (2.24). The solution is called intermediate discrete circulation, γ^*. Equation (2.25) is then solved for the Lagrange multiplier, f_{fb}. Finially, a projection is done by equation (2.26) to obtain the discrete circulation, γ.

A multi-domain approach is developed to solve equation (2.24) with simple far-field boundary conditions, such as equation (2.12), on a progressively coarsifying grids as shown schematically in figure (2.2). First, the discrete circulation and velocity flux from the last time step are interpolated or *coarsified* from the inner mesh onto the outer mesh to obtain corrected right-hand side of equation (2.24) in each grid level. Equation (2.24) is then solved (with zero boundary conditions) on the outer

(larger, coarser) domain for the intermediate discrete circulation, which is then interpolated along the boundary of the inner mesh. Equation (2.24) is solved again, with the "corrected" boundary value specified, on the inner (smaller, finer) mesh. This technique is applied recursively a number of times to obtain the intermediate discrete vorticity in each grid level. Detailed formulation is given by Colonius and Taira (2008):

$$
\begin{aligned}
\gamma^{(k)^*} = \ & S\left(\frac{1}{\Delta t}I + \frac{\beta}{2}\Lambda\right)^{-1}\left\{S\left[\frac{3}{2\Delta x^2}C^T N(q^{(k)^n} - q_a^{(k)^n}, \gamma^{(k)^n})\right.\right. \\
& \qquad - \frac{1}{2\Delta x^2}C^T N(q^{(k)^{n-1}} - q_a^{(k)^{n-1}}, \gamma^{(k)^{n-1}}) \\
& \qquad \left. + \frac{\beta}{2}bc_\gamma\left([P^{(k+1)\to(k)}(\gamma^{(k+1)^*})] + [P^{(k+1)\to(k)}(\gamma^{(k+1)^n})]\right)\right] \\
& \qquad + \left(\frac{1}{\Delta t}I - \frac{\beta}{2}\Lambda\right)S\gamma^{(k)^n}\right\} ,
\end{aligned}
\tag{2.27}
$$

where the superscript (k) denotes variables in the kth-level and $P^{(k+1)\to(k)}$ is the boundary value interpolation operator.
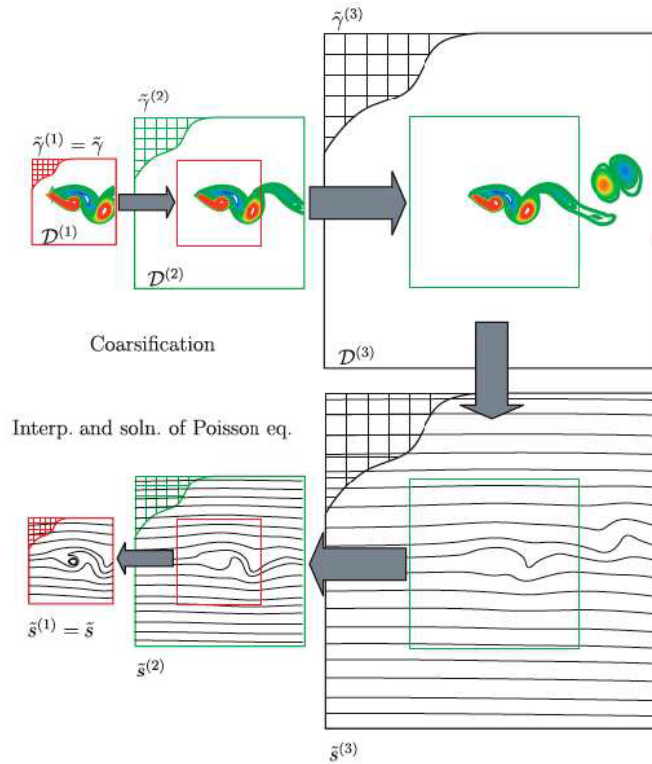
Figure 2.2: Multi-domain method to solve equation (2.24). Figure reproduced with permission from Colonius and Taira (2008).

2.3 The evolution of the flow coupled with the motion of the body

The evolution of the flow can be coupled with the motion of the body by a set of equations of motion:

$$\frac{d\mathbf{X}}{dt}(t) = \dot{\mathbf{X}}(\mathbf{X}, f_{fb}, t) \; , \tag{2.28}$$

where $\mathbf{X}(t)$ is a state vector which elements are (in general) coordinates and velocity of each body point, and $\dot{\mathbf{X}}(\mathbf{X}, f_{fb}, t)$ is the driving term, which is time-dependent and depends on the state vector, $\mathbf{X}(t)$, and the Lagrangian forces, f_{fb}. For example, elements in the state vector can be the rotation angle of the body, $\theta(t)$, or the corresponding angular velocity, $\Omega(t)$. The inertial velocity in the rotating frame then depends on the state vector, i.e., $\mathbf{u}_a = \mathbf{u}_a(\mathbf{X}(t), \mathbf{x}_r)$. When the evolution of the flow is coupled with the motion of the body, equation (2.25) cannot be solved directly because $q_{a,s}^{n+1}$ is unknown. The coupled evolution of the flow field and the motion of the body is solved using the *predictor-corrector* method (PCM). In this method, equations (2.25) and (2.28) are integrated in time using a second order Runge-Kutta scheme.

First, a prediction of the state vector, $\mathbf{X}^*$ is made using the explicit Euler method:

$$\mathbf{X}^* = \mathbf{X}^n + \Delta t \; \dot{\mathbf{X}} \left(\mathbf{X}^n, f_{fb}^n, t^n \right) \; , \tag{2.29}$$

which gives us the prediction of the inertial velocity flux, $q_{a,s}^* = u_a(\mathbf{X}^*, \mathbf{x}_s)\Delta x$. The prediction of Lagrangian forces, f_{fb}^*, is obtained by solving a modified equation of equation (2.25):

$$f_{fb}^* = \left(ECS\Lambda^{-1} \left(\frac{1}{\Delta t}I + \frac{\beta}{2}\Lambda \right)^{-1} SC^T E^T \right)^{-1} \left(ECS\Lambda^{-1} S\gamma^* - q_{a,s}^* \right) \; . \tag{2.30}$$

Note that the operator $ECS\Lambda^{-1} \left(\frac{1}{\Delta t}I + \frac{\beta}{2}\Lambda \right)^{-1} SC^T E^T$ is a symmetric, Poisson-like operator which is independent of time. Therefore, equation 2.30 can be solved efficiently using the Cholesky decomposition.

Corrections in the state vector and Lagrangian forces are made by taking average of the predictions and the values in the nth-step:

$$\mathbf{X}^{n+\frac{1}{2}} = \frac{1}{2}\left(\mathbf{X}^n + \mathbf{X}^*\right) , \tag{2.31}$$

$$f_{fb}^{n+\frac{1}{2}} = \frac{1}{2}\left(f_{fb}^n + f_{fb}^*\right) , \tag{2.32}$$

We then update the state vector using the corrected values:

$$\mathbf{X}^{n+1} = \mathbf{X}^n + \Delta t \, \dot{\mathbf{X}}\left(\mathbf{X}^{n+\frac{1}{2}}, f_{fb}^{n+\frac{1}{2}}, t^{n+\frac{1}{2}}\right) , \tag{2.33}$$

which gives the update of the inertial velocity flux, $q_{a,s}^{n+1} = u_a(\mathbf{X}^{n+1}, \mathbf{x}_s)\Delta x$. Since now $q_{a,s}^{n+1}$ is known, f_{fb}^{n+1} can be solved from equation (2.25) using Cholesky decomposition, i.e.,

$$f_{fb}^{n+1} = \left(ECS\Lambda^{-1}\left(\frac{1}{\Delta t}I + \frac{\beta}{2}\Lambda\right)^{-1}SC^TE^T\right)^{-1}\left(ECS\Lambda^{-1}S\gamma^* - q_{a,s}^{n+1}\right) . \tag{2.34}$$

2.4 Derivation of adjoint equations and control gradients

In this section, supplementing the constraints used in Joe et al. (2010) and Flinois and Colonius (2015) with additional equations of motion to account for coupling the motion of the bodies with the fluid, we rederive the adjoint equations and the corresponding control gradients used by the adjoint-based optimization following the same approach developed in Joe et al. (2010) and Flinois and Colonius (2015). In this study, the following PDE-constrained optimization problem is considered:

$$\text{minimize} \quad \mathcal{J}(\mathbf{X}, f_{fb}, \mathbf{a}) \equiv \int_0^{T_H} \mathcal{F}(\mathbf{X}(t), f_{fb}, \mathbf{a}(t)) \, dt \tag{2.35}$$

$$\text{subject to} \quad \frac{d\gamma}{dt}(t) = \frac{1}{\Delta x^2}C^TN\left(q(t) - q_a(\mathbf{X}(t), \mathbf{a}), \gamma(t)\right) - \beta C^TC\gamma(t) - C^TE^Tf_{fb} , \tag{2.36}$$

$$EC(C^TC)^{-1}\gamma(t) = q_{a,s}(\mathbf{X}(t), \mathbf{a}) , \tag{2.37}$$

$$\text{and} \quad \frac{d\mathbf{X}}{dt}(t) = \dot{\mathbf{X}}(\mathbf{X}(t), f_{fb}, \mathbf{a}, t) , \tag{2.38}$$

where $\mathcal{J}$ is the cost function, $\mathcal{F}$ is the integrand of the cost function, $\mathbf{a}$ is a vector formed by the controlled variables, and T_H is the control horizon.

In order to solve this optimization problem, based on earlier works of Joe et al. (2010) and Flinois and Colonius (2015), an adjoint solvers were developed using the method of Lagrange multiplier. First, we introduce the Lagrangian, $\mathcal{L}$, corresponding to the optimization problem:

$$\mathcal{L} \equiv \int_0^{T_H} \left\{ \mathcal{F}(\mathbf{X}, f_{fb}, \mathbf{a}) - \gamma^{\dagger^T}(C^T C)^{-1} \left[\frac{d\gamma}{dt} - \frac{1}{\Delta x^2} C^T N (q - q_a(\mathbf{X}, \mathbf{a}), \gamma) - \beta C^T C \gamma - C^T E^T f_{fb} \right] \right.$$
$$- f_{fb}^{\dagger^T} \left[EC(C^T C)^{-1} \gamma - q_{a,s}(\mathbf{X}(t), \mathbf{a}) \right]$$
$$\left. - \mathbf{X}^{\dagger^T} \left[\frac{d\mathbf{X}}{dt} - \dot{\mathbf{X}}(\mathbf{X}, f_{fb}, \mathbf{a}, t) \right] \right\} dt , \tag{2.39}$$

where the superscript $\dagger$ denotes the adjoint variables of the corresponding state variables. Note that Lagrangian uses the inner product of velocity fluxes instead of that of circulations so that $(C^T C)^{-1}$ is added since $\gamma^{\dagger^T}(C^T C)^{-1}\gamma = q^{\dagger^T} q$. By collecting terms not involving time-derivative into a Hamiltonian, $\mathcal{H}$, we obtain

$$\mathcal{L}(\mathbf{X}, \gamma, f_{fb}, \mathbf{a}) = \int_0^{T_H} \left\{ \mathcal{H}(\mathbf{X}, \gamma, f_{fb}, \mathbf{a}) - \gamma^{\dagger^T}(C^T C)^{-1} \frac{d\gamma}{dt} - \mathbf{X}^{\dagger^T} \frac{d\mathbf{X}}{dt} \right\} dt , \tag{2.40}$$

where

$$\mathcal{H}(\mathbf{X}, \gamma, f_{fb}, \mathbf{a}) = \mathcal{F}(\mathbf{X}, f_{fb}, \mathbf{a}) + \gamma^{\dagger^T}(C^T C)^{-1} \left[\frac{1}{\Delta x^2} C^T N (q - q_a(\mathbf{X}, \mathbf{a}), \gamma) - \beta C^T C \gamma - C^T E^T f_{fb} \right]$$
$$- f_{fb}^{\dagger^T} \left[EC(C^T C)^{-1} \gamma - q_{a,s}(\mathbf{X}(t), \mathbf{a}) \right] + \mathbf{X}^{\dagger^T} \dot{\mathbf{X}}(\mathbf{X}, f_{fb}, \mathbf{a}, t) . \tag{2.41}$$

Integrating equation (2.40) by parts, we obtain

$$\mathcal{L} = \int_0^{T_H} \left\{ \mathcal{H} + \frac{d\gamma^\dagger}{dt}^T (C^T C)^{-1} \gamma + \frac{d\mathbf{X}^\dagger}{dt}^T \mathbf{X} \right\} dt$$
$$+ \gamma^\dagger(0)^T (C^T C)^{-1} \gamma(0) - \gamma^\dagger(T_H)^T (C^T C)^{-1} \gamma(T_H) + \mathbf{X}^\dagger(0)^T \mathbf{X}(0) - \mathbf{X}^\dagger(T_H)^T \mathbf{X}(T_H) . \tag{2.42}$$

Therefore, the total derivative of the Lagrangian is

$$\frac{d\mathcal{L}}{d\mathbf{a}} = \int_0^{T_H} \left\{ \left[\left(\frac{\partial \mathcal{H}}{\partial \gamma} \right)^T + (C^T C)^{-1} \frac{d\gamma^\dagger}{dt} \right]^T \frac{\partial \gamma}{\partial \mathbf{a}} + \left(\frac{\partial \mathcal{H}}{\partial f_{fb}} \right) \frac{\partial f_{fb}}{\partial \mathbf{a}} + \left[\left(\frac{\partial \mathcal{H}}{\partial \mathbf{X}} \right)^T + \frac{d\mathbf{X}^\dagger}{dt} \right]^T \frac{\partial \mathbf{X}}{\partial \mathbf{a}} + \frac{\partial \mathcal{H}}{\partial \mathbf{a}} \right\} dt$$

$$+ \gamma^\dagger(0)^T (C^T C)^{-1} \frac{\partial \gamma(0)}{\partial \mathbf{a}} - \gamma^\dagger(T_H)^T (C^T C)^{-1} \frac{\partial \gamma(T_H)}{\partial \mathbf{a}}$$

$$+ \mathbf{X}^\dagger(0)^T \frac{\partial \mathbf{X}(0)}{\partial \mathbf{a}} - \mathbf{X}^\dagger(T_H)^T \frac{\partial \mathbf{X}(T_H)}{\partial \mathbf{a}} . \tag{2.43}$$

Since the initial conditions do not change with controlled variables, i.e. $\frac{\partial \gamma(0)}{\partial \mathbf{a}} = 0$, and $\frac{\partial \mathbf{X}(0)}{\partial \mathbf{a}} = 0$, and $\frac{\partial \gamma}{\partial \mathbf{a}}(t)$, $\frac{\partial f_{fb}}{\partial \mathbf{a}}$, $\frac{\partial \mathbf{X}}{\partial \mathbf{a}}(t)$, $\frac{\partial \gamma(T_H)}{\partial \mathbf{a}}$, and $\frac{\partial \mathbf{X}(T_H)}{\partial \mathbf{a}}$ are difficult to calculate, if we set

$$\left(\frac{\partial \mathcal{H}}{\partial \gamma} \right)^T + (C^T C)^{-1} \frac{d\gamma^\dagger}{dt} = 0 \implies -\frac{d\gamma^\dagger}{dt} = (C^T C) \left(\frac{\partial \mathcal{H}}{\partial \gamma} \right)^T , \tag{2.44}$$

$$\left(\frac{\partial \mathcal{H}}{\partial f_{fb}} \right)^T = 0 , \tag{2.45}$$

$$\left(\frac{\partial \mathcal{H}}{\partial \mathbf{X}} \right)^T + \frac{d\mathbf{X}^\dagger}{dt} = 0 \implies -\frac{d\mathbf{X}^\dagger}{dt} = \left(\frac{\partial \mathcal{H}}{\partial \mathbf{X}} \right)^T , \tag{2.46}$$

$$\gamma^\dagger(T_H) = 0 , \tag{2.47}$$

$$\mathbf{X}^\dagger(T_H) = 0 , \tag{2.48}$$

then the Lagrangian becomes

$$\frac{d\mathcal{L}}{d\mathbf{a}} = \int_0^{T_H} \left(\frac{\partial \mathcal{H}}{\partial \mathbf{a}} \right) dt . \tag{2.49}$$

Note that equation (2.44) is the adjoint of the Navier-Stokes equations and equation (2.47) is the corresponding initial condition. Equation (2.45) is the adjoint of no-slip boundary condition. Equation (2.46) is the adjoint of the equation of motion and equation (2.48) is the corresponding initial condition. Therefore, we need to find an optimal control $\mathbf{a}_{\text{opt}}$ such that $\frac{d\mathcal{L}}{d\mathbf{a}}(\mathbf{a}_{\text{opt}}) = 0$ with the constraints of equations (2.44) to (2.48) .

By substituting the Hamiltonian in equation (2.41) into equations (2.44), (2.45), (2.46), and

(2.49), they yield

$$\frac{d\gamma^\dagger}{d\tau}(\tau) = \frac{1}{\Delta x^2} C^T N^\dagger \left(q^\dagger(\tau), q(\tau) - q_a(\mathbf{X}(\tau), \mathbf{a}), \gamma(\tau) \right) - C^T E^T f_{fb}^\dagger , \tag{2.50}$$

$$EC(C^T C)^{-1} \gamma^\dagger(\tau) = q_{a,s}^\dagger(\mathbf{X}^\dagger(\tau), \mathbf{X}(\tau), f_{fb}, \mathbf{a}) , \tag{2.51}$$

$$\frac{d\mathbf{X}^\dagger}{d\tau}(\tau) = \dot{\mathbf{X}}^\dagger(\mathbf{X}^\dagger(\tau), \mathbf{X}(\tau), f_{fb}, \mathbf{a}, \tau) , \tag{2.52}$$

where

$$\tau \equiv T_H - t , \tag{2.53}$$

$$N^\dagger \left(q^\dagger, q - q_a(\mathbf{X}, \mathbf{a}), \gamma \right) \equiv CN \left(q^\dagger, q - q_a(\mathbf{X}, \mathbf{a}) \right) - N \left(q^\dagger, \gamma \right) , \tag{2.54}$$

is the adjoint of nonlinear term (detailed derivation in appendix B),

$$q_{a,s}^\dagger(\mathbf{X}^\dagger, \mathbf{X}, f_{fb}, \mathbf{a}) \equiv \left(\frac{\partial \mathcal{F}}{\partial f_{fb}}(\mathbf{X}, f_{fb}, \mathbf{a}) \right)^T + \left(\frac{\partial \dot{\mathbf{X}}}{\partial f_{fb}}(\mathbf{X}, f_{fb}, \mathbf{a}, t) \right)^T \mathbf{X}^\dagger , \tag{2.55}$$

is the adjoint velocity flux,

$$\dot{\mathbf{X}}^\dagger(\mathbf{X}^\dagger, \mathbf{X}, f_{fb}, \mathbf{a}, t) \equiv \left(\frac{\partial \mathcal{F}}{\partial \mathbf{X}}(\mathbf{X}, f_{fb}, \mathbf{a}) \right)^T - \frac{1}{\Delta x^2} q^{\dagger^T} N \left(\frac{\partial q_a}{\partial \mathbf{X}}(\mathbf{X}, \mathbf{a}), \gamma \right)$$
$$+ \left(\frac{\partial q_{a,s}}{\partial \mathbf{X}}(\mathbf{X}, \mathbf{a}) \right)^T f_{fb}^\dagger + \left(\frac{\partial \dot{\mathbf{X}}}{\partial \mathbf{X}}(\mathbf{X}, f_{fb}, \mathbf{a}, t) \right)^T \mathbf{X}^\dagger , \tag{2.56}$$

is the right-hand side of the adjoint equation of motion, and

$$\frac{\partial \mathcal{H}}{\partial \mathbf{a}} = \left(\frac{\partial \mathcal{F}}{\partial \mathbf{a}}(\mathbf{X}, f_{fb}, \mathbf{a}) \right) - \frac{1}{\Delta x^2} N \left(\frac{\partial q_a}{\partial \mathbf{a}}(\mathbf{X}, \mathbf{a}), \gamma \right)^T q^\dagger$$
$$+ f_{fb}^{\dagger^T} \left(\frac{\partial q_{a,s}}{\partial \mathbf{a}}(\mathbf{X}, \mathbf{a}) \right) + \mathbf{X}^{\dagger^T} \left(\frac{\partial \dot{\mathbf{X}}}{\partial \mathbf{a}}(\mathbf{X}, f_{fb}, \mathbf{a}, t) \right) . \tag{2.57}$$

We can see that adjoint equations (2.50), (2.51), and (2.52) have the same form as equations (2.36), (2.37), and (2.38). Therefore, they can be solved backward in time (since $\tau = T_H - t$) with zero initial conditions (equations (2.47) and (2.48)) using the fast immersed boundary method and predictor-

corrector method introduced in sections 2.2 and 2.3.

The forms of $q_{a,s}^{\dagger}(\mathbf{X}^{\dagger}, \mathbf{X}, f_{fb}, \mathbf{a})$, $\dot{\mathbf{X}}^{\dagger}(\mathbf{X}^{\dagger}, \mathbf{X}, f_{fb}, \mathbf{a}, t)$, and $\frac{d\mathcal{L}}{d\mathbf{a}}(\mathbf{a})$ depends on the choices of $\mathcal{F}(\mathbf{X}, f_{fb}, \mathbf{a})$, $\mathbf{X}(t)$, $\dot{\mathbf{X}}(\mathbf{X}, f_{fb}, \mathbf{a}, t)$, and $\mathbf{a}(t)$. In this study, the following sets of $\dot{\mathbf{X}}(\mathbf{X}, f_{fb}, \mathbf{a}, t)$, $\mathbf{X}(t)$, and $\mathbf{a}$ are considered in this study:

$$1. : \quad \dot{\mathbf{X}} = \Omega_j , \quad \mathbf{X} = \theta_j , \quad \mathbf{a} = \Omega_j , \tag{2.58}$$

$$2. : \quad \dot{\mathbf{X}} = \frac{1}{I_j}(\tau_{fb_j} + \tau_{m_j}) , \quad \mathbf{X} = \Omega_j , \quad \mathbf{a} = \tau_{m_j} , \tag{2.59}$$

where I_j is the moment of inertia of the body about the $j-$th rotation center. θ_j and Ω_j are the rotation angle and angular velocity of the $j-$th rotating frame relative to the $(j-1)-$th rotating frame, respectively. $\tau_{fb_j} = \hat{S}(\mathbf{x}_s \times f_{fb})$ and τ_{m_j} are the torque exerted by the fluid on the body and by the motor about the $j-$th rotation center, respectively. $\tilde{S}$ is a first-order integration matrix,

$$\tilde{S} = \begin{pmatrix} 1, 1, \cdots, 1, 0, 0, \cdots, 0 \\ 0, 0, \cdots, 0, 1, 1, \cdots, 1 \end{pmatrix}_{2 \times (2n_b)} \Delta x , \tag{2.60}$$

where n_b is the number of points of a body.

We considered three kinds of $\mathcal{F}(\mathbf{X}, f_{fb}, \mathbf{a})$:

1. squared force difference: $\quad \frac{1}{2}\Delta F^T Q_i \Delta F$, where $\quad \Delta F = B(\phi)\tilde{S}f_{fb} - F_{\text{ref}}$, $\qquad$ (2.61)

2. power generated by the fluid: $\quad Q_i \tau_{fb_j} \Omega_j$, $\qquad$ (2.62)

3. power input from the motor: $\quad Q_i(-\tau_{m_j}\Omega_j)$, $\qquad$ (2.63)

where Q_i is the coefficient (matrix). In equation (2.61), ΔF is the difference of the desired forces to its targeted values, F_{ref}, and $B(\phi)$ is the rotation matrix, which for 2D is given by

$$B(\phi) = \begin{pmatrix} \cos\phi & -\sin\phi \\ \sin\phi & \cos\phi \end{pmatrix} , \tag{2.64}$$

where ϕ is the rotation angle from the rotating frame to the desired orientation of the integrated forces, which is a function of θ_j. For examples, if the freestream is in $(+x)-$direction in the inertial (laboratory) frame and $x-$direction of the grid is aligned with the chord of the body, then $B(\phi = \alpha)\hat{S}f_{fb} = (F_D, -F_L)^T$, i.e., $(\hat{S}f_{fb})_n = B(\phi = \alpha)(\hat{S}f_{fb})_r$, and $B(\phi = 0)\hat{S}f_{fb} = (-F_T, F_N)^T$, where F_D is the drag, F_L is the lift, F_T is the force tangent to the chord of the body, and F_N is the force normal to the chord of the body. Moreover, the derivative of the rotation matrix $B(\phi)$ has the properties

$$\frac{dB(\phi)}{d\phi} = B\left(\phi + \frac{\pi}{2}\right) = B(\phi)B\left(\frac{\pi}{2}\right) = B\left(\frac{\pi}{2}\right)B(\phi) \ . \tag{2.65}$$

The derivatives of $\mathcal{F}(\mathbf{X}, f_{fb}, \mathbf{a})$ and $\dot{\mathbf{X}}(\mathbf{X}, f_{fb}, \mathbf{a}, t)$ with respect to f_{fb}, $\mathbf{X}$, and $\mathbf{a}$ are listed in table 2.1 and 2.2, respectively. Note that in table 2.2, $q_{\Omega_j^\dagger, s} = (\Omega_j^\dagger \times \mathbf{x}_s)\Delta x$ is the velocity flux on the body induced by the adjoint angular velocity $\Omega_j^\dagger$.

Table 2.1: Derivatives of $\mathcal{F}(\mathbf{X}, f_{fb}, \mathbf{a})$ with respect to f_{fb}, $\mathbf{X}$, and $\mathbf{a}$.

$\mathcal{F}$	$\frac{\partial \mathcal{F}}{\partial f_{fb}}$	$\frac{\partial \mathcal{F}}{\partial \theta_j}$	$\frac{\partial \mathcal{F}}{\partial \Omega_j}$	$\frac{\partial \mathcal{F}}{\partial \tau_{m_j}}$
$Q_i \tau_{fb_j} \Omega_j$	$Q_i q_{\Omega_j}$	0	$Q_i \tau_{fb_j}$	0
$Q_i \tau_{m_j} \Omega_j$	0	0	$Q_i \tau_{m_j}$	$Q_i \Omega_j$
$\frac{1}{2}\Delta F^T Q_i \Delta F$	$\hat{S}^T B^T Q_i \Delta F$	$\frac{d\phi}{d\theta_j}\left(B\left(\frac{\pi}{2}\right)\Delta F\right)^T Q_i \Delta F$	0	0

Table 2.2: Derivatives of $\dot{\mathbf{X}}(\mathbf{X}, f_{fb}, \mathbf{a}, t)$ with respect to f_{fb}, $\mathbf{X}$, and $\mathbf{a}$.

$\dot{\mathbf{X}}$	$\left(\frac{\partial \dot{\mathbf{X}}}{\partial f_{fb}}\right)^T f_{fb}^\dagger$	$\left(\frac{\partial \dot{\mathbf{X}}}{\partial \theta_j}\right)^T \mathbf{X}^\dagger$	$\left(\frac{\partial \dot{\mathbf{X}}}{\partial \Omega_j}\right)^T \mathbf{X}^\dagger$	$\left(\frac{\partial \dot{\mathbf{X}}}{\partial \tau_{m_j}}\right)^T \mathbf{X}^\dagger$
Ω_j	0	0	$\theta_j^\dagger$	0
$\frac{1}{I_j}(\tau_{fb_j} + \tau_{m_j})$	$\frac{1}{I_j} q_{\Omega_j^\dagger, s}$	0	0	$\frac{1}{I_j}\Omega_j^\dagger$

For the derivatives of $q_a(\mathbf{X}, \mathbf{a}) = q_U + q_{\Omega_1} + q_{\Omega_2}$, since q_U is usually independent of θ_j in the inertial frame, i.e., $\frac{d(q_U)_n}{d\theta_j} = 0$,

$$\frac{d(q_U)_{r_2}}{d\theta_j} = \frac{d(B(\theta_1 + \theta_2)^T (q_U)_n)}{d\theta_j} = B\left(\frac{\pi}{2}\right)^T B(\theta_1 + \theta_2)^T (q_U)_n = B\left(\frac{\pi}{2}\right)^T (q_U)_{r_2} \ . \tag{2.66}$$

Moreover, q_{Ω_1} is independent of θ_1 but not θ_2 and q_{Ω_2} is independent of both θ_1 and θ_2 because

the rotations are successive. Therefore, $\frac{\partial (q_{\Omega_2})_{r_2}}{\partial \theta_1} = 0$, $\frac{\partial (q_{\Omega_2})_{r_2}}{\partial \theta_2} = 0$, $\frac{\partial (q_{\Omega_1})_{r_2}}{\partial \theta_1} = 0$, and $\frac{\partial (q_{\Omega_1})_{r_2}}{\partial \theta_2} = B\left(\frac{\pi}{2}\right)^T q_{U_{\mathrm{rel}}}$, where $U_{\mathrm{rel}} = \mathbf{\Omega_2} \times \mathbf{R}_2$ is the relative velocity of O_2 to O_1. Therefore,

$$\frac{\partial q_a}{\partial \theta_j} = B\left(\frac{\pi}{2}\right)^T \left(q_U + q_{U_{\mathrm{rel}}}\delta_{2j}\right) \ , \tag{2.67}$$

$$\frac{\partial q_a}{\partial \Omega_j} = q_{\hat{\Omega}_j} \ , \tag{2.68}$$

$$\frac{\partial q_a}{\partial \tau_{m_j}} = 0 \ , \tag{2.69}$$

where $q_{\hat{\Omega}_j}$ is the velocity flux of $\hat{\mathbf{\Omega}}_j \times \mathbf{x}_{r_j}$ and δ_{ij} is the Kronecker delta.

2.5   Procedures of optimal control

Even with the adjoint equations and boundary conditions derived in section 2.4, finding an control $\mathbf{a}_{\mathrm{opt}}$ such that $\frac{d\mathcal{L}}{d\mathbf{a}}(\mathbf{a}_{\mathrm{opt}}) = 0$ is difficult. Instead, we find an optimal control iteratively. In each iteration, the procedure contains three steps, which are illustrated as follows:

Step 1: Generally in the p-th step, a control, $\mathbf{a}^{[p]}$, is given (the iteration usually starts from the baseline case, i.e., $\mathbf{a}^{[0]} = 0$). Equations (2.36) to (2.38) are solved forward in time (from 0 to T_H) using the fast immersed boundary projection method (IBPM) and predictor-corrector method (PCM) introduced in sections 2.2 and 2.3. The solutions, $\gamma^{[p]}$, $q^{[p]}$, $f_{fb}^{[p]}$, and $\mathbf{X}^{[p]}$, are called forward variables. The total cost function with this control, $\mathcal{J}(\mathbf{a}^{[p]})$, is then evaluated by equation (2.35).

Step 2: With forward variables, equations (2.50) to (2.52) are solved backward in time (from T_H to 0) using IBPM and PCM again. The solutions, $\gamma^{\dagger[p]}$, $q^{\dagger[p]}$, $f_{fb}^{\dagger[p]}$, and $\mathbf{X}^{\dagger[p]}$ are called adjoint (backward) variables. The control gradient, $\left(\frac{\partial \mathcal{H}}{\partial \mathbf{a}}\right)^{[p]}$, is computed by equation (2.57).

Step 3: Update the control with the negative of the control gradient multiplied by a distance, d_{ctrl},

$$\mathbf{a}^{[p+1]} = \mathbf{a}^{[p]} - \left(\frac{\partial \mathcal{H}}{\partial \mathbf{a}}\right)^{[p]} d_{\mathrm{ctrl}} \tag{2.70}$$

Proceed a *line search* in d_{ctrl} such that the total cost function given by equation (2.35) is minimized.

A flow chart of the procedure is shown in figure 2.3. The procedure described in step 3 is more like the steepest decent (SD) method. However, the conjugate gradient (CG) method is instead used for the optimization in our computations because it is proven to converge much faster than the SD method. Moreover, for our non-convex and nonlinear optimization problem, we choose to use the CG method called the Polak-Ribiere formula (Polak, 1970), which is known to converge faster than other conjugate algorithms (Shewchuk, 1994) in this kind of optimization problem.

Start with $p = 0$
and choose a $\mathbf{a}^{[0]}$.

Given $\mathbf{a}^{[p]}$, run forward simulation (eqs. (2.36) to (2.38)) to obtain forward variables, $\gamma^{[p]}$, $q^{[p]}$, $f_{fb}^{[p]}$, and $\mathbf{X}^{[p]}$ and evaluate $\mathcal{J}(\mathbf{a}^{[p]})$.

Run backward simulation (eqs. (2.50) to (2.52)) to obtain forward variables, $\gamma^{\dagger[p]}$, $q^{\dagger[p]}$, $f_{fb}^{\dagger[p]}$, and $\mathbf{X}^{\dagger[p]}$ and compute the control gradient, $\left(\frac{\partial \mathcal{H}}{\partial \mathbf{a}}\right)^{[p]}$.

Update the control with $\left(\frac{\partial \mathcal{H}}{\partial \mathbf{a}}\right)^{[p]}$ using either SD or CG method and proceed line search in the distance, d_{ctrl}, such that $\mathcal{J}(\mathbf{a}^{[p+1]})$ is minimized.

Is $\mathcal{J}(\mathbf{a}^{[p+1]})$ converged?

no

yes

Stop

Figure 2.3: Flow chart of the iterative procedures.

Chapter 3

Coriolis effect on the dynamic stall in a VAWT

As discussed in section 1.2, Wang et al. (2010) introduced a simplified model of an airfoil undergoing an equivalent planar motion. However, this model does not account for the forces associated with the non-inertial reference frame. The Coriolis force, in particular, depends on the fluid velocity and is known to locally affect the dynamic stall. In this chapter, we focus on investigating the effect of the Coriolis force on dynamic stall by comparing the rotating airfoil to one undergoing an equivalent planar motion. Simulation results are then compared with PIV data in Ferreira et al. (2007) and water-tunnel experiments performed by collaborators Dunne and McKeon (2014, 2015a,b) in Dunne et al. (2015). Moreover, airfoils undergoing a sinusoidal pitching motion and a sinusoidal surging-pitching motion are also computed and compared to the full VAWT and equivalent planar motions. The coupling of the Coriolis force with the incoming velocity and angle-of-attack variations in VAWT and equivalent planar motions is also studied. Finally, open-loop control is applied to control dynamic stall vortices.

3.1   Simulation setup

Figure 3.1 shows a schematic of a single-bladed VAWT with radius R rotating at an angular velocity Ω with a freestream velocity, U_∞, coming from the left. The chord length of the turbine blade is c. In order to systematically investigate the aerodynamics of a VAWT, five dimensionless parameters

are introduced:

$$\text{tip-speed ratio:} \quad \lambda = \frac{\Omega R}{U_\infty} \ , \tag{3.1}$$

$$\text{radius-to-chord-length ratio:} \quad \ell = \frac{R}{c} \ , \tag{3.2}$$

$$\text{solidity:} \quad \sigma = \frac{N_b c}{2\pi R} = \frac{N_b}{2\pi \ell} \ , \tag{3.3}$$

$$\text{Reynolds number:} \quad Re = \frac{U_\infty c}{\nu} \ , \tag{3.4}$$

$$\text{Rossby number:} \quad Ro = \frac{U_\infty}{2\Omega c} = \frac{\ell}{2\lambda} = \frac{1}{4k} \ , \tag{3.5}$$

where N_b is the number of blades ($N_b = 1$ in this case), ν is the kinematic viscosity of the fluid, and k is the reduce frequency, $k = \frac{\Omega c}{2U_\infty} = \frac{\lambda}{2\ell}$. Rossby number is the ratio of the inertial force to the Coriolis force, which is used to scale the Coriolis force. In this thesis, we focus on the effect of tip-speed ratio, Reynolds number, and Rossby number on the dynamic stall in a single-bladed VAWT. The effect of solidity is discussed in more detail by Araya and Dabiri in Araya (2016), where a new parameter called the dynamic solidity, which is associated with the tip-speed ratio and the turbine solidity, is defined to quantitatively relate the dynamics of the VAWT to that of a solid cylinder.
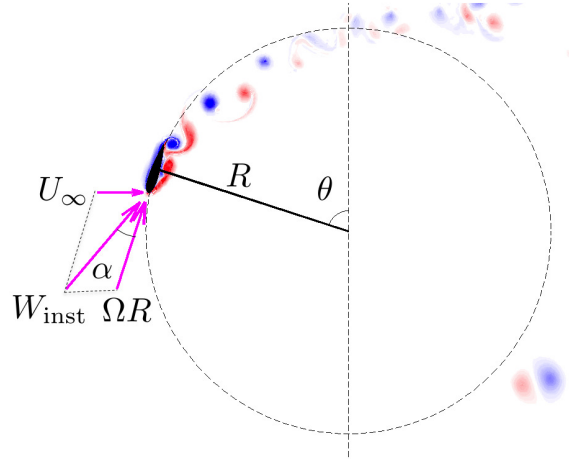
Figure 3.1: Schematic of a single-bladed VAWT and the computational domain.

The instantaneous incoming velocity W_{inst} and the angle of attack α can then be characterized as a function of the tip speed ratio λ and the azimuthal angle θ:

$$\alpha(\lambda, \theta) = \tan^{-1}\left(\frac{\sin\theta}{\lambda + \cos\theta}\right) , \tag{3.6}$$

$$\frac{W_{\text{inst}}(\lambda, \theta)}{U_\infty} = \sqrt{1 + 2\lambda\cos\theta + \lambda^2} . \tag{3.7}$$

Figure 3.2 shows the angle of attack variation and incoming velocity variation of the VAWT at $\lambda = 2$. From equation (3.6), the maximum angle of attack,

$$\alpha_{\text{max}}(\lambda) = \tan^{-1}\left(\frac{1}{\sqrt{\lambda^2 - 1}}\right) , \tag{3.8}$$

occurs at $\theta = \cos^{-1}\left(-\frac{1}{\lambda}\right)$.

In order to isolate the Coriolis effect on dynamic stall, a moving airfoil experiencing an equivalent incoming velocity and angle-of-attack variation over a cycle is proposed. This equivalent planar motion (EPM) is composed of a surging motion with a velocity W_{surge} and a pitching motion around the leading edge with a pitch rate $\dot{\alpha}$. The airfoil is undergoing the EPM in a freestream velocity W_{avg}. W_{avg}, W_{surge}, and $\dot{\alpha}$ are shown to be

$$\frac{W_{\text{avg}}(\lambda)}{U_\infty} = \frac{1}{2\pi}\int_0^{2\pi} \frac{W_{\text{inst}}(\lambda, \theta)}{U_\infty}\, d\theta = \frac{2(1 + \lambda)}{\pi} E\left(\sqrt{\frac{4\lambda}{(1 + \lambda)^2}}\right) , \tag{3.9}$$

where the function, $E(m) = \int_0^{\pi/2} \sqrt{1 - m^2\sin^2\theta}\, d\theta$, is the complete elliptic integral of the second kind,

$$W_{\text{surge}}(\lambda, \theta) = W_{\text{inst}}(\lambda, \theta) - W_{\text{avg}}(\lambda) , \tag{3.10}$$

$$\dot{\alpha}(\lambda, \theta) = \frac{1}{2Ro}\left(\frac{1 + \lambda\cos\theta}{1 + 2\lambda\cos\theta + \lambda^2}\right) . \tag{3.11}$$

The flow around a rotating airfoil in a VAWT is complicated not only by the Coriolis effect but also because the angle of attack and incoming velocity vary simultaneously. It is interesting to

understand whether the Coriolis effect has strong coupling with the angle of attack or incoming velocity variations. Therefore, we independently examine airfoils undergoing only pitching motion and only surging motion associated with VAWT and EPM. Moreover, inspired by Wang et al. (2010), who studied dynamic stall in a VAWT by investigating an airfoil undergoing a simplified sinusoidal pitching motion, we introduce sinusoidal approximations of the angle of attack and incoming velocity of VAWT,

$$\alpha_{\sin}(\lambda, \theta) = \alpha_{\max}(\lambda) \sin \theta \ , \tag{3.12}$$

$$\frac{W_{\text{inst,sin}}(\lambda, \theta)}{U_\infty} = \lambda + \cos \theta \ , \tag{3.13}$$

which are shown in figure 3.2.

(a) Angle of attack variation

(b) Incoming velocity variation
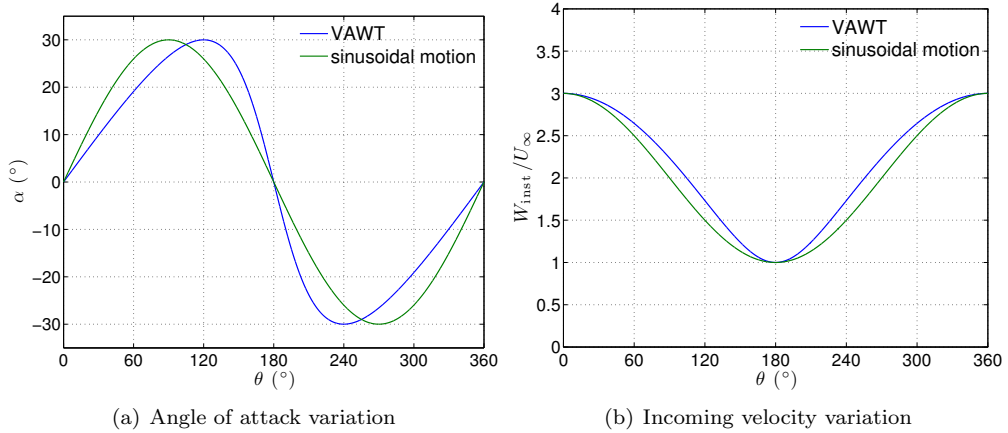
Figure 3.2: Comparison of angle of attack variation and incoming velocity variation between the VAWT and the sinusoidal motion at $\lambda = 2$.

Although the sinusoidal motion shares the same amplitude, it overestimates the angle of attack in the upstroke phase, underestimates the incoming velocity in the downstroke phase, and slightly underestimates the instantaneous velocity over the entire half-cycle. In order to search for the most appropriate model for a VAWT, we introduce two additional motions: a sinusoidal pitching motion (SPM) and a sinusoidal surging-pitching motion (SSPM). Airfoils undergoing both the SPM and SSPM pitch with the sinusoidal angle-of-attack variation described in equation (3.12) in a freestream velocity $W_{\text{avg,sin}} = \lambda U_\infty$. Airfoils undergoing the SSPM also surge with a velocity

$W_{\text{surge,sin}} = U_\infty \cos\theta$. All motions investigated in this chapter are summarized in table 3.1.

Table 3.1: Summary of the VAWT motion and all simplified motions. Symbol $\times$ denotes that the motion is exactly the same as the VAWT motion described in equations (3.6) and (3.7). Symbol $\circ$ denotes that the motion is the sinusoidal approximation of the VAWT motion described in equations (3.12) and (3.13).

Motion	incoming velocity	angle of attack	rotation
VAWT	$\times$	$\times$	$\times$
only surging motion of VAWT	$\times$		$\times$
only pitching motion of VAWT		$\times$	$\times$
EPM	$\times$	$\times$	
only surging motion of EPM	$\times$		
only pitching motion of EPM		$\times$	
SPM		$\circ$	
SSPM	$\circ$	$\circ$	

NACA 0018 airfoils are used as blades in the present study in order to compare with experiments performed by Dunne and McKeon (2014, 2015a). The ratio of the radius of the turbine to the chord length, ℓ, depends on the choice of the tip-speed ratio, λ, and the Rossby number, Ro. In preliminary simulations of a three-bladed VAWT, as well as in previous studies (Ferreira et al., 2007), vorticity-blade interaction is only observed in the downwind-half of a cycle. Since only the flow in the upwind-half cycle is important to torque generation, we save computational time by modeling a single-bladed turbine. We compute about five periods of motion, which is equal to $5\pi/Ro$ convective time units, to remove transients associated with the startup of periodic motion. For the largest Rossby number we examined, the starting vortex propagates far enough into the wake to have an insignificant effect on the forces on the blades after five periods. An additional five periods of nearly periodic stationary-state motion were then computed and analyzed below.

IBPM introduced in section 2.2 is used to compute two-dimensional incompressible flows in an airfoil-fixed reference frame with appropriate forces added to the momentum equation to account for the non-inertial reference frame as described in section 2.1. Based on the analysis by Colonius and Taira (2008), IBPM is estimated to have an $O(4^{-N_g})$ convergence rate, where N_g is the number of the grid levels. Six grid levels are used for the present computations in order to have the leading-order

error dominated by the truncation error arising from the discrete delta functions at the immersed boundary and the discretization of the Poisson equation. The coarsest grid extends to 96 chord lengths in both the transverse and streamwise directions of the blade.

In order to show grid convergence, we examine a single-bladed VAWT with $\ell = 1.5$ rotating at $\lambda = 2$. The velocity field in the streamwise direction is compared to one on the finest grid with $\Delta x = 0.00125$ at $t = 1$. Figure 3.3 shows the spatial convergence in the L_2 norm. The rate of decay for the spatial error is about 1.5, which agrees with Taira and Colonius (2007). All ensuing computations use a 600×600 grid, which corresponds to $\Delta x = 0.005$. The time step, Δt, is chosen to make Courant-Friedrichs-Lewy (CFL) number less than 0.4.
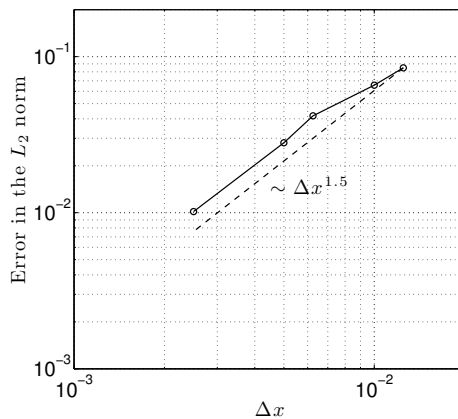
Figure 3.3: The L_2 norm of the error of the velocity field in the streamwise direction in a single-bladed VAWT with $\ell = 1.5$ rotating at $\lambda = 2$ at $t = 1$.

3.2 Qualitative flow features in a VAWT

We begin by examining the flow at low tip-speed ratio, $\lambda = 2$, $Ro = 1.5$, and $Re = 1500$, which gives a maximum amplitude of 30 degrees in angle of attack variation and a reduced frequency $k = 1/6$. Figure 3.4 shows the vorticity field generated by the blade at different azimuthal angles over a cycle. Negative and positive vorticity are plotted in blue and red contour levels, respectively, and all vorticity contour plots use the same contour levels.

At the beginning of a cycle (figure 3.4(a)), the airfoils are just returning to zero angle of attack, and there are still the remnants of earlier vortex shedding in the wake. The flow reattaches by the

(a) $\theta = 0°/360°$, $\alpha = 0°$ (b) $\theta = 15°$, $\alpha = 5.0°$ (c) $\theta = 60°$, $\alpha = 19.1°$ (d) $\theta = 90°$, $\alpha = 26.6°$

(e) $\theta = 120°$, $\alpha = 30°$ (f) $\theta = 135°$, $\alpha = 28.7°$ (g) $\theta = 150°$, $\alpha = 23.8°$ (h) $\theta = 165°$, $\alpha = 14.1°$

(i) $\theta = 180°$, $\alpha = 0°$ (j) $\theta = 195°$, $\alpha = -14.1°$ (k) $\theta = 210°$, $\alpha = -23.8°$ (l) $\theta = 225°$, $\alpha = -28.7°$

(m) $\theta = 240°$, $\alpha = -30°$ (n) $\theta = 270°$, $\alpha = -26.6°$ (o) $\theta = 300°$, $\alpha = -19.1°$ (p) $\theta = 330°$, $\alpha = -9.9°$
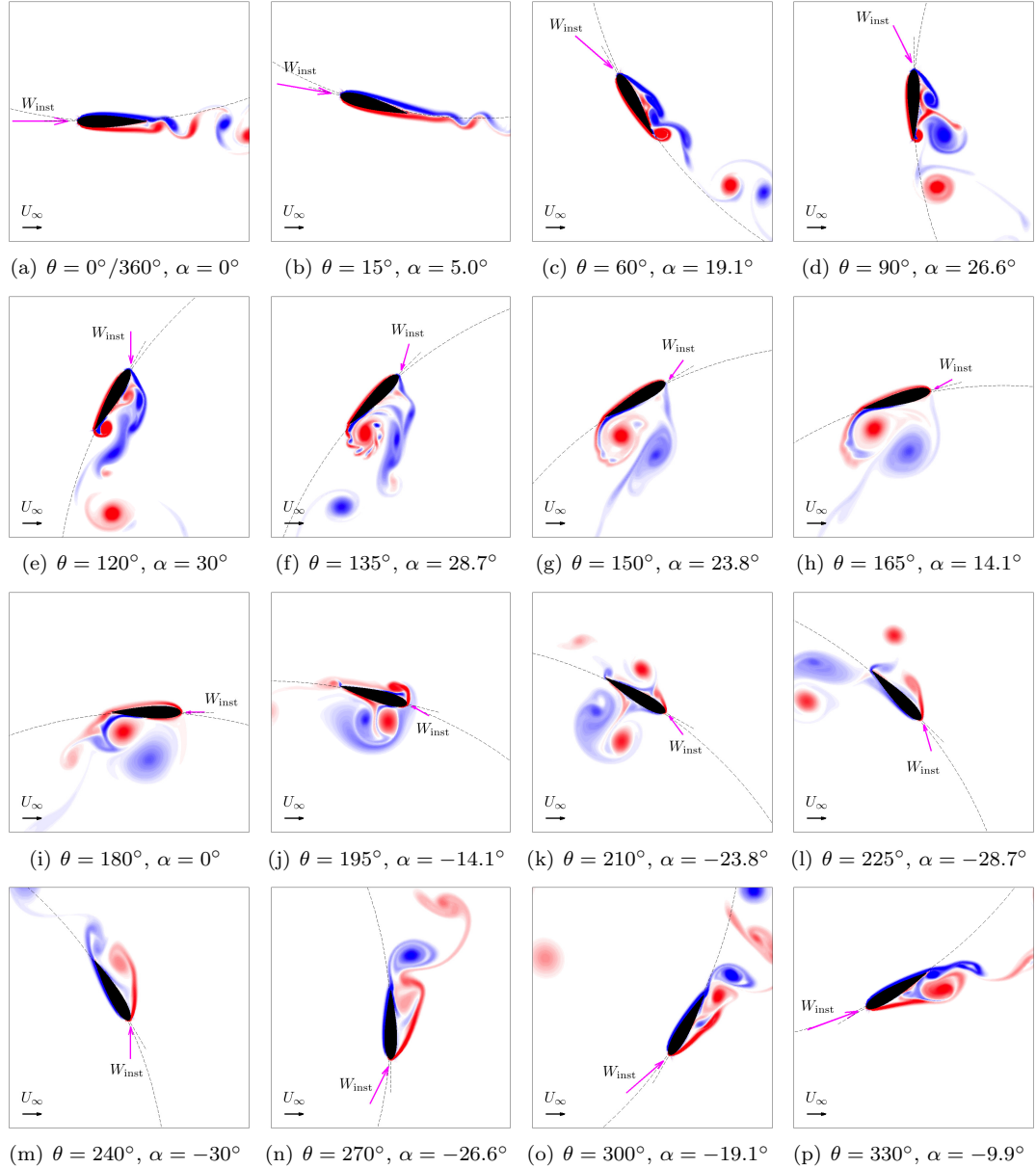
Figure 3.4: Vorticity field for a (clockwise rotating) VAWT at various azimuthal angles at $\lambda = 2$, $Ro = 1.5$, and $Re = 1500$. Negative and positive vorticity are plotted in blue and red contour levels, respectively, and all vorticity contour plots are using the same contour levels.

time airfoil reaches $\alpha = 5°$ (figure 3.4(b)). When the angle of attack increases further, the wake behind the airfoil starts to oscillate and vortex shedding commences. Dynamic stall then takes place, and is marked by the growth, pinch-off, and advection of an leading edge vortex (LEV) on the suction side of the airfoil (figures 3.4(c-e)). The vortices generated will propagate downstream into the wake of the VAWT or interact with the blades in the downwind half of a cycle.

When the angle of attack starts to decrease, a trailing edge vortex (TEV) develops (figure 3.4(f)). Bloor instability (Bloor, 1964) occurs in the trailing-edge shear layer at this Reynolds number, which resembles the convectively unstable Kelvin-Helmholtz instability observed in plane mixing layers. This TEV couples with a LEV to form a vortex pair that travels downstream together with the airfoil (figures 3.4(g-i)). This vortex pair interacts with the airfoil in the downwind half of a cycle (figures 3.4(j-l)), which was also observed by Ferreira et al. (2007).

When the blade rotates in the downwind half of a cycle, the angle of attack becomes negative. Vortices are now generated on the other side of the airfoil and shed into the wake of the VAWT (figures 3.4(j-p)). For a multi-bladed VAWT, when a blade is traveling in the downwind half of a cycle, it interacts with vortices generated upstream from other blades or from the wake it generated at an earlier time (figure 3.4(o)).

3.3   Comparison of VAWT and EPM

In this section, we compare flows around an airfoil undergoing the EPM and a single-bladed VAWT at $\lambda = 2$, $Ro = 1.5$, and $Re = 1500$. We are interested in the tangential force response of the blade over a cycle because the power output is proportional to the tangential force acting on the blade when VAWT operate at a constant tip-speed ratio. The tangential force acting on the blade can be written as a linear combination of lift and drag,

$$C_T = C_L \sin \alpha - C_D \cos \alpha = C_L \left(\sin \alpha - \frac{1}{C_L/C_D} \cos \alpha \right) \ , \tag{3.14}$$

where α is the angle of attack of the blade. From preliminary simulations, a three-bladed VAWT with $\ell = 4$ will be free-spinning with a time-averaged tip-speed ratio $\lambda = 0.95$ at $Re = 1500$, so that in the flow we are examining the average tangential force is expected to be negative. However, as the Reynolds number increases to the range where commercial VAWT usually operate, $Re \sim O(10^5 - 10^6)$, drag coefficient drops dramatically while the change in the lift coefficient is small. This leads to a large increase in the lift-to-drag ratio, C_L/C_D (Lissaman, 1983). Therefore, the

contribution of lift to the tangential force dominates at high Reynolds numbers. Moreover, the power of a VAWT is generated mostly in the upwind half cycle since large vorticity-blade interactions cancel out the driving torque in the downwind half cycle (Ferreira et al., 2007). Therefore, in this study we will focus on the lift in the upwind-half of a cycle.

In figure 3.5, the first two columns show the vorticity field at different azimuthal angles for EPM and VAWT motion. Figure 3.6 shows a comparison of the lift coefficient against dimensionless time and angle of attack for a single rotation and for the average of both lift coefficients over five cycles. Although there are still the remnants of earlier vortex shedding in the wake when the airfoil just returns to zero angle of attack (figure 3.5(a)), the flow reattaches by $\alpha = 5°$ (figure 3.5(b)), which leads to a smoothly increasing lift coefficient at low angle of attack. The differences in the lift coefficient between the EPM and VAWT are small (figure 3.6). As the angle of attack increases, dynamic stall commences (figures 3.5(c-e)), which leads to rapidly increasing lift. EPM and VAWT induced flows are quite similar, with just a small phase difference when the airfoils pitch up. They result in comparable lift throughout the upstroke phase.

When the downstroke phase starts (figures 3.5(e-f)), the development of a TEV leads to a decrease in lift. The aforementioned Bloor instability in the shear layer at the trailing edge produces high frequency fluctuations in the lift coefficient. For EPM, the TEV sheds into the wake and a secondary vortex (McCroskey et al., 1976) appears as the angle of attack decreases further (figure 3.5(g)), which results in a sudden increase in the lift coefficient. On the other hand, for VAWT, as described in section 3.2, this TEV couples with the LEV and forms a vortex pair that travels together with the airfoil (figures 3.5(g-h)). This generates high pressure on the suction side and further decreases the lift. This vortex pair is "captured" by the rotating airfoil. By analogy with flow observed in insect flight by Dickinson et al. (1999), we refer to this phenomenon as the wake-capturing of a vortex pair in VAWT. The wake-capturing occurs at a slightly different phase in each cycle and leads to a significant decrease in the average lift in the downstroke phase. In general, the lift of an airfoil undergoing the EPM is overestimated in the downstroke phase. Moreover, when this vortex pair travels downstream, it interacts with the airfoil in the downwind half of a cycle. This leads to a lift
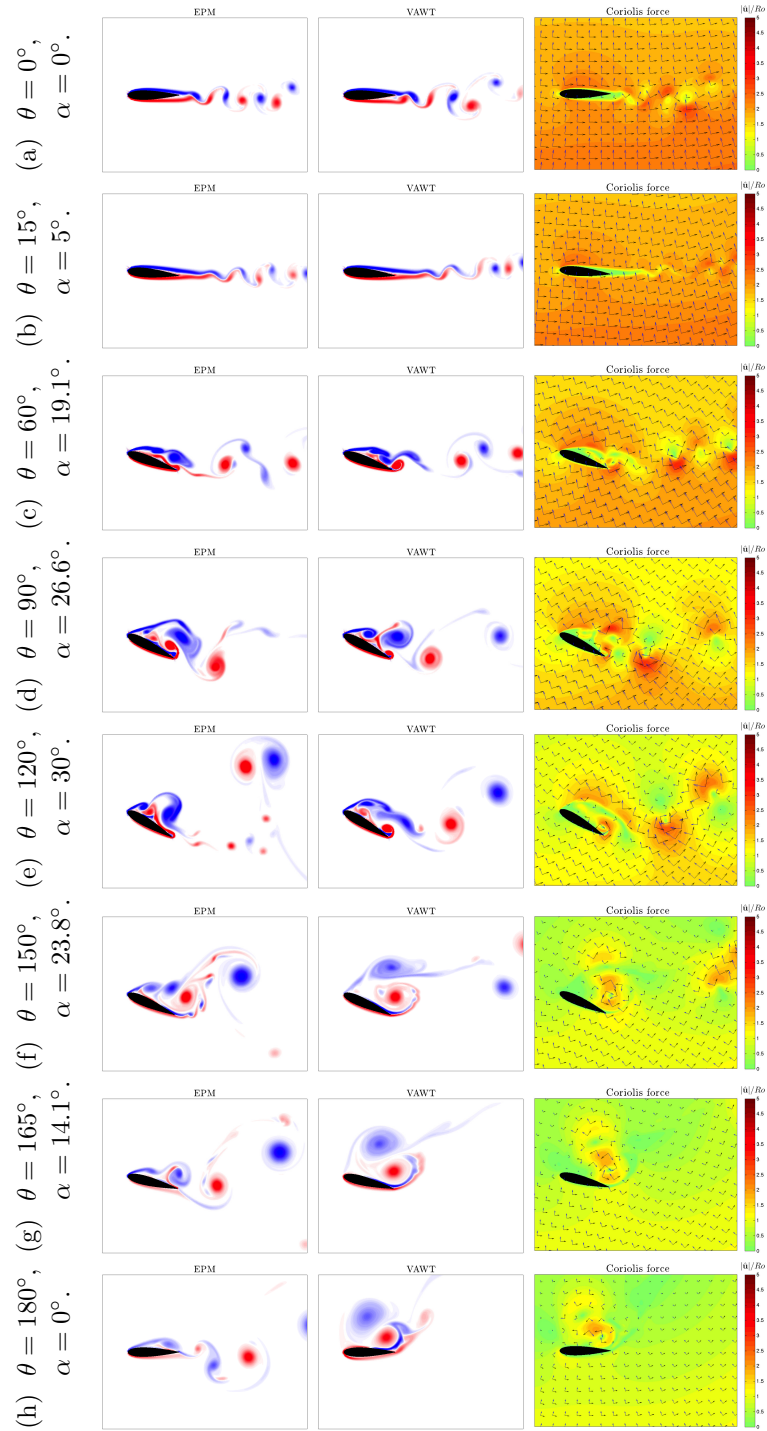
Figure 3.5: Vorticity field for EPM and VAWT and the Coriolis force for VAWT at various azimuthal angles. Negative and positive vorticity are plotted in blue and red contour levels, respectively, and all vorticity contour plots are using the same contour levels. In the Coriolis force plots, black arrows show the direction of velocity, blue arrows point the direction of the Coriolis force, and the color contour plots the magnitude of the Coriolis force.

(a) Lift coefficients over a cycle against azimuthal angle.

(b) Lift coefficients over a cycle against angle of attack.

(c) Phase-averaged lift coefficients over five cycles.
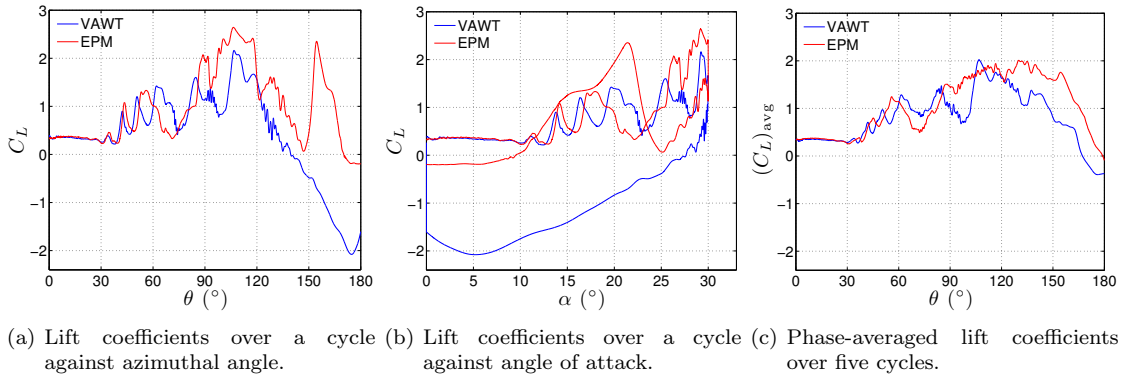
Figure 3.6: Comparing $C_{L,\text{VAWT}}$ and $C_{L,\text{EPM}}$ at $\lambda = 2$, $Ro = 1.5$, and $Re = 1500$.

coefficient with large fluctuations and small mean, as was also observed by Ferreira et al. (2007).

We can see from the second and third columns in figure 3.5 that the Coriolis force deflects the flow around the rotating airfoil in the clockwise direction. The magnitude of the Coriolis force acting on the background fluid decreases as the azimuthal angle increases. Therefore, the Coriolis force acting on the fluid around vortices becomes relatively important in the downstroke phase. A stronger Coriolis force is exerted on the fluid around the vortex pair, which deflects the fluid in such a way that the vortex pair travels with the airfoil (figures 3.5(f-h)).

3.4 Comparison with an airfoil undergoing a sinusoidal motion

Flows around an airfoil undergoing SPM and SSPM introduced in section 3.1 are compared with one undergoing EPM and in a VAWT. A comparison of the lift response at $\lambda = 2$ and 4, $Ro = 1.5$, and $Re = 1000$ is shown in figure 3.7.

At lower tip-speed ratio, $\lambda = 2$, in the upstroke phase, we can see that only $C_{L,\text{EPM}}$ is close to $C_{L,\text{VAWT}}$ at low angle of attack. $C_{L,\text{SPM}}$ and $C_{L,\text{SSPM}}$ overestimate the lift due to the overestimation of the pitch rate. In the downstroke phase, none of $C_{L,\text{EPM}}$, $C_{L,\text{SPM}}$, and $C_{L,\text{SSPM}}$ match the behavior of $C_{L,\text{VAWT}}$ because of the strong effect on lift of the wake-capturing that occurs in the flows. At higher tip-speed ratio, $\lambda = 4$, $C_{L,\text{SPM}}$ and $C_{L,\text{SSPM}}$ still overestimate the lift at the beginning of

the upstroke phase. Nevertheless, as the angle of attack increases, and after vortex shedding starts, differences between the four lift coefficients are relatively small. In the downstroke phase, behaviors of $C_{L,\text{EPM}}$, $C_{L,\text{SPM}}$, and $C_{L,\text{SSPM}}$ are close to that of $C_{L,\text{VAWT}}$ due to the low angle of attack.

We can see that, among all simplified motions, an airfoil undergoing the EPM is the best approximation to a rotating airfoil in a VAWT in the upstroke phase for the sub-scale Reynolds numbers considered in this study. However, it overestimates the lift coefficients in the downstroke phase due to its inability to predict the wake-capturing phenomenon.
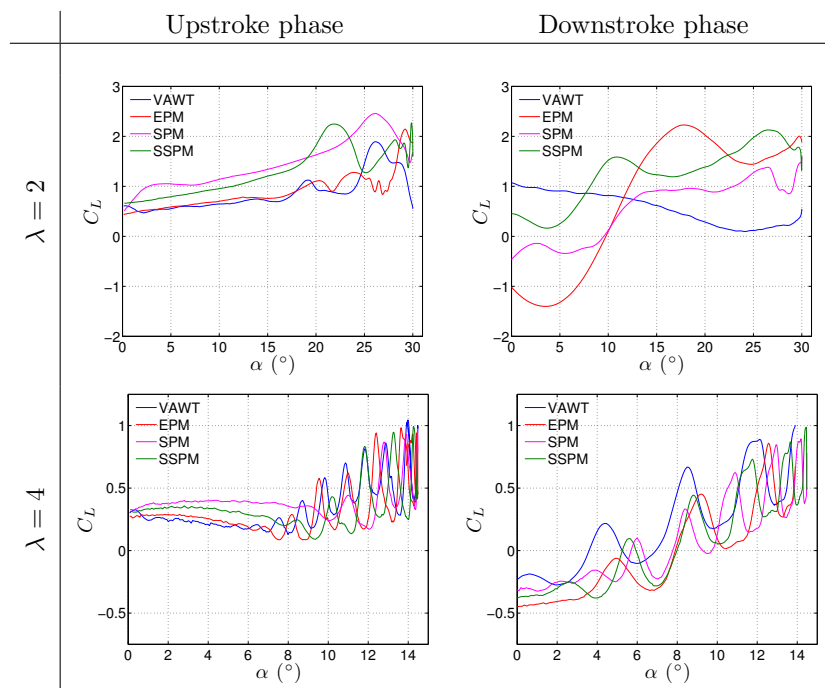
Figure 3.7: Lift coefficients of VAWT, EPM, SPM, and SSPM over a cycle at $\lambda = 2$ and 4, $Ro = 0.75$, and $Re = 1000$.

3.5   Effect of tip-speed ratio, Rossby number, and Reynolds number

In this section, the effect of tip-speed ratio, Rossby number, and Reynolds number on the flow in a VAWT is investigated to understand when wake-capturing occurs. We compare the simulations

of a rotating wing with a wing undergoing EPM. We examine the flows at tip-speed ratios $\lambda = 2$, 3 and 4, and Reynolds numbers $Re = 500$, 1000, and 1500. The corresponding lift coefficients with Rossby numbers $Ro = 0.75$, 1.00, and 1.25 are shown in figure 3.8.
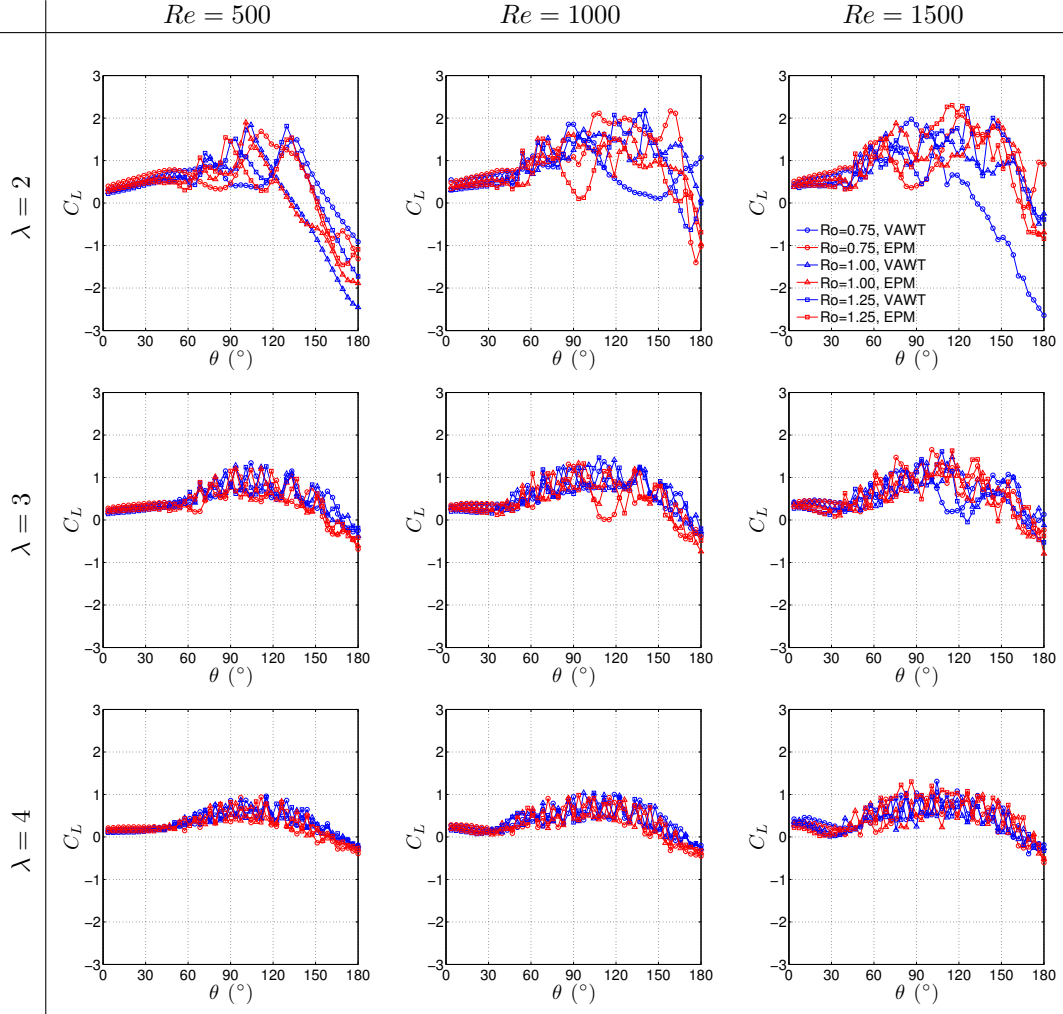
Figure 3.8: Comparing lift coefficients of VAWT and EPM over a cycle with $Ro = 0.75$, 1.00, and 1.25 at $\lambda = 2$, 3, and 4 and $Re = 500$, 1000, and 1500.

As the tip-speed ratio increases, the amplitudes of angle of attack variation and the corresponding lift decrease. Since the maximum angle of attack is slightly above the static stall angle of a NACA 0018 airfoil predicted by Morris and Rusak (2013), the lift coefficients of EPM is close to that of VAWT at $\lambda = 4$ for all Rossby numbers and Reynolds numbers examined. Therefore, EPM motion is a good approximation of VAWT at larger tip-speed ratios due to the low angle of attack. However, at lower tip-speed ratios, $C_{L,\mathrm{EPM}}$ remains close to $C_{L,\mathrm{VAWT}}$ only in the upstroke phase. In

the downstroke phase, the discrepancy in lift coefficients due to the wake-capturing effect becomes larger as Rossby number decreases and Reynolds number increases. As the VAWT rotates faster, on the one hand the wake-capturing effect is strengthened due to the intensifying Coriolis force, which corresponds to decreasing Rossby number; on the other hand, it is attenuated because of the decreasing amplitude of the angle of attack variation due to the increasing tip-speed ratio. Therefore, the growth of the discrepancy depends subtly on the increase of the rotating speed of the VAWT.

3.6 Comparisons with experiments

In this section, the simulation of a rotating airfoil in a VAWT is compared with phase-averaged PIV data from Ferreira et al. (2007) to probe the existence of wake-capturing at higher Reynolds numbers. Next, simulation results for VAWT and EPM (described in section 3.3) are compared with a phase-averaged data set from experiments on an airfoil undergoing the EPM performed by Dunne and McKeon (2014, 2015a,b) to further investigate the effect of the rotating frame, Reynolds number, and the Coriolis force.

3.6.1 Comparison with Ferreira et al. (2007)

To probe the existence of wake-capturing at higher Reynolds numbers, the vorticity field in VAWT ($Re = 1500$) for a single period is compared with phase-averaged PIV data from Ferreira et al. (2007)($Re \approx 10^5$) at $\lambda = 2$ and $Ro = 1(\ell = 4)$ in figure 3.9. The contours in gray are the phase-averaged vorticity field taken from the experiments. In figures 3.9(a-f), their phase-averaged field was filtered to plot only the LEV generated around $\theta = 72°$ and the plot represents a composite of overlaid fields from various azimuthal angles. Similarly, in figures 3.9(g-i), the contours in the gray scale show the filtered, phase-averaged TEV evolution. In order to make qualitative comparisons, our vorticity fields at the corresponding azimuthal angles are overlaid in the color scale on top of the results from the experiments. Our blue contours correspond to negative vorticity, which should be compared to the LEV-filtered PIV data in figures 3.9(a-f), while the red contours correspond to positive vorticity that should be compared to the TEV-filtered PIV data in figures 3.9(g-i).

(a) $\theta = 72°$

(b) $\theta = 90°$

(c) $\theta = 108°$

(d) $\theta = 133°$

(e) $\theta = 158°$

(f) $\theta = 223°$

(g) $\theta = 121°$
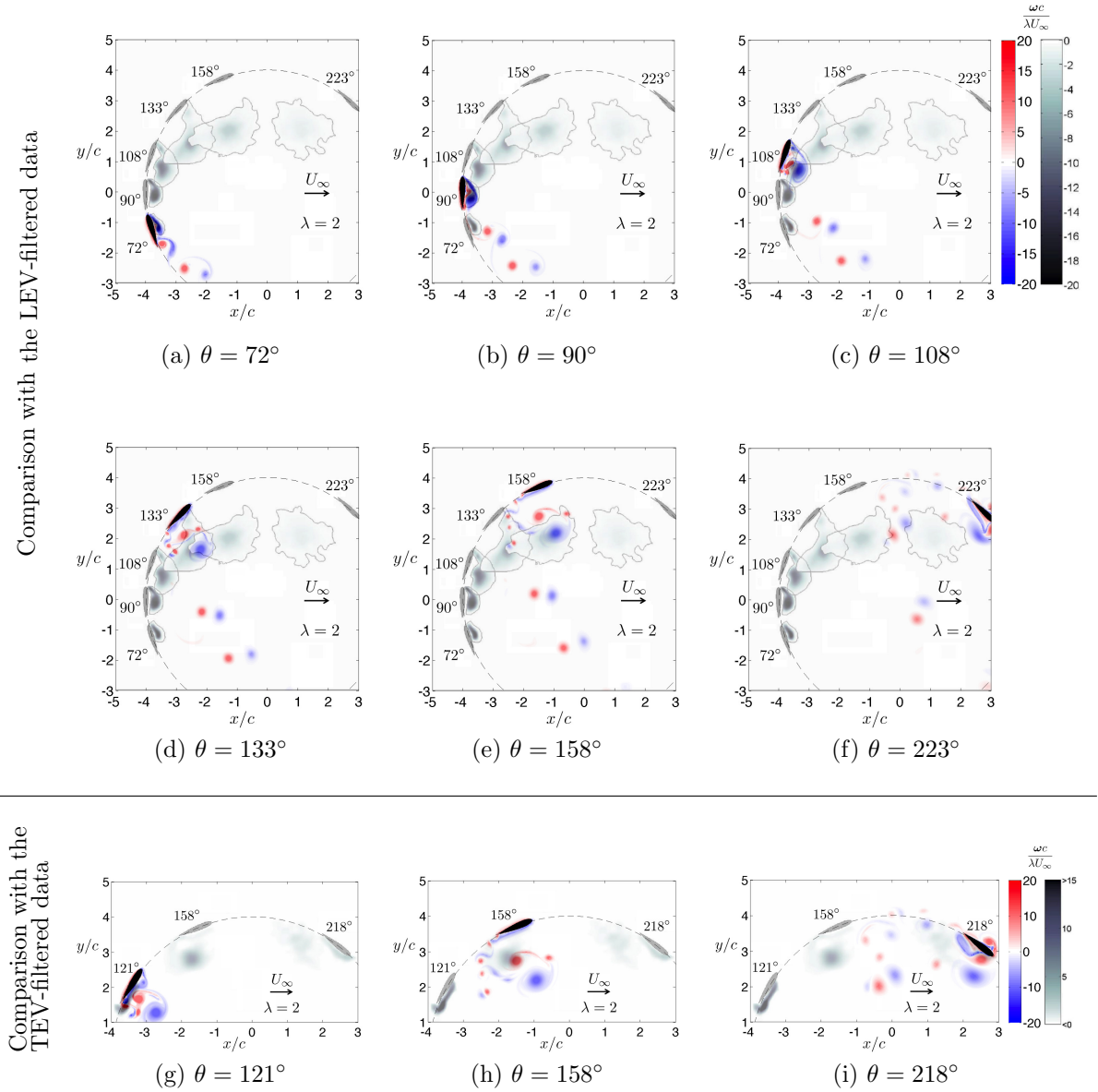
(h) $\theta = 158°$

(i) $\theta = 218°$

Figure 3.9: The comparison of the vorticity fields of the LEV-filtered (a-f) and TEV-filtered (g-i) phase-averaged PIV data from Ferreira *et al* (gray scale), and of the corresponding VAWT simulations (color scale) at $\lambda = 2$ and $Ro = 1(\ell = 4)$ at various azimuthal angles.

The trajectories of the LEV and TEV from Ferreira et al. seem to be reasonably captured by the simulation in the upwind half of a cycle. The disagreement in figures 3.9(f) and 3.9(i) may be due to strong vortex-blade and vortex-vortex interactions in the downwind half of a cycle. A LEV is generated around $\theta = 72°$ and wake-capturing occurs around $\theta = 90°$, which forms a vortex pair traveling with the blade (figures 3.9(a-c)). The vortex pair then detaches around $\theta = 133°$ and propagates downstream (figures 3.9(d-f)). The location of the vortex pair composed of the phase-averaged LEV and TEV agrees with the current simulation, especially at $\theta = 158°$ (figures 3.9(e) and 3.9(h)). The qualitative agreement in the upwind half of a cycle suggests that wake-capturing may also be occurring in Ferreira et al.'s experiment.

3.6.2   Comparison with Dunne and McKeon (2014, 2015a,b)[1]

Simulation results on airfoils undergoing VAWT and EPM motions at $Re = 1500$ described in section 3.3 are compared with phase-averaged data set from experiments on an airfoil undergoing the EPM performed by Dunne and McKeon (2014, 2015a,b) in order to explore the effect of Reynolds number and the rotating frame. The experiments were performed in a water tunnel at Reynolds numbers near turbine conditions of 10^5 and the setup of experiments are described in more detail in Dunne and McKeon (2014, 2015a,b). In order to distinguish between the computational results and experimental data, Dunne and McKeon introduced the nomenclature $\mathbf{EPM}^E$ and $\mathbf{EPM}^C$ to denote EPM from experiment and computation, respectively, and $\mathbf{VAWT}^C$ to denote VAWT from computation.

Figure 3.10 reproduced from Dunne et al. (2015) shows the comparison of $\mathbf{EPM}^E$ with $\mathbf{EPM}^C$ and $\mathbf{VAWT}^C$ at various azimuthal angles. α_+, α, and α_- denote the angles of attack when the pitch rates are positive, zero, and negative, respectively. As expected, vortices appearing at all angles of attacks in the simulation are much more coherent because of the low Reynolds number. Furthermore, since the experimental data is an ensemble average of multiple experiments, the coherent vortex shedding apparent at $\alpha_+ = 0°$ is smeared out in experimental results and the vorticity generated

---

[1]This work was presented as a collaborative effort between the author with advisor Tim Colonius, and collaborators Reeve Dunne and Beverley McKeon at the International Conference on Wakes, Jets, and Separated Flows in June, 2015, Stockholm, Sweden, and is published as Dunne et al. (2015)
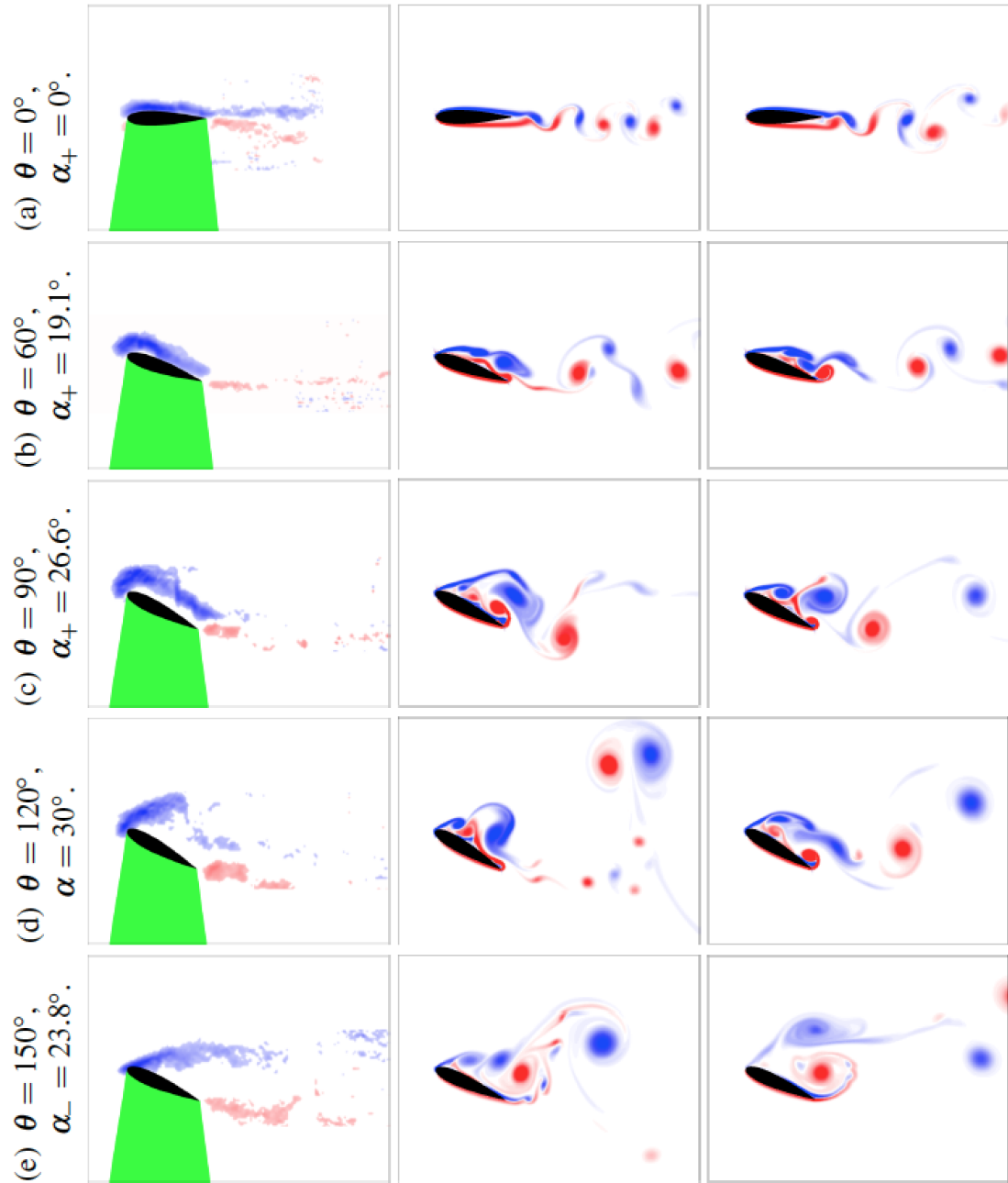
Figure 3.10: Vorticity contours of $\mathbf{EPM}^E$ (left), $\mathbf{EPM}^C$ (middle), and $\mathbf{VAWT}^C$ (right). Red and blue contours indicate positive and negative vorticity, repectively, and green area indicates the PIV laser shadow. Figure reproduced from Dunne et al. (2015).

from the leading edge is significantly weakened by this phase averaging. Apart from these Reynolds numbers and experimental differences, the flow evolution is similar between three cases. At $\alpha_+ = 0°$ the flow is attached and a symmetrical wake corresponding to vortex shedding is seen behind the airfoil (figure 3.10(a)). At $\alpha_+ = 19°$ a LEV begins to form, indicated by increased intensity in experiment and visible as a distinct structure in computation (figure 3.10(b)). At $\alpha_+ = 27°$ the LEV grows even stronger in the experiment and the flow has just begun to separate; however, in both computations the LEV has moved downstream, indicating that flow separation occurs slightly earlier at low Reynolds number (figure 3.10(c)). At maximum $\alpha = 30°$ the flow is fully separated in both experiment and computation with a shear layer at the leading edge visible in the experiment, and continuously large scale vortex shedding from the leading and trailing edges in the computation (figure 3.10(d)). The trajectories of the shed vortices between $\mathbf{EPM}^C$ and $\mathbf{VAWT}^C$ are different due to the Coriolis forces as discussed in section 3.3. Finally at $\alpha_- = 24°$, while in $\mathbf{EPM}^E$ and $\mathbf{EPM}^C$ vortices can be seen to shed from the leading and trailing edges, the aforementiaoned wake-capturing phenomenon is seen in $\mathbf{VAWT}^C$ (figure 3.10(e)).
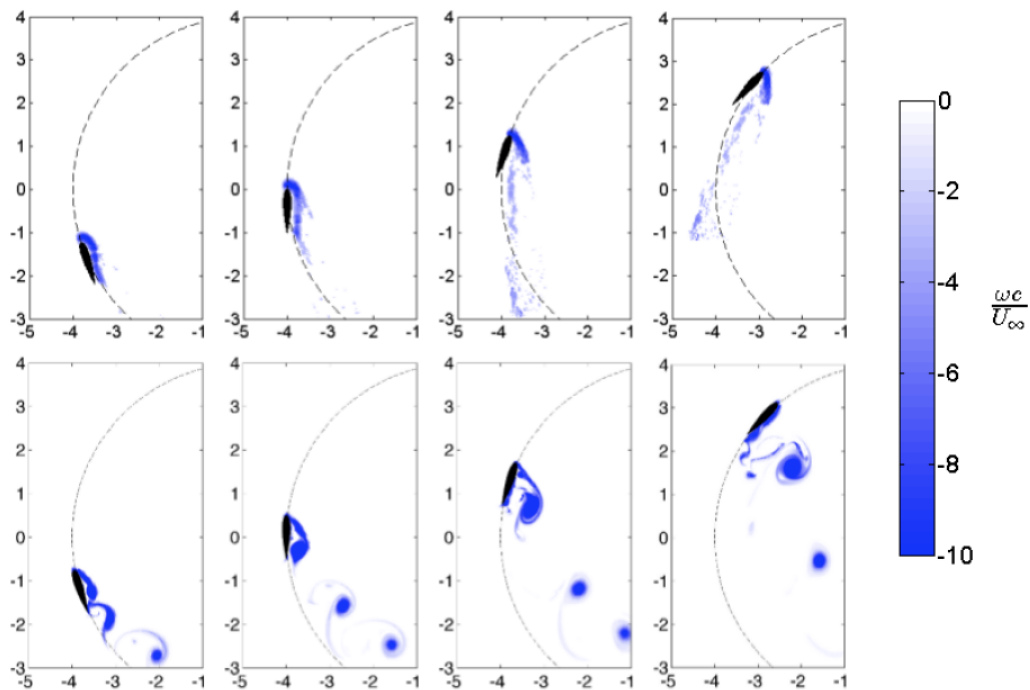
Figure 3.11: Clockwise vorticity contours from $\mathbf{EPM}^E$ (top) and $\mathbf{VAWT}^C$ (bottom) at $\theta = 70°$, $90°$, $108°$, and $133°$ respectively from left to right. Figure reproduced from Dunne et al. (2015).

Figure 3.11, which is also reproduced from Dunne et al. (2015), shows the vortices generated from the leading edge for $\mathbf{EPM}^E$ and $\mathbf{VAWT}^C$ at various points in a cycle in the turbine reference frame. Similar to figure 3.10, vortices are more coherent in the computation due to the lower Reynolds number. The effect of experimental and turbine reference frame can be seen clearly by the trajectories of the vortices. The vortices in the computation convect from left to right with the turbine relative freestream, while the vortices in experiment convect behind the airfoil with the blade relative freestream. However, agreement is good at the blade level and immediately behind the blade.

3.7 Decoupling the effect of surging, pitching, and rotation

In order to understand whether the Coriolis effect has strong coupling with the incoming velocity and angle-of-attack variations, we independently examine airfoils undergoing the decoupled pitching and surging motion associated with VAWT and EPM.

3.7.1 Airfoil undergoing only surging motion

We examine a surging motion with fixed angles of attack of 15 and 30 degrees at $\lambda = 2$, $Ro = 1.5$ ($k = 1/6$), and $Re = 1500$. A rotating airfoil undergoing only the surging motion of a VAWT is achieved by pitching the airfoil around the leading edge simultaneously as it rotates so that the angle of attack is fixed with respect to the incoming velocity. For an airfoil surging at an angle of attack of 15°, lift coefficients are shown in figure 3.12(a). We can see that dynamic stall is relatively stable and no wake-capturing phenomenon is observed. Moreover, from the analysis by Choi et al. (2015), when the reduced frequency is low enough, the flow can be approximated as quasi-steady, which results in both lift coefficients for VAWT and EPM fluctuating about a slowly increasing mean value. For the case of $\alpha = 30°$, lift coefficients are shown in figure 3.12(b). The flow is well separated so that there is no stationary vortex shedding. Moreover, no wake-capturing phenomenon is observed in the flow.

(a) $\alpha = 15°$ (b) $\alpha = 30°$

Figure 3.12: Comparing lift responses of airfoils undergoing only surging motion at $\lambda = 2$, $Ro = 1.5$, and $Re = 1500$.

3.7.2 Airfoil undergoing only pitching motion

We consider a pitching motion in a freestream velocity $W_{\mathrm{avg}} = \lambda U_\infty$ at $\lambda = 2$, $Ro = 1.5$ and $Re = 1500$. A rotating airfoil undergoing only the pitching motion in a VAWT is achieved by rotating an airfoil in a VAWT without the external free stream and simultaneously pitching it around the leading edge with the exact angle of attack variation. The corresponding lift coefficients are shown in figure 3.13. We can see dynamic stall in both lift coefficients as angle of attack increases. However, there is no wake-capturing.

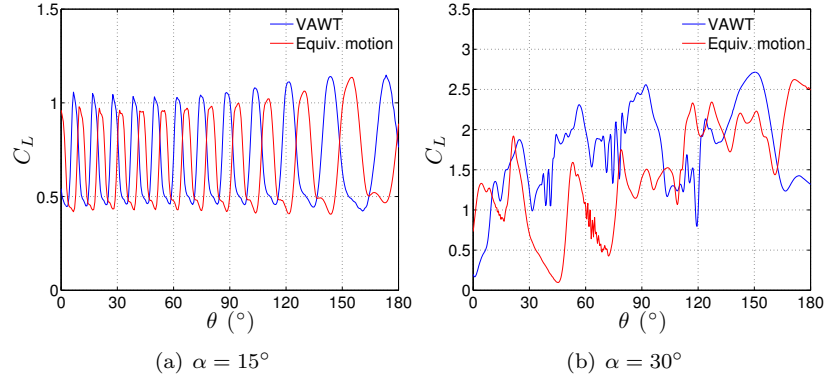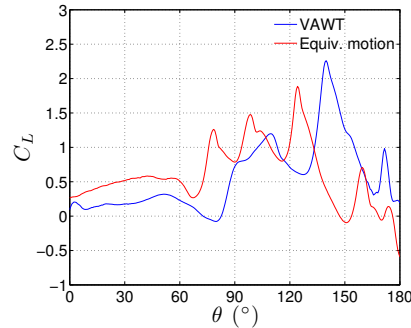

Figure 3.13: Comparing lift responses of airfoils undergoing only pitching motion at $\lambda = 2$, $Ro = 1.5$, and $Re = 1500$.

The wake-capturing effect is therefore only present when pitching, surging, and the Coriolis force are all present.

3.8 Open-loop control on the wake-capturing phenomenon

From the discussion in sections 3.3 and 3.5, the wake-capturing of vortex pair leads to a large decrease in lift. In order to improve the corresponding implied loss in power production, we apply a open loop control on dynamic stall in a VAWT. Inspired by Greenblatt et al. (2013), an actuator modeled as a bodyforce introduced by Joe et al. (2011) is placed on the suction surface blowing the fluid tangent to the surface to control dynamic stall vortices.

C_μ is the momentum coefficient that defines the momentum injection added by the forcing. For an actuator with the width estimated as the grid spacing, Δx, which injects a jet with average velocity, $\bar{u}_\text{jet}$, the momentum coefficient is

$$C_\mu = \frac{\bar{u}_\text{jet}^2 \Delta x}{\frac{1}{2} U_\infty^2 c} \ . \tag{3.15}$$

A bodyforce with strength C_μ is placed at different actuation locations to control the baseline flow with wake-capturing phenomenon at $\lambda = 2$, $Ro = 1.5$, and $Re = 1500$. The corresponding lift coefficients are shown in figure 3.14. C_μ and the actuation locations that are examined and the corresponding percentage changes in the averaged lift over the upwind half of a cycle are summarized in table 3.2. The actuation location is measured by how far away from the leading edge.

Since the wake-capturing phenomenon only occurs in the downstroke phase, the control initiates at an azimuthal angle of 90°and terminates at 180°. We can see that the best improvement is obtained with the actuator placed at 30% of the chord length from the leading edge. Based on these preliminary simulations, with C_μ above a certain threshold, say 0.02 in this case, the control is able to remove the wake-capturing of vortex pair and increase the lift generation significantly in the downstroke phase. Figure 3.15 shows the vorticity field of the baseline flow and the controlled flow with an actuator placing at 30% of the chord length from the leading edge with $C_\mu = 0.02$. We can see that the actuation successfully removes the wake-capturing of vortex pair in the downstroke phase.

(a) Actuator placed at 10%c

(b) Actuator placed at 20%c

(c) Actuator placed at 30%c
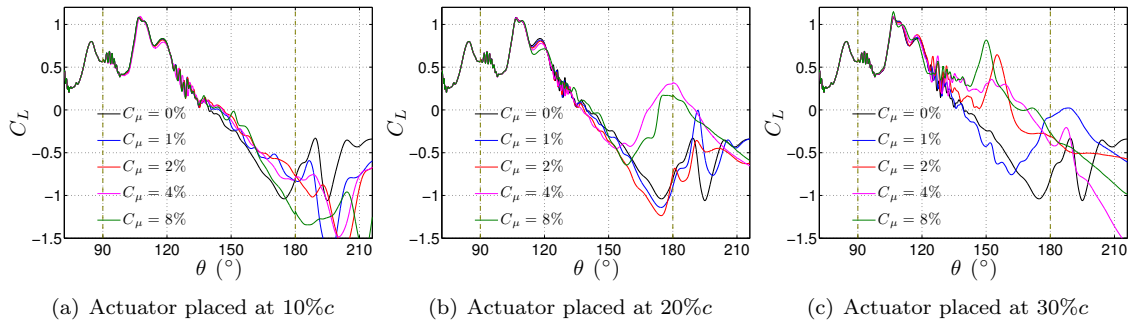
Figure 3.14: Open loop control on wake-capturing phenomenon with actuator placing at 10%, 20%, and 30% of the chord length from the leading edge at $\lambda = 2$, $Ro = 1.5$, and $Re = 1500$.

Table 3.2: Parameters examined in the open-loop control are summarized. The actuation location is measured by the ratio of the distance from the leading edge to the chord length.

actuation location	C_μ	ΔC_L (%)
10% c	0.01	17
10% c	0.02	23
10% c	0.04	15
10% c	0.08	10
20% c	0.01	-9
20% c	0.02	-19
20% c	0.04	40
20% c	0.08	33
30% c	0.01	13
30% c	0.02	71
30% c	0.04	82
30% c	0.08	94

$\theta = 120°, \alpha = 30°$ $\theta = 150°, \alpha = 23.8°$ $\theta = 165°, \alpha = 14.1°$ $\theta = 180°, \alpha = 0°$
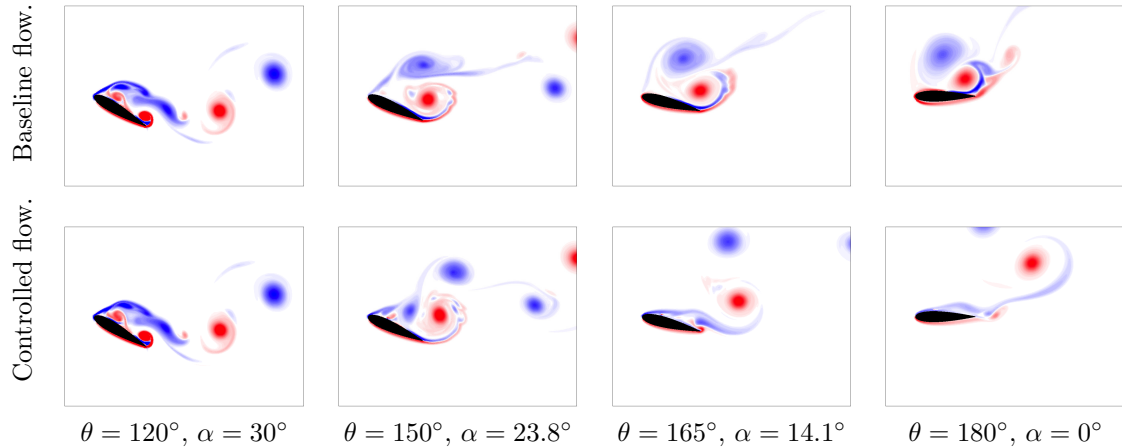
Figure 3.15: Vorticity field of the baseline flow and the controlled flow with an actuator placing at 30% of the chord length from the leading edge with $C_\mu = 0.02$.

3.9   Summary

In simulating the flow around a single-bladed VAWT, we have observed an interesting wake-capturing phenomenon that occurs during the pitch-down portion of the upstream, lift-generating portion of the VAWT cycle. This phenomenon leads to a substantial decrease in lift coefficient due to the presence of a vortex pair traveling together with the rotating airfoil. Our results show that as tip-speed ratio and Rossby number are reduced and Reynolds number is increased, this flow feature persists and grows stronger, as it results in a larger decrease in lift coefficient. Therefore, the growth of this features depends subtly on the increase of the rotating speed of the VAWT, which on the one hand is strengthened due to the intensifying Coriolis force. On the other hand, it is attenuated because of the decreasing amplitude of the angle of attack variation. Moreover, although our study is restricted to two dimensional flow at relatively low Reynolds numbers, the qualitative agreement of the LEV and TEV evolutions with Ferreira et al.'s experiment suggests that this feature may persist in real applications. The corresponding decrease in efficiency could be improved by implementing flow control (e.g. blowing) to remove this flow feature.

An equivalent planar surging-pitching motion was introduced in order to isolate the Coriolis effect on dynamic stall in a VAWT. We also examined simplified planar motions consisting of si-nusoidally varying pitch and surge. Except at the beginning of the pitch-up motion, all of the

simplified motions are good approximations to VAWT motion at sufficiently high tip-speed ratios since the corresponding maximum angle of attack is close to or lower than the stall angle of the blade. However, at low tip-speed ratios, while the equivalent planar motion captures the pitch-up part of the cycle, all the motions show significant differences in forces during the pitch down motion. The results show that the equivalent motion is a good approximation to a rotating airfoil in a VAWT in the upstroke phase where the Coriolis force has a relatively small effect on vortices. However, it overestimates the average lift coefficient in the downstroke phase by eliminating the aforementioned wake-capturing. Moreover, the computational results of VAWT and EPM a low Reynolds number of 1500 were compared with the experimental result of EPM at a high Reynolds number of 10^5 from the water-tunnel experiments performed by Dunne and McKeon (2014, 2015a,b) in Dunne et al. (2015). The flow was shown to develop similarly prior to separation, but kinematics of vortices shed post separation were reference-frame dependent due to the wake-capturing.

We further investigated the flow by decomposing the planar motion into surging- and pitching-only motions. We only observe wake-capturing when the combination of surging, pitching, and rotation are present, which suggests this feature is associated with an unique combination of angle of attack variation, instantaneous velocity variation, and the Coriolis effect.

Chapter 4

Numerical investigation of the self starting of a VAWT

In this chapter, we focus on investigating the starting capability of a VAWT. The motion of the VAWT is coupled with the aerodynamic forces exerted on the blades. A three-bladed VAWT with NACA0018 blades is started at various Reynolds numbers and density ratios. Comparisons of flow-driven and motor-driven VAWT are made with the water-tunnel experiments performed by Araya and Dabiri (2015) to validate the load model. A simple quasi-steady model is proposed to analyze the starting torque of a three-bladed VAWT. The total torque and blade torque distributions are compared between VAWT with various number of blades. Based on the torque distributions of a single-bladed VAWT with various static pitch angles, an optimal pitch distribution is proposed.

4.1 Simulation setup

Figure 4.1 shows the schematic of a VAWT with three NACA0018 airfoils as blades rotating with an angular velocity, Ω, about point O in a freestream with velocity, U_∞, coming from the left. The azimuthal angle, θ, is defined as the angle between the black blade and the vertical axis as illustrated and θ_0 is the initial value of the azimuthal angle, i.e., $\theta_0 = \theta(t^* = 0)$.

In order to simulate the starting of a VAWT, two-dimensional incompressible Navies-Stokes
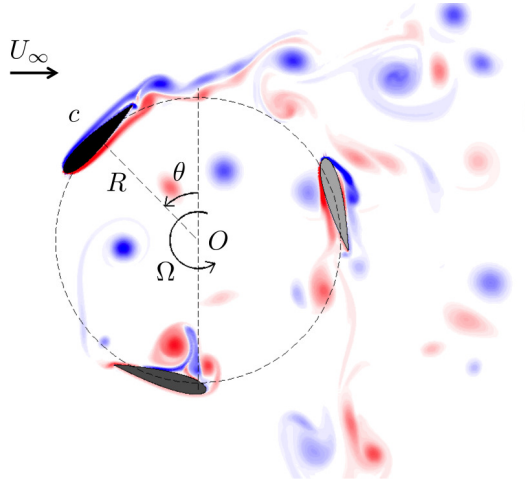
Figure 4.1: Schematic of a rotating three-bladed VAWT and the computational domain

equations are coupled with the equation of the motion of the VAWT:

$$N_b I_O \frac{d\Omega}{dt} = \tau_{fb} - \tau_L \; , \tag{4.1}$$

where N_b is the number of the blades, I_O is the moment of inertia of the blade about the rotation center of the VAWT, τ_{fb} is the moment exerted by the fluid about the rotation center of the VAWT, and τ_L is torque generated by a load. The moment of inertia of the blade, I_O, is obtained by computing the second moment of mass with respect to point O,

$$I_O = \int_V \rho_b(\mathbf{x})|\mathbf{x}|^2 \; d^3\mathbf{x} \; , \tag{4.2}$$

where V is the volume of the blade, $\mathbf{x}$ is the position vector from point O to a point in the blade, and $\rho_b(\mathbf{x})$ is the density field of the blade. τ_{fb} is determined by the aerodynamic forces exerted by the fluid on the blade, whose behavior is complicated due to the inherently unsteady flow around the rotating blades and strong blade-vorticity interaction in the downwind half of a cycle. Finally, a simple load model is used for the torque:

$$\tau_L = F \, \Omega \; , \tag{4.3}$$

where F is the friction coefficient of the load.

Besides tip-speed ratio (equation (3.1)), solidity (equation (3.3)), and Reynolds number (equation (3.4)), another dimensionless parameter is introduced to systematically investigate the self-starting capability of a VAWT:

$$\text{density ratio:} \quad \phi_\rho = \frac{\rho_e}{\rho} \;, \tag{4.4}$$

where ρ is the density of the fluid, and ρ_e is the effective density of the blade, which is defined by

$$\rho_e = \frac{\int_V \rho_b(\mathbf{x})|\mathbf{x}|^2 \; d^3\mathbf{x}}{\int_V |\mathbf{x}|^2 \; d^3\mathbf{x}} = \frac{I_O}{\int_V |\mathbf{x}|^2 \; d^3\mathbf{x}} \;. \tag{4.5}$$

The radius of the VAWT is fixed at $R = 1.5 \; c$ in the present study in order to compare with experiments performed by Araya and Dabiri (2015). Therefore, the corresponding solidity is $\sigma = \frac{N_b}{3\pi} \approx 0.106 \times N_b$ for VAWT with N_b blades. From equation (4.1), we can see that when investigating the self-starting of a VAWT, the tip-speed ratio is a function of the other three parameters and the friction coefficient of the load, i.e.,

$$\lambda = \lambda(Re, \phi_\rho, \sigma, F) \;. \tag{4.6}$$

As in Chapter 3, IBPM introduced in section 2.2 is used to compute two-dimensional incompressible flows in an airfoil-fixed reference frame with appropriate forces added to the momentum equation to account for the non-inertial reference frame as illustrated in section 2.1. Moreover, equation (4.1) is coupled with the flow using PCM introduced in section 2.3. All ensuring computations use six 800×800 grids, which corresponds to $\Delta x = 0.005$. The coarsest grid extends to 128 chord lengths in both the transverse and streamwise directions of the VAWT. The time step, Δt, is chosen to make CFL number less than 0.4. Again, VAWT are investigated numerically at low Reynolds number, $Re \sim O(10^3)$, in order to have more understanding of the starting of a VAWT in relatively short computational time. Although density ratio of the real VAWT is of $O(10^2)$ (Hill et al., 2009),

as we will discuss in section 4.2, VAWT with density ratio this high are not able to self-start at low

Reynolds numbers of $O(10^3)$. Therefore, VAWT with low density ratios, $\phi_\rho \sim O(1)$, are investigated

in order to explore the effect of density ratio on the starting of a VAWT at low Reynolds number.

4.2 Starting of a three-bladed VAWT at various Reynolds numbers and density ratios

We begin with examining a three-bladed VAWT with $\phi_\rho = 1$ and $F = 0$ starting from $\theta_0 = 0°$ at various Reynolds numbers. Figure 4.2 shows the tip-speed ratio, which serves as the non-dimensionalized angular velocity, as a function of Reynolds number and the azimuthal angle history.

(a) Tip-speed ratio as a function of Reynolds number. Error bars represent one standard deviation.

(b) Azimuthal angle history.
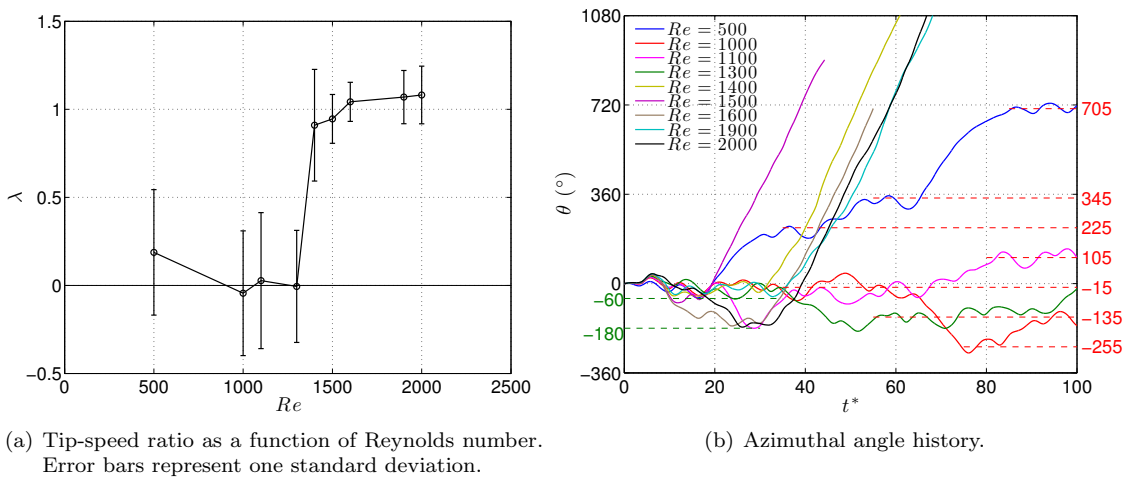
Figure 4.2: Azimuthal angle history of a VAWT with $\phi_\rho = 1$ and $F = 0$ starting from $\theta_0 = 0°$ at various Reynolds number.

First, from figure 4.2(a), there exists a critical Reynolds number between 1300 and 1400 below

which the VAWT does not start itself. Above $Re = 1400$ the tip-speed ratio slightly increases as

Reynolds number increases. Second, $\theta_0 = 0°$ does not seem to be a favorable orientation for starting.

At the beginning of the simulation, VAWT initially rotates in the opposite direction (clockwise) and

then starts to rotate in the counter-clockwise direction, which is the correct direction given the

orientation of the blades. Most interestingly, indicated by the green dashed lines in figure 4.2(b), we

can see that the onset of counter-clockwise rotation commences when one of the blades is around

$\theta = 60°$. On the other hand, VAWT that are unable to self-start oscillate around an equilibrium orientation with one of the blades about $\theta = 105°$, which is indicated by the red dashed lines in figure 4.2(b). Further analysis on these behaviors using the starting torque are shown in section 4.4.

We further investigate the three-bladed VAWT with $F = 0$ and $\phi_\rho = 1, 2, 3$, and 4 starting from $\theta_0 = 60°$ at $Re = 2000$. Figure 4.3 shows the corresponding tip-speed ratio and azimuthal angle histories. From figure 4.3(b), we can see that when starting from $\theta_0 = 60°$, VAWT that are able to self-start will rotate in the correct direction from the beginning. From figure 4.3(b), we observe a critical density ratio between 3 and 4 that VAWT with density ratios higher than the critical value fail to start at $Re = 2000$. When VAWT are able to start, those with a lower density ratio reach a stationary rotation faster but with a larger fluctuation in tip-speed ratio due to lower moment of inertia. Nevertheless, after they start, the average tip-speed ratio of each VAWT is roughly the same. This indicates that the averaged properties of the stationary state depend mainly on Reynolds number but not density ratio.
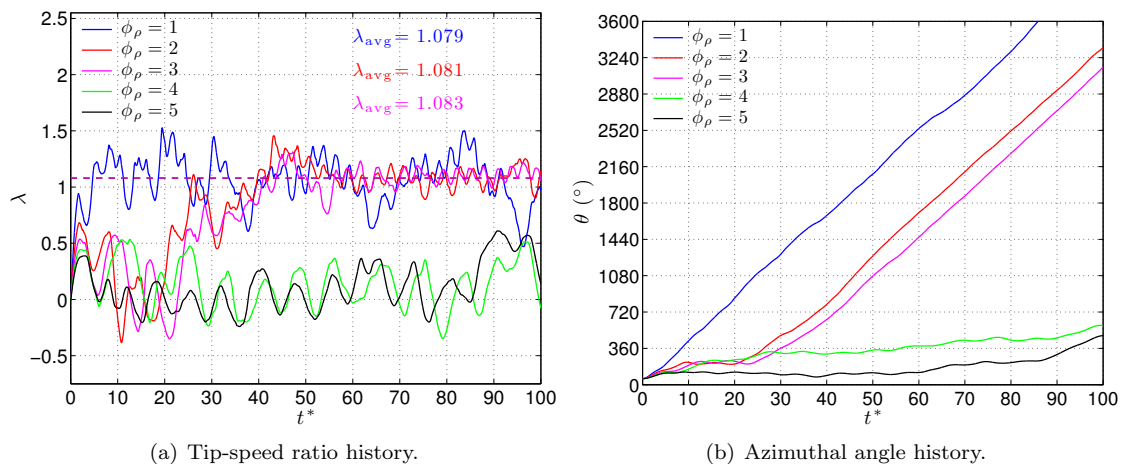

(a) Tip-speed ratio history.

(b) Azimuthal angle history.

Figure 4.3: Histories of angular velocity and azimuthal angle of VAWT with $F = 0$ and $\phi_\rho = 1, 2, 3$, and 4 starting from $\theta_0 = 60°$ at $Re = 2000$.

4.3 Flow-driven VAWT and the comparison with motor-driven VAWT

Based on the discussions in section 4.2, the angular velocity of a VAWT driven by the flow, which can be characterized as a function of Reynolds number and density ratio, is determined by the aerodynamic forces exerted on the blades as in the field. However, prescribing the motion of a VAWT within a flow is common among both experimental and numerical investigations. In this section, we numerically investigate the difference between flow-driven and motor-driven VAWT by comparing power coefficients of flow-driven and motor-driven three-bladed VAWT. Moment coefficients are qualitatively compared with the torque of flow/motor-driven VAWT measured from experiments performed by Araya and Dabiri (2015). The experiments were performed in a water tunnel at Reynolds numbers of 10^4 and the setup of experiments are described in more detail in Araya and Dabiri (2015).

Figure 4.4 shows the comparison of the power coefficients of a motor-driven VAWT at various tip-speed ratios and flow-driven VAWT with different friction coefficients at $Re = 2000$. In each subfigure, we show the motor-driven power coefficient in black with the error bar showing the corresponding fluctuation in power coefficient at that tip-speed ratio and the power coefficient of a flow-driven VAWT with $F = 0$ over three cycles in green. In figures 4.4(b), (c), and (d), the power curves of flow-driven VAWT with $F = 0.1, 0.2,$ and 1.0 are shown in purple, respectively. The motor-driven power coefficient curve shows two equilibria at $\lambda \approx 0.7$ and $\lambda \approx 1.1$ where the VAWT generates zero power. Since the slope of the power coefficient curve is negative at $\lambda \approx 1$, it is a stable equilibrium. As expected, the flow-driven VAWT with $F = 0$ generates almost zero power and is just free-spinning at an averaged tip-speed ratio $\lambda_{\mathrm{avg}} \approx 1.08$. As F increases, if the VAWT is able to rotate continuously, it operates at a lower averaged tip-speed ratio and generates a higher averaged power as shown in figures 4.4(b) and 4.4(c). However, when F is too large, say, $F = 1.0$, the VAWT is unable to sustain rotation and the power output goes to zero as the turbine oscillates about a stable equilibrium with $\lambda \approx 0$ as shown in figure 4.4(d).
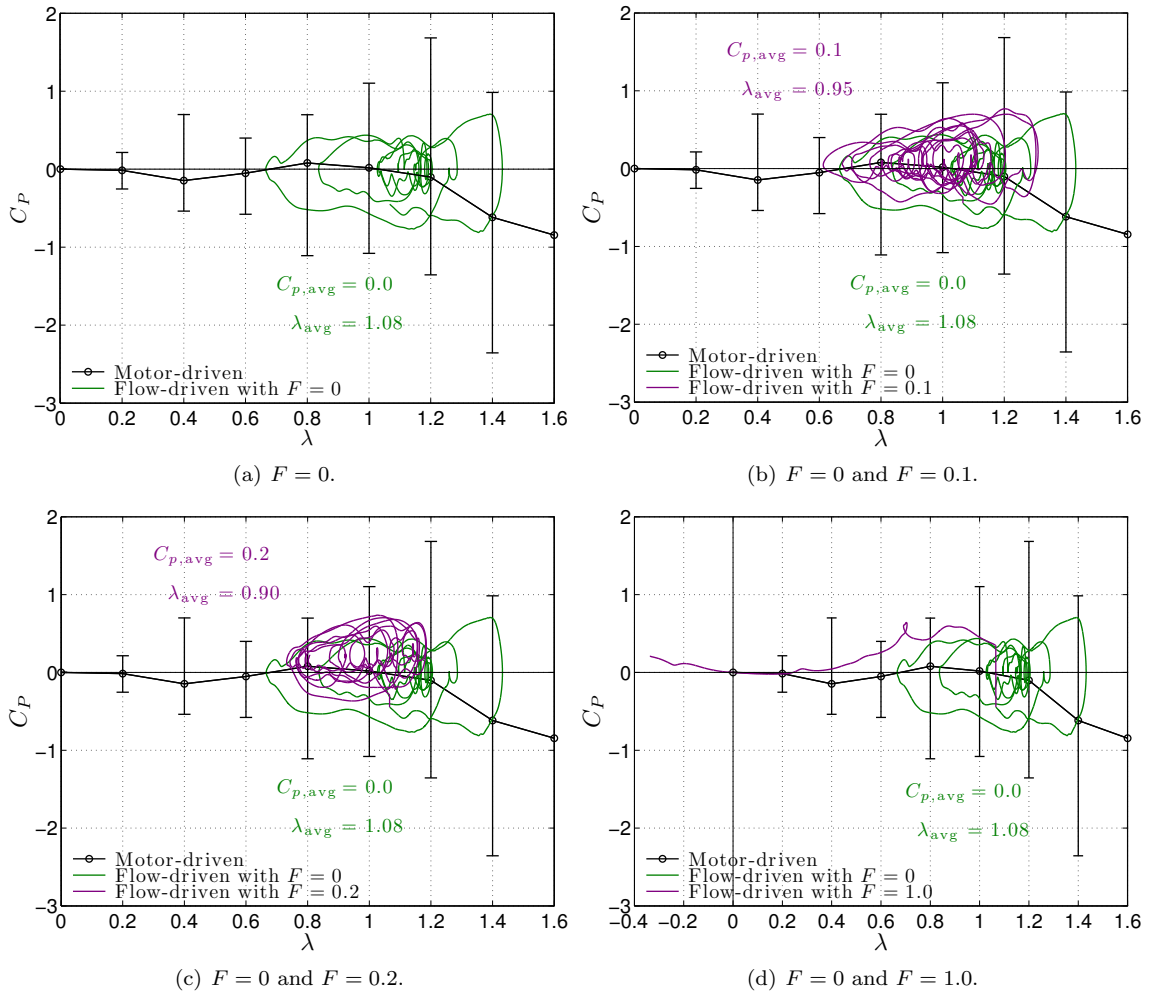
Figure 4.4: Comparisons of power curves of a three-bladed VAWT motor-driven at various tip-speed ratios and flow-driven with $\phi_\rho = 1$ and various friction coefficients at $Re = 2000$.
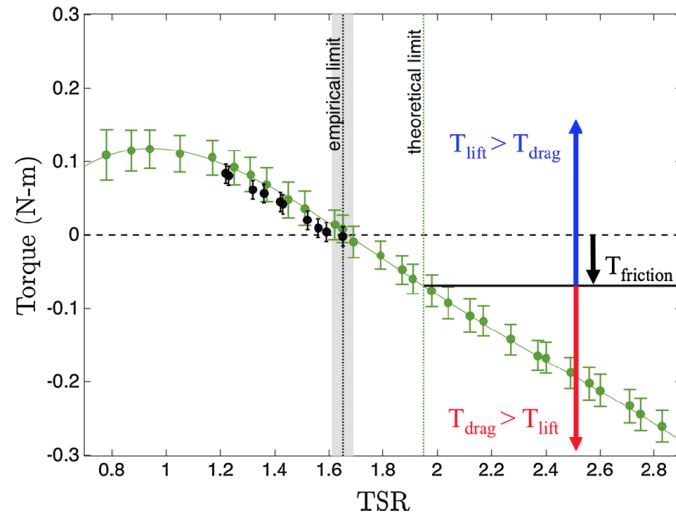
Figure 4.5: Measured torque for flow-driven (black) and motor-driven (green) cases. Error bars represent an estimate of one standard deviation in measurement error. A fourth-order polynomial is fit to the motor-driven points. Figure reproduced from Araya and Dabiri (2015).
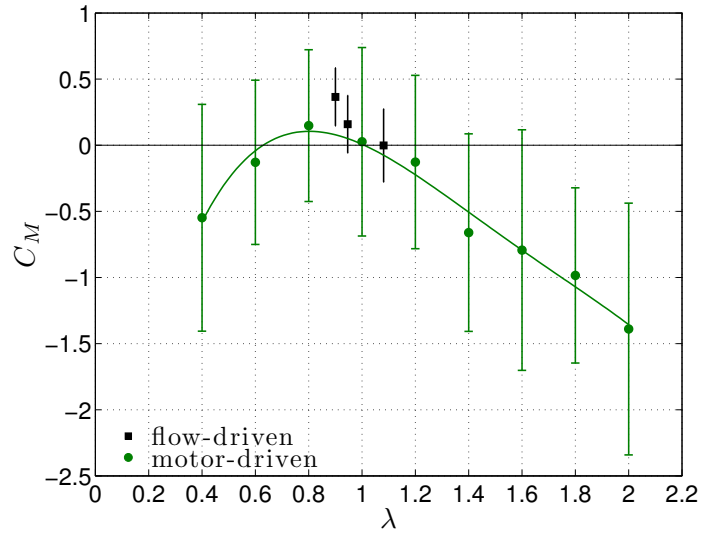
Figure 4.6: Moment coefficients for flow-driven (black) and motor-driven (green) cases. Error bars represent one standard deviation. A fourth-order polynomial is fit to the motor-driven points.

Figure 4.5, reproduced from Araya and Dabiri (2015), presents turbine shaft torque measurements for a fixed $Re = 2.6 \times 10^4$ and λ ranging from approximately 0.9-2.8. There is qualitative agreement in the trend of the measured torque for similar flow-driven and motor-driven cases. Figure 4.5 also points out the theoretical limit of tip-speed ratio below which the difference between flow-driven and motor-driven wakes is minimal (Araya and Dabiri, 2015). Similarly, in figure 4.6, we show the moment coefficients of flow-driven cases with $F = 0$, 0.1, and 0.2 and motor-driven cases for λ ranging from 0.4-2.0 at $Re = 2000$. The flow-driven and motor-driven moment coefficients in the computation have good agreement between each other and similar behaviors to the torque for flow-driven and motor-driven VAWT measured in the experiments. These suggest that our load model is sufficient to represent the load of a flow-driven VAWT and a motor-driven VAWT can reproduce the physics of a flow-driven VAWT at $Re = 2000$ when λ is ranging from 0.4-2.0.

4.4 Analysis on the starting torque of a three-bladed VAWT

The starting torque of a VAWT with various initial orientations are hard to compare directly due to their different rates of rotational acceleration. Therefore, we propose a simple model to analyze the starting torque. Consider the limit where the inertia of the VAWT is much larger than the inertia of the fluid so that the VAWT is barely rotating during starting. We can then treat the starting torque as the torque acting on a VAWT fixed in the flow.
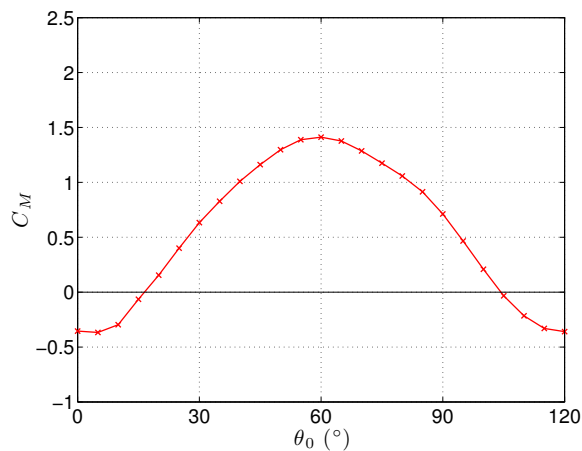
Figure 4.7: Torque distribution of a three-bladed VAWT at $t^* = 1$ and $Re = 2000$.

We first simulate the flow past a three-bladed VAWT fixed at every five degrees. The flows start impulsively and the early torque distribution at $t^* = 1$, which has not been affected by vorticity-blade interaction, is shown in the red curve in figure 4.7. Only the torques between $0°$ and $120°$ are shown because of the symmetry. The maximum of averaged torque occurs around $\theta_0 = 60°$, which explains why $\theta_0 = 60°$ is a favorable orientation to start a three-bladed VAWT. Two equilibria where the torque is equal to zero are found at $\theta_0 = 15°$ and $\theta_0 = 105°$. The equilibrium at $\theta_0 = 105°$ is stable because the curve has a negative slope. As the VAWT slowly rotates away from $\theta_0 = 105°$, the torque becomes stronger and pulls the VAWT back to the stable equilibrium. With similar arguments, equilibrium at $\theta_0 = 15°$ is unstable, i.e., as the VAWT slowly rotates away from $\theta_0 = 15°$, the increasing torque pushes the VAWT further away. Therefore, as shown in figure 4.3(b), VAWT that are not able to self-start oscillate around $\theta_0 = 105°$.

Shown in figure 4.8, we investigate the contributions of the torque from each blade to the starting torque for a three-bladed VAWT. For example, when VAWT is at $\theta_0 = 30°$, its three blades are at $\theta_0 = 30°$, $\theta_0 = 150°$, and $\theta_0 = 270°$. We plot the torque from each blade at the corresponding azimuthal angle in figure 4.7. These torque distributions of the blades are compared with the starting torque of a single-bladed VAWT. We can see that the torque distribution from each blade is close to that of a single-bladed VAWT except for a small difference in the downwind region $(180° \leq \theta_0 \leq 360°)$.
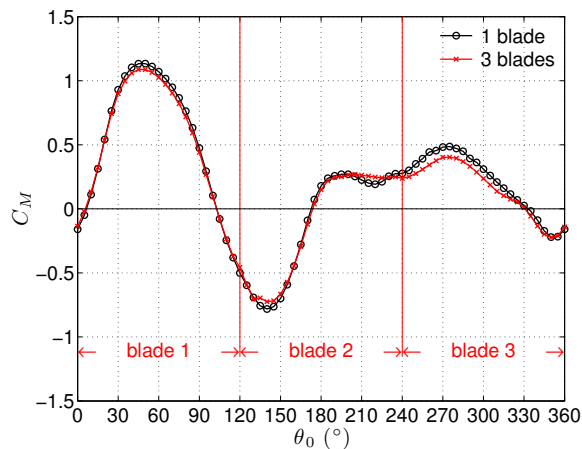
Figure 4.8: The contributions of the torque from each blade for a three-bladed VAWT at $t^* = 1$ at $Re = 2000$.

Due to the similarity of the torque distribution from each blade, the starting torque of a three-bladed VAWT can be well-reconstructed from the single-bladed torque distribution. The starting torque at a certain orientation is reconstructed by linearly combining the torques at the respective position of the blades. For instance, the torque of a three-bladed VAWT at $\theta_0 = 30°$ can be reconstructed by adding the single-bladed torques at $\theta_0 = 30°$, $\theta_0 = 150°$, and $\theta_0 = 270°$. Figure 4.9 shows the starting torque in figure 4.7 again (red curve) and the reconstruction of the torque distribution from the single-bladed torque distribution obtained from figure 4.8 (black curve). We can see that the reconstruction retains all important features of the three-bladed starting torque. The largest difference occurs at where the VAWT generates largest torque ($\theta_0 = 60°$).
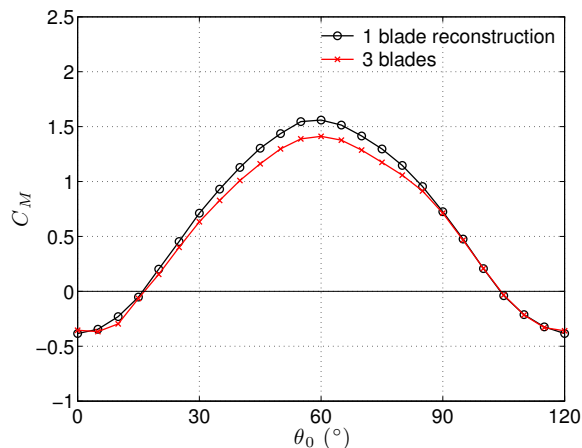
Figure 4.9: Comparison of the starting torque of a three-bladed VAWT (red curve) and the three-bladed torque reconstruction from the single-bladed result (black curve) at $t^* = 1$ and $Re = 2000$.

4.5   The starting torque distribution of a multi-bladed VAWT

In order to investigate the effect of solidity on the starting torque, as discussed in section 4.4, we investigate the torque of a multi-bladed VAWT fixed in the flow at various initial orientations. Again, we simulate the flow past a multi-bladed VAWT fixed at every five degrees. Figure 4.10 shows the starting torques of VAWT with two to eight blades at $t^* = 1$ and $Re = 2000$.

The torques of the multi-bladed VAWT with N_b blades are shown only between $0°$ and $\left(\frac{360}{N_b}\right)^°$ due to the symmetry. The range of initial orientations that generate a positive torque increase as the
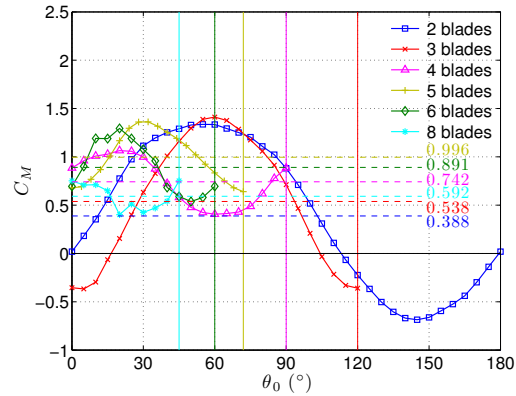
Figure 4.10: The starting torque distributions with $\sigma \approx 0.106$ (1 blade), 0.212 (2 blades), 0.318 (3 blades), 0.424 (4 blades), 0.637 (6 blades), and 0.848 (8 blades) at $t^* = 1$ at $Re = 2000$.

number of the blades increases. VAWT with more than three blades generate positive torque at all initial orientations. Moreover, we can again observe that stable equilibria for two and three-bladed VAWT exist around $\theta_0 = 115°$ and $105°$, respectively. Two, three, four, five, six, and eight-bladed VAWT generate the highest torques around $\theta_0 = 55°$, $60°$, $20°$, $30°$, $20°$, and $0°$, respectively, which indicate the optimal orientations for starting.

Similarly, we also investigate the contributions of the torque from each blade to the starting torque for multi-bladed VAWT as discussed in section 4.4. These torque distributions of the blades are compared with the starting torque of a single-bladed VAWT in figure 4.11. When the solidity is lower than 0.5, the torque distribution from each blade is close to one of a single-bladed VAWT except for a small difference in the downwind region ($180° \leq \theta_0 \leq 360°$), highlighting the lack of vorticity-blade interactions amongst the different blades at early times. The average value of the torques over a cycle labelled in figure 4.10 increases as the number of the blades increases. However, when the solidity is larger than 0.5, the torque distribution from each blade is different from one of a single-bladed VAWT. As the number of the blades increases, the discrepancy in the torque distribution increases and the average value of the torques over a cycle may decreases.
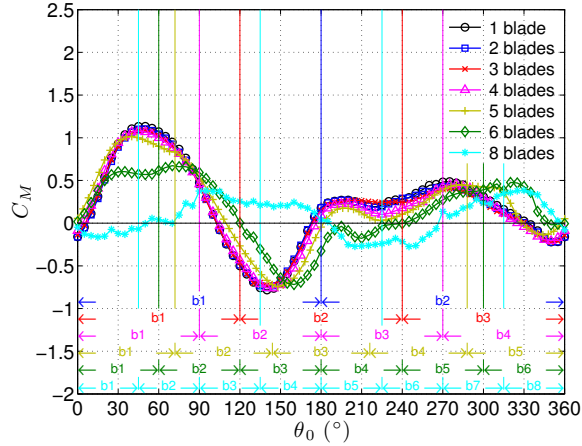
Figure 4.11: The contributions of the torque from each blade with $\sigma \approx 0.106$ (1 blade), 0.212 (2 blades), 0.318 (3 blades), 0.424 (4 blades), 0.637 (6 blades), and 0.848 (8 blades) at $t^* = 1$ at $Re = 2000$.

4.6 Effect of the static pitch angle on the single-bladed torque distribution

We showed in sections 4.4 and 4.5 that the multi-bladed starting torque can be well reconstructed from the single-bladed torque distribution when the solidity is lower than 0.5. Here we investigate the extent to which the static pitch angle can be changed to optimize the starting torque. As illustrated in figure 4.12, a constant static pitch angle is applied to the blade and the torque distribution changes correspondingly. The constant static pitch angle, ψ, is zero in the tangential direction, and positive when the blade is rotated counter-clockwise to the turbine's center.
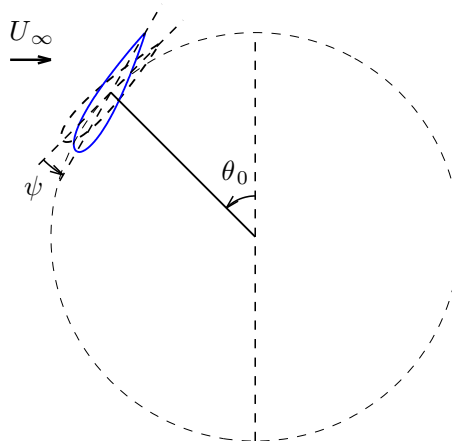
Figure 4.12: Schematic of a single-bladed VAWT with a static pitch angle fixed in the flow.

Figure 4.13(a) shows the single-bladed torque distributions with various constant static pitch angles at $t^* = 1$ and $Re = 2000$. The black dashed curve is the single-bladed torque distribution with zero pitch angle. The red and blue curves correspond to positive and negative pitch angles, respectively. We can see that at any initial azimuthal angle, there exists an optimal static pitch angle that generates the highest torque. The torque distribution corresponding to these highest (optimal) torques is the upper envelope of these curves and is shown as the green curve in figure 4.13(a). The corresponding optimal static pitch angles are shown in figure 4.13(b).
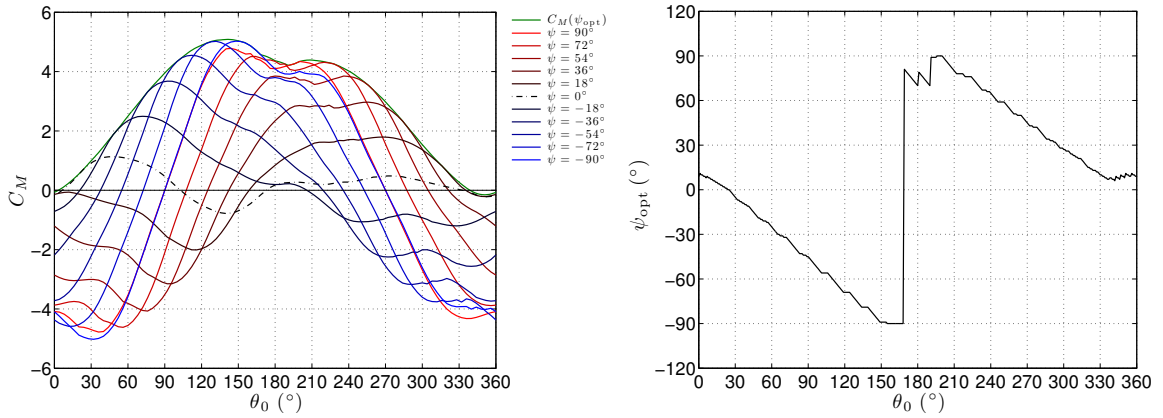
(a) Torque distributions with various static pitch angles (blue, black, and red curves) and the optimal torque distribution (green curve) at $t^* = 1$ and $Re = 2000$.

(b) The optimal static pitch angles.

Figure 4.13: Torque distributions with various static pitch angles at $t^* = 1$ and $Re = 2000$ and the corresponding optimal static pitch angle.

(a) Reconstructing the optimal three-bladed torque distribution from single-bladed results.

(b) Three-bladed torque distribution reconstructed by optimal single-bladed torque distribution.
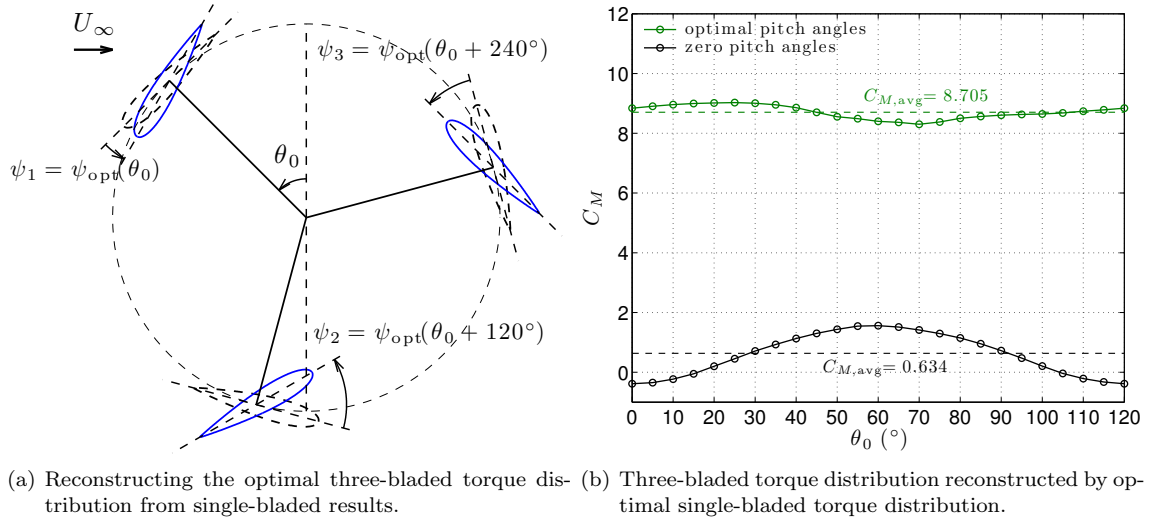
Figure 4.14: The schematic of a three-bladed VAWT with static pitch angles and the corresponding reconstruction of the three-bladed torque distribution.

The optimal starting configuration for a multi-bladed VAWT can be determined by pitching the blades with their own optimal static pitch angles as illustrated in figure 4.14(a). For example, when a three-bladed VAWT is at $\theta = 0$, its three blades are at $\theta = 0°$, $120°$, and $240°$. The corresponding optimal static pitch angles found from figure 4.13(b) are $9°$, $-69°$, and $65°$. We then pitch the blades with their own optimal static pitch angles. The optimal three-bladed torque distribution can be reconstructed by linearly adding the torques at those azimuthal angles with their own optimal static pitch angles from figure 4.13(a). The resulting torque distribution is shown in the green curve in figure 4.14(b) and compared with the three-bladed torque distribution reconstructed from the single-bladed, zero pitch angles result. We can see that the three-bladed torques with optimal static pitch angles are positive and much higher than with zero pitch angles at all orientations.

4.7 Summary

The starting capability of a VAWT was numerically investigated by simulating the flow around a free-to-rotate three-bladed VAWT. The predictor-corrector method was used to couple the motion of the VAWT with the aerodynamic forces exerted on the blade and shaft torque generated by a load. A simple load model, which is linearly proportional to turbine angular velocity, is used. Tip-speed

ratio, which is associated with the angular velocity of the VAWT, is characterized as a function of Reynolds number and density ratio. Simulations show that there exists a critical Reynolds number below which the VAWT cannot start itself. Flow at a higher Reynolds number drives the VAWT to rotate faster. At the same Reynolds number, VAWT with a density ratio lower than the critical value is capable of self-starting. A smaller density ratio results in a shorter time needed for VAWT to reach the stationary state but a larger fluctuation in angular velocity due to a smaller moment of inertia. Moreover, the averaged properties of the stationary state depend mainly on the Reynolds number but not on the density ratio.

The power outputs and the moment coefficients of motor-driven and flow-driven VAWT were compared. The flow-driven power coefficients lie within the power fluctuations of a motor-driven turbine at various tip-speed ratios. With a larger friction coefficient, the VAWT generates a higher averaged power output but operates at a lower averaged tip-speed ratio until the friction coefficient is too large for a VAWT to rotate at Reynolds number examined. Moreover, the flow-driven and motor-driven moment coefficients in the computation have good agreement between each other and similar trend of the torque for flow-driven and motor-driven VAWT measured in the experiments performed by collaborators Araya and Dabiri (2015). These suggest that the load of a flow-driven VAWT can be well-represented by the proposed simple load model and within the range of tip-speed ratio examined, a motor-driven VAWT can reproduce the physics of a flow-driven VAWT at a low Reynolds number $Re = 2000$.

A simple model was proposed in order to analyze the starting torque of VAWT. The inertia of the blade is assumed to be much larger than the fluid, i.e., $\phi_\rho \gg 1$, so that the VAWT barely rotates and can be considered fixed in the flow. Analysis of the starting torque at early time indicates the two important orientations associated with the starting of a VAWT: orientation corresponding to the largest torque generation, at which a self-starting turbine always starts, and a stable equilibrium, where a non-self-starting turbine oscillates. These features agree with the observations from the simulations of the starting of a VAWT.

The effect of turbine solidity on the starting torque and the contribution to the starting torque

from each blade for a multi-bladed VAWT were investigated. When solidity is smaller than 0.5, the averaged starting torque over a cycle increases with solidity due to a growing range in generating positive starting torque and the multi-bladed torque distribution from each blade is close to the single-bladed one. Therefore, the total torque distribution reconstructed from the single-bladed torque distribution retains important features. On the other hand, when solidity is above 0.5, the discrepancy between single and multi-bladed blade torque distributions grows and the averaged total torque over a cycle decreases as solidity increases.

Therefore, for a sufficiently low turbine solidity of about 0.5, the starting torque distribution can be modeled by considering a single blade at different orientations and constructed for multi-bladed turbines by linearly combining the torques at the respective positions of the blades. The torque distributions of the single-bladed VAWT with various static pitch angles were then investigated. An optimal pitch distribution was determined by the pitch angles that maximize the torque generation at individual orientation. Using this model, we found an optimal starting configuration for a multi-bladed low-solidity VAWT.

Chapter 5

Optimal control of time-dependent blade pitch on a VAWT

In this chapter, we apply optimal control to determine the time-dependent blade pitching angle that minimizes the input power required to drive a single-bladed VAWT. The influence of the cost function and the horizon length are studied. The controlled and uncontrolled flows are compared to draw preliminary conclusions regarding the fluid-mechanical mechanisms behind the input power reduction.

5.1   Simulation setup

In this chapter, we are interested in determining how the blades of a VAWT could be pitched in order to maximize power generation using optimal control. As a preliminary step in this direction, optimal control of time-dependent blade pitch on a single-bladed VAWT is investigated at low Reynolds number in order to obtain a solution in a relative short computational time. Because of the similarity in motor-driven and flow-driven cases as discussed in section 4.3, we propose a relevant model problem in order to further reduce computational time by considering minimizing the input power required to rotate a VAWT at a constant tip-speed ratio. Figure 5.1 shows the schematic of a single-bladed motor-driven VAWT with a control of time-dependent blade pitch. The VAWT has a radius, R, and rotates with an angular velocity, Ω, in a freestream with velocity, U_∞. The blade has a chord length, c, and pitches about its center chord, where the arm of turbine usually connect

to the blade in commercial VAWT, with an angular velocity, $\dot{\psi}$. The azimuthal and pitch angles are θ and ψ, respectively.
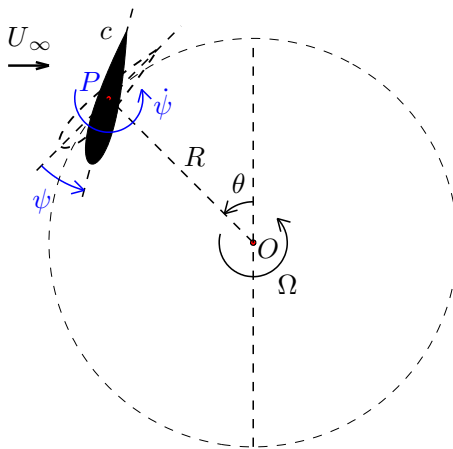
Figure 5.1: Schematic of a single-bladed motor-driven VAWT with a control of time-dependent blade pitch.

Again, IBPM is used to compute two-dimensional incompressible flows around the VAWT in a non-inertial airfoil-fixed frame at a low Reynolds number, $Re = 500$. In this case, we have two rotation centers: one is the turbine rotation center and the other is the blade center chord. Therefore, we use the extension of the non-inertial incompressible Navier-Stokes equations to two successively rotating frames. The detailed derivation is given in Appendix A. θ, Ω, ψ, and $\dot{\psi}$ correspond to θ_1, Ω_1, θ_2, and Ω_2 in section 2.4 and Appendix A, respectively. In all simulations, we use 6 nested grids of progressively increasing size and decreasing resolution. Each grid is composed of 300×300 cells, which correspond to $\Delta x = 0.0133$, and the extend of the smallest grid is 4.0×4.0 chord lengths. A NACA0018 airfoil is used as the blade of the VAWT. The VAWT has a radius $R = 1.5\ c$ and is motor-driven at a constant tip-speed ratio $\lambda = 2$ so that the period is $T = 1.5\pi \approx 4.7124$ convective time units. CFL number is made less than 0.4.

Since the VAWT is motor-driven at a constant rotation rate in this case, the input power is equal to the negative of the power generated by the forces exerted on the blade by the fluid, i.e., $(Power)_{input} = -\Omega\ \tau_{fb}$. In this thesis, optimal control aims to minimize the integral of the input

power over a horizon of the length T_H,

$$\mathcal{J}_P = \int_0^{T_H} (Power)_{input} \ dt = \int_0^{T_H} (-\Omega \ \tau_{fb}) \ dt \ . \tag{5.1}$$

Inspired by Hwang et al. (2006), we also consider maximizing the mean tangential force, which can be achieved by minimizing the following quadratic cost function:

$$\mathcal{J}_T = \int_0^{T_H} \frac{1}{2} (F_T - F_{T,\text{ref}})^2 \ dt \ , \tag{5.2}$$

where F_T is the tangential force and $F_{T,\text{ref}}$ is its targeted value. We can see that when $F_{T,\text{ref}}$ is set to be a constant much larger than F_T, the $-F_T F_{T,\text{ref}}$ term dominates in equation 5.2. Therefore, minimizing $\mathcal{J}_T$ results in maximizing the mean tangential force when $F_{T,\text{ref}}$ is large.

A time-dependent control with single degree of freedom, $\dot{\psi}(t)$, is used to minimize the cost function. The pitch angle of the blade, $\psi(t)$, is obtained by solving the equation $\frac{d\psi}{dt}(t) = \dot{\psi}(t)$ using the second order Runge-Kutta scheme as introduced in section 2.3. The gradient of the cost with respect to the control is determined by solving the corresponding adjoint equations and the controls is updated in the *direction* provided by the control gradient in order to locally and optimally reduce the cost function. An optimal control is obtained iteratively with the procedures discussed in section 2.5.

Based on the studies of Joe et al. (2010) and Flinois and Colonius (2015), we use the *receding-horizon* predictive control in order to obtain optimization results that are longer than one horizon. An overlap of 2/3 of the optimal control is used to ensure that transients from adjoint simulation do not affect the retained solution. Therefore, the initial condition for each horizon i is chosen to be a snapshot of the converged solution of the previous horizon $i-1$ such that $t_i^*(0) \approx (2/3)T_{H_{i-1}}$. The choice of T_{H_i} is discussed in section 5.2. The first control guess is chosen to be zero pitch rate throughout each new horizon. An initial discontinuity in the optimal control is expected since $\dot{\psi}((2/3)T_{H_{i-1}}) \neq 0$ in general.

5.2   Optimization results

All optimizations start from the same initial condition of a flow with $\psi = 0°$ and $\theta = -90°$. The baseline case refers to the uncontrolled flow, which corresponds to the flow with $\psi = 0°$ and $\dot{\psi} = 0$ over the horizon. $\theta = -90°$ is chosen so that when performing the receding-horizon predictive control, $\theta = 90° - 270°$ in each rotation, where the aforementioned wake-capturing phenomenon occurs, is not included in the overlap of horizons. In order to investigate the influence of changing the cost function and the horizon length, several optimizations are run and summarized in table 5.1. The performance of the optimizations is quantified by the amount of mean input power reduction, ΔC_P, and mean tangential force increment, ΔC_T, obtained towards the end of the optimized simulations. Control cost is evaluated by the term $\int_0^{T_H} \frac{1}{2}|\dot{\psi}|^2 \, dt$.

Table 5.1: Summary of results from the optimizations. T_H is the control horizon. T_o is the correspond overlaps in control horizon between each optimization. ΔC_P and ΔC_T are the reduction in mean input power and the increment in mean tangential force relative to the unforced case, respectively. $\int_0^{T_H} \frac{1}{2}|\dot{\psi}|^2 \, dt$ is used to evaluate the control cost.

| Run	T_H	T_o	cost function	ΔC_P (%)	ΔC_T (%)	$\int_0^{T_H} \frac{1}{2}|\dot{\psi}|^2 \, dt$
1	$1 \times 1T$	0	$\mathcal{J}_P$	7.60	2.23	0.0007
2	$1 \times 1.5T$	0	$\mathcal{J}_P$	22.46	13.97	0.0021
3	$1 \times 2T$	0	$\mathcal{J}_P$	22.04	17.55	0.0024
4	$1 \times 3T$	0	$\mathcal{J}_P$	21.64	18.18	0.0030
5	$1 \times 4T$	0	$\mathcal{J}_P$	11.60	12.70	0.0048
6	$2.5T \, (2 \times 1.5T)$	$1 \times 0.5T$	$\mathcal{J}_P$	23.10	14.30	0.0028
7	$3.5T \, (3 \times 1.5T)$	$2 \times 0.5T$	$\mathcal{J}_P$	18.14	9.12	0.0047
8	$4.5T \, (4 \times 1.5T)$	$3 \times 0.5T$	$\mathcal{J}_P$	6.20	-1.04	0.0047
9	$5.5T \, (5 \times 1.5T)$	$4 \times 0.5T$	$\mathcal{J}_P$	5.42	-3.17	0.0049
10	$1 \times 1.5T$	0	$\mathcal{J}_T$	40.95	55.77	0.0502
11	$2.5T \, (2 \times 1.5T)$	$1 \times 0.5T$	$\mathcal{J}_T$	33.45	59.89	0.1518
12	$3.5T \, (3 \times 1.5T)$	$2 \times 0.5T$	$\mathcal{J}_T$	20.45	44.16	0.1518
13	$4.5T \, (4 \times 1.5T)$	$3 \times 0.5T$	$\mathcal{J}_T$	7.92	31.43	0.1518
14	$5.5T \, (5 \times 1.5T)$	$4 \times 0.5T$	$\mathcal{J}_T$	4.71	25.17	0.1518

Improved results of runs 1 to 5 using $\mathcal{J}_P$ are obtained by increasing the length of the control horizon. Although the cost function that has been minimized is $\mathcal{J}_P$, the tangential force is also enhanced. Among all runs using a single horizon, run 2 with $T_H = 1.5T$ has the largest ΔC_P of about 22.5%. Moreover, finding a converged solution for the run using a single horizon with a long length ($> 4T$) is difficult. Therefore, when the control horizon is long, the improved result is obtained using the receding-horizon predictive control discussed in section 5.1. Each horizon in the receding-horizon predictive control is chosen to be $T_{H_i} = 1.5T$ and the corresponding overlap between two horizons is $T_o = \frac{2}{3}T_H = 0.5T$.

In runs 6 to 9, $\mathcal{J}_P$ is minimized using two to five $1.5T$-long horizons, which corresponds to a total horizon of a length $2.5T$ to $5.5T$. Improved results of runs 2 and 6 to 9 are compared, respectively, with that of runs 10 to 14, where $\mathcal{J}_T$ is minimized instead. ΔC_P of runs 6 and 7 agree with the trend of ΔC_P of runs 3 to 5. For a horizon longer than $4T$, the input power in runs 8 and 9 are reduced by about 5% and the control costs are roughly the same as run 5 ($T_H = 4T$). Nevertheless, when minimizing $\mathcal{J}_P$ with a long horizon, the reduction in input power does not guarantee an increase in the tangential force. From the improved results of runs 10 to 14, we can see that minimizing $\mathcal{J}_T$ can successfully enhance the averaged tangential force and reduce the input power. In all cases examined, the power reduction using $\mathcal{J}_T$ is higher than using $\mathcal{J}_P$ but with a much greater control cost (about 30 times), which may indicate that minimizing $\mathcal{J}_P$ only converges to a local minimum.

5.3 Influence of the cost function

We now focus on runs 9 and 14, which correspond to the improved results obtained using $\mathcal{J}_P$ and $\mathcal{J}_T$ over a horizon of a length $5.5T$, respectively. The histories of blade pitch angle, input power, and tangential force for both runs are shown in figure 5.2 and compared with the uncontrolled flow (baseline case). From figure 5.2(a), optimal blade pitch angles about $5°$ and $-6°$ are found by the end of the control horizon in run 9 and run 14, respectively. We can also see that the control cost of run 14 is larger than run 9 because of the larger pitching motion in the first $1.5T$ of the horizon. As shown in figures 5.2(b) and 5.2(c), the largest input power reduction and tangential force increment

in both cases are between 90° and 180° in most of the cycles. Between 0° and 90° in each cycle, both the power generation and the tangential force are damaged by the optimal blade pitch in run 9, but enhanced in run 14. However, between 180° and 360° in each cycle, both the power generation and the tangential force are enhanced by the optimal blade pitch in run 9, but damaged in run 14.
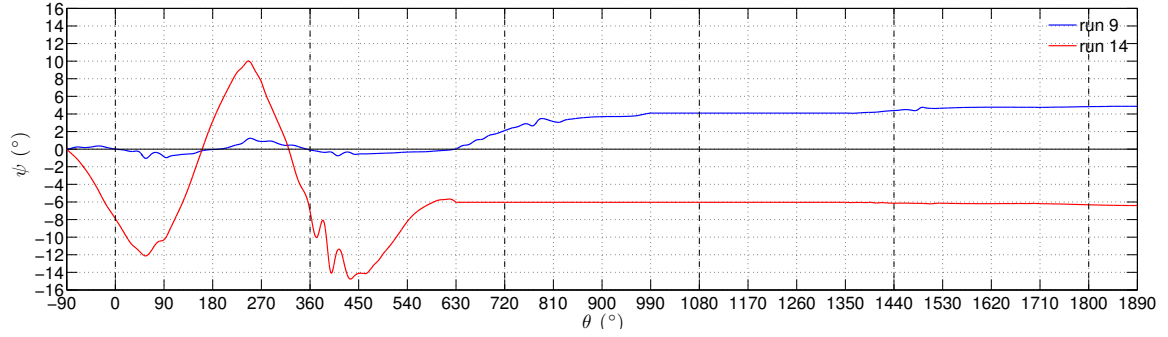
(a) Blade pitch angle history
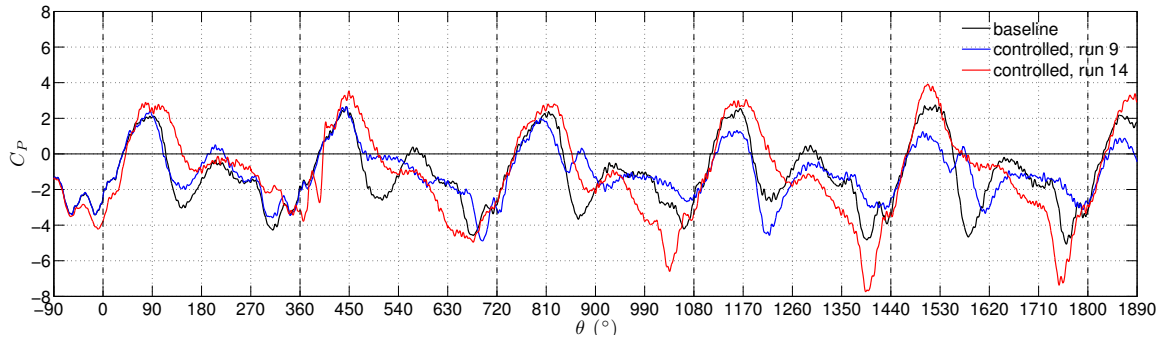
(b) Power coefficient history
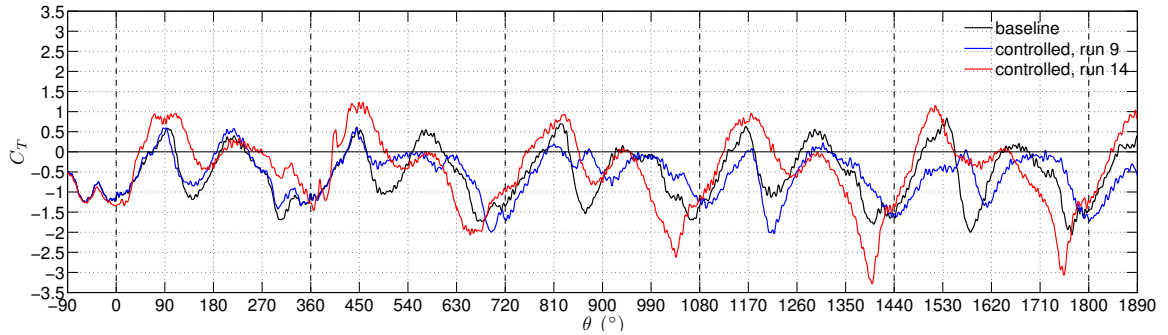
(c) Tangential force coefficient history

Figure 5.2: Histories of (a) blade pitch angle, (b) input power, and (c) tangential force of baseline case (black curve), run 9 (blue curve), and run 14 (red curve).

5.4 Comparison of the controlled and uncontrolled flows

Figures 5.3, 5.4, and 5.5 show the comparison of the controlled and uncontrolled flows between $\theta = 1440° - 1530°$, $1560° - 1650°$, and $1680° - 1770°$, respectively. In each figure, the power coefficient histories are plotted again in subfigure (a) and the vorticity fields are compared in subfigures (b-e) with the corresponding phases labelled in subfigure (a).

From figure 5.3, we can see that when θ is between $1440°$ and $1560°$, the angle of attack is increasing. Run 14 generates a larger power output by pitching counter-clockwise so that the effective angle of attack is lowered, which avoids a larger flow separation. Similarly, when θ is sbetween $1680°$ and $1800°$ (figure 5.5), run 9 has a lower power input than the unforced flow due to a lower effective angle of attack.

When $\theta = 1590° - 1650°$ (figure 5.4), the wake-capturing of a vortex pair is observed in the baseline case. By $\theta = 1590°$ (figure 5.4 (c)), the blade in run 9 eliminates the TEV and the corresponding power coefficient increases. However, a new TEV is formed and cuts off the LEV from the leading edge shear layer by $\theta = 1620°$ (figure 5.4 (d)). This new TEV and the leading edge shear layer form a jet impinging the blade surface (figure 5.4 (e)), which results in a drop in power coefficient. On the other hand, in run 14 the wake-capturing vortex pair still travels with the blade. However, the blade pitches in a way such that the LEV always travels behind the TEV. Although there exits a jet formed by the vortex pair impinging the blade at the trailing edge, the LEV and the leading edge shear layer forms a wide range of low pressure region on the blade surface, which causes a large input power reduction.

(a) Power coefficient history

(b) $\theta = 1440°(0°)$, $\alpha = 0°$.

(c) $\theta = 1470°(30°)$, $\alpha = 9.9°$.

(d) $\theta = 1500°(60°)$, $\alpha = 19.1°$.

(e) $\theta = 1530°(90°)$, $\alpha = 26.6°$.

Figure 5.3: Power coefficient history (a) and vorticity field for baseline, run 9 and run 14 at $\theta = 1440°$ (b), 1470° (c), 1500° (d), and 1530° (e). Negative and positive vorticity are plotted in blue and red contour levels, respectively.

(a) Power coefficient history

(b) $\theta = 1560°(120°)$, $\alpha = 30°$.

(c) $\theta = 1590°(150°)$, $\alpha = 23.8°$.

(d) $\theta = 1620°(180°)$, $\alpha = 0°$.

(e) $\theta = 1650°(210°)$, $\alpha = -23.8°$.

Figure 5.4: Power coefficient history (a) and vorticity field for baseline, run 9 and run 14 at $\theta = 1560°$ (b), 1590° (c), 1620° (d), and 1650° (e). Negative and positive vorticity are plotted in blue and red contour levels, respectively.

(a) Power coefficient history

(b) $\theta = 1680°(240°)$, $\alpha = -30°$.

(c) $\theta = 1710°(270°)$, $\alpha = -26.6°$.

(d) $\theta = 1740°(300°)$, $\alpha = -19.1°$.

(e) $\theta = 1770°(330°)$, $\alpha = -9.9°$.
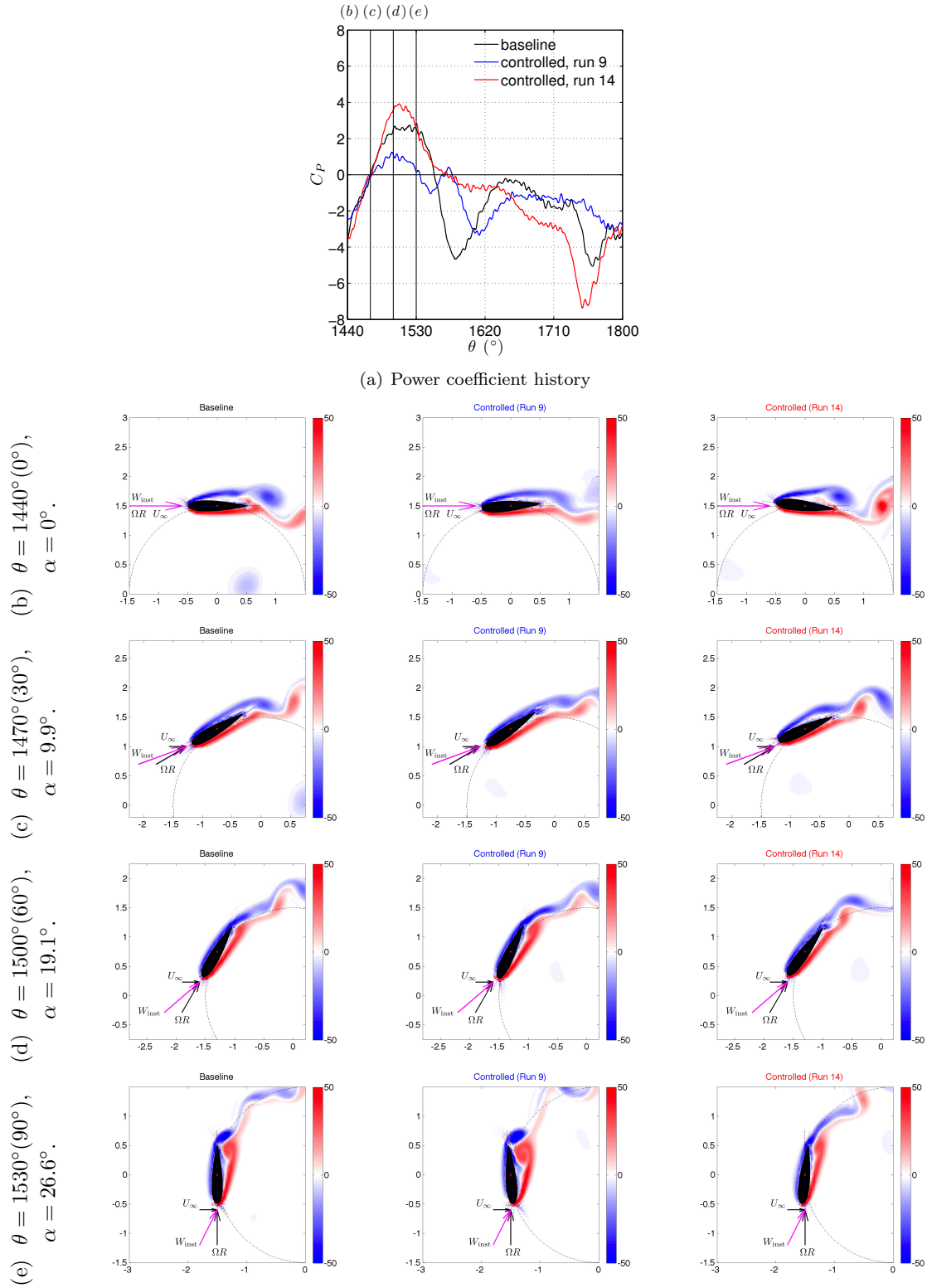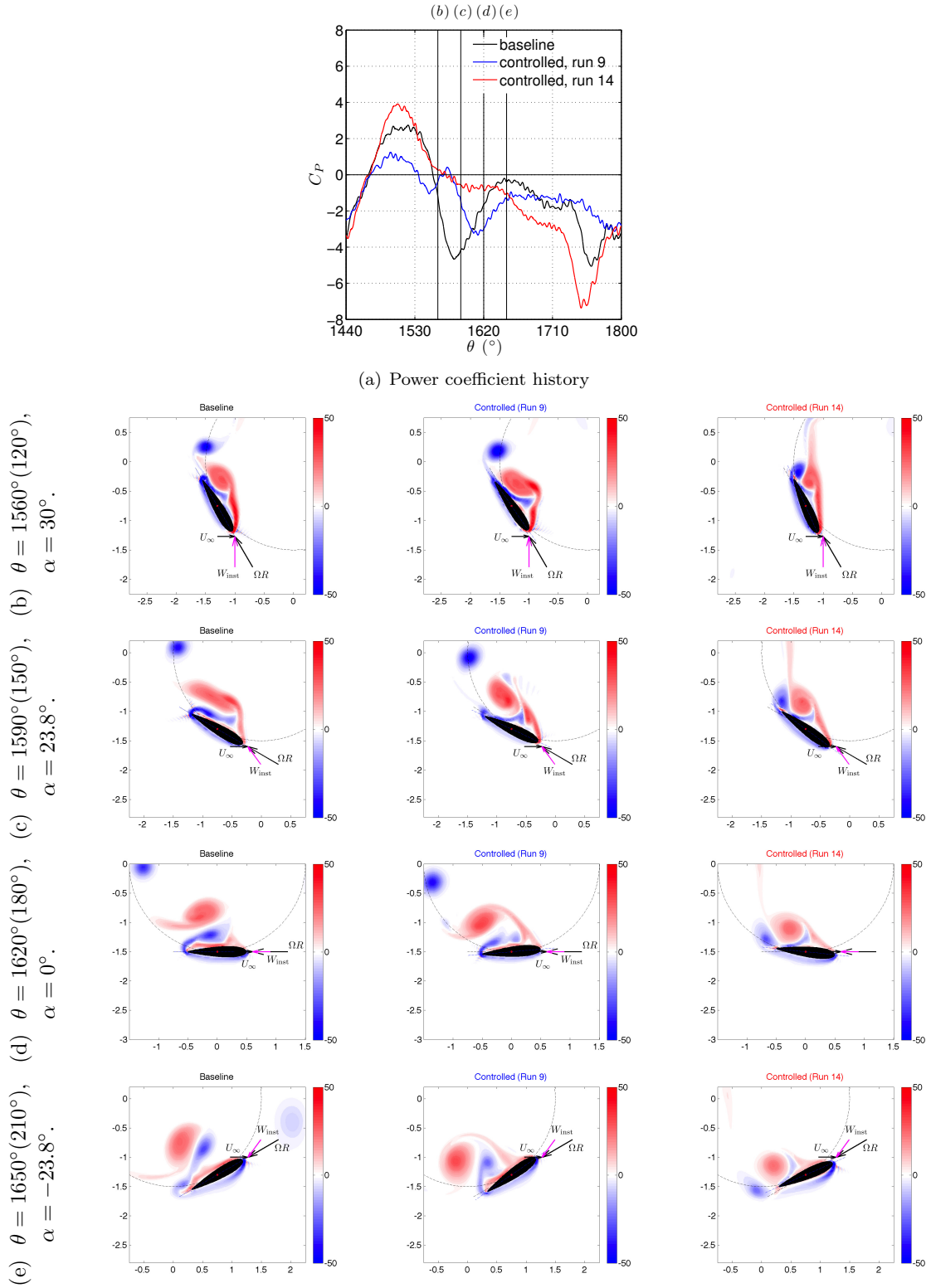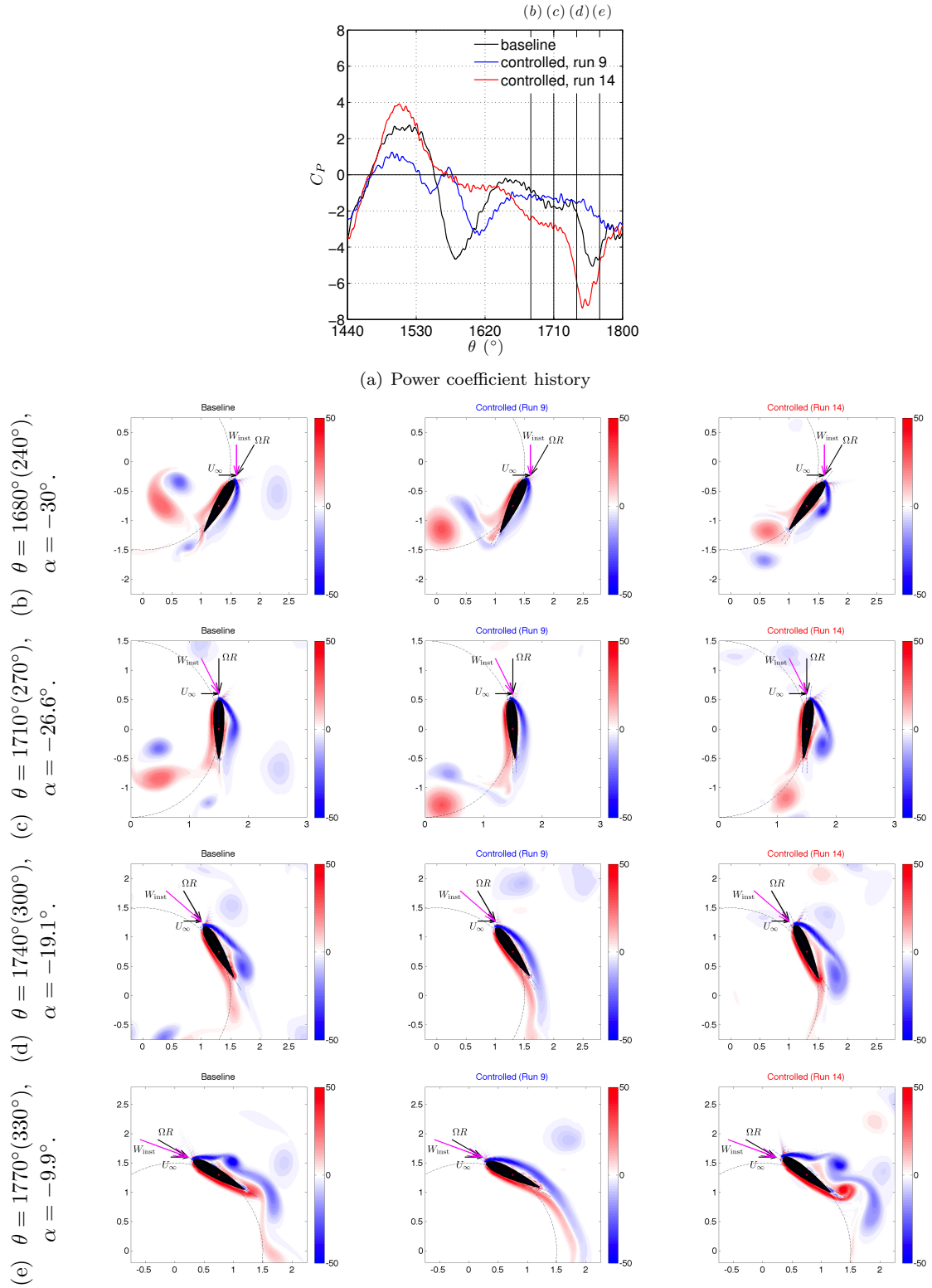
Figure 5.5: Power coefficient history (a) and vorticity field for baseline, run 9 and run 14 at $\theta = 1680°$ (b), 1710° (c), 1740° (d), and 1770° (e). Negative and positive vorticity are plotted in blue and red contour levels, respectively.

5.5   Summary

In this chapter, a preliminary study was made to determine an optimal blade pitch as a function of time for a single-bladed VAWT. With fixed tip-speed ratio, the input power and mean tangential force were minimized over a specific time horizon by applying optimal control theory. The input power was reduced by about 10-20% with a single horizon shorter than four periods. With a horizon longer than four periods, the optimal control was obtained by the receding horizon predictive control, which leads to a input power reduction of about 6% by the end of the longest control horizon examined. When the input power is used as a cost function, the solution seems to converge to only a local minimum because the reduction in the input power is less than that using the mean tangential force as a cost function. Moreover, although maximizing the averaged tangential force always leads to a reduction in input power, minimizing the input power does not guarantee an increase in the tangential force.

By the end of the longest control horizon examined, time-invariant pitch angles of about $5°$ and $-6°$ were obtained when the input power and mean tangential force were used as the cost functions, respectively. The comparison of the uncontrolled and controlled flows showed that when the angle of attack is increasing/decreasing in the upwind/downwind half of a cycle, the negative/positive blade pitch angle reduces input power by lowering the effective angle of attack. When the angle of attack is decreasing in the upwind half of a cycle, the wake-capturing phenomenon occurs in the uncontrolled flow. The control with positive time-invariant pitch angle successfully reduces the input power by eliminating the TEV of the wake-capturing vortex pair. However, a newly formed TEV cuts off the remaining LEV from the leading edge shear layer and forms a jet with the leading edge shear layer impinging the blade, which leads to a large decrease in power coefficient. On the other hand, the wake-capturing vortex pair still travels together with the blade when the control with negative time-invariant pitch angle is applied. Nevertheless, the TEV always travels behind the LEV with this control. Although there exits a jet formed by the vortex pair impinging the blade at the trailing edge, a wide rage of low pressure region formed by the LEV and the leading edge shear layer greatly reduces the input power.

Chapter 6

Conclusions and future works

6.1   Conclusions

In this thesis, the immersed boundary method is used to numerically investigate the flow around a two-dimensional cross section of a rotating VAWT at low Reynolds number in order to have more understanding of VAWT and explore the parametric space in relative short computational time.

First, the aerodynamics of a single-bladed VAWT is investigated. An interesting wake-capturing phenomenon that leads to a substantial decrease in lift coefficient is observed. As the VAWT rotates faster, this features is on one hand strengthened due to the intensifying Coriolis force and on the other hand attenuated because of the decreasing amplitude of the angle of attack variation. Further investigation on motion decomposition shows that the wake-capturing is associated with a unique combination of angle of attack variation, instantaneous velocity variation, and the Coriolis effect. Moreover, the qualitative agreement with the experiment (Ferreira et al., 2007) suggests that this feature may persist in real applications. The Coriolis effect on dynamic stall in a VAWT is investigated by introducing three simplified motions: EPM, SPM, and SSPM. All simplified motions are good approximations to VAWT motion at sufficiently high tip-speed ratio. However, at low tip-speed ratio, only EPM is a good approximation in the upstroke phase where the Coriolis effect is relatively small. In the downstroke phase, EPM overestimates the average lift coefficient due to the absence of the aforementioned wake-capturing. Moreover, in order to look further into the effect of the rotating frame, the Coriolis forces, and Reynolds number, the computational results of VAWT

and EPM were compared with the experimental result of EPM from the experiments performed by collaborators Dunne and McKeon (2014, 2015a,b) in Dunne et al. (2015). The flow was shown to develop similarly prior to separation, but kinematics of vortices shed post separation were reference frame and Reynolds number dependent.

Next, we investigated the starting capability of a multi-bladed VAWT. A simple load model proportional linearly to the angular velocity is used to determine the motion of the VAWT. The angular velocity is characterized as a function of Reynolds number and density ratio. The power outputs and moment coefficients of motor-driven and flow-driven VAWT were compared. For a particular Reynolds number, as the load on the flow-driven turbine is increased, the tip speed is reduced until the turbine fails to coherently rotate. The flow-driven and motor-driven moment coefficients in the computation have good agreement between each other and similar trend of the torque for flow-driven and motor-driven VAWT measured in the experiments performed by collaborators Araya and Dabiri (2015). These suggest that the load of a flow-driven VAWT can be well-represented by the proposed simple load model and a motor-driven VAWT can reproduce the physics of a flow-driven VAWT within the range of tip-speed ratio examined. A simple model was proposed in order to analyze the starting torque. By assuming that the inertia of the blade is much larger than the fluid, the VAWT can be considered stationary in the flow. The starting torque distribution of a multi-bladed VAWT indicates the important orientations corresponding to maximum torque generation, at which a self-starting turbine always starts, and a stable equilibrium, where a non-self-starting turbine oscillates. These features agree with the observations from the simulations of the starting of a VAWT. We modeled the starting torque distribution by considering a single blade at different orientations, and construct starting torque distributions for multi-bladed turbines by linearly combining the torques at the respective positions of the blades. We showed that this approximation is valid for a sufficiently low turbine solidity of about 0.5. Using this model, we found an optimal starting configuration for a multi-bladed low-solidity VAWT.

Finally, a preliminary study was made to determine an optimal blade pitch as a function of time for a single-bladed VAWT. With fixed tip-speed ratio, the input power was minimized and the mean

tangential force was maximized over a specific time horizon by applying optimal control theory. The receding horizon predictive control was used to obtain an optimal control over a horizon longer than four periods. Both cases lead to a reduction in the input power but not necessarily an enhancement in the mean tangential force. When the input power is minimized directly, the solution seems to converge to only a local minimum due to a lower input power reduction than maximizing the mean tangential force. By the end of the longest control horizon examined, two controls end up with time-invariant pitch angles of about the same magnitude but with the opposite signs. When the angle of attack is increasing/decreasing in the upwind/downwind half of a cycle, the negative/positive blade pitch angle reduces input power by lowering the effective angle of attack. When the angle of attack is decreasing in the upwind half of a cycle, the wake-capturing phenomenon occurs in the uncontrolled flow. Depending on the sign of the time-invariant pitch angle, both controls reduce the input power initially by either eliminating the TEV entirely or stalling the TEV behind the LEV. The leading edge shear layer later forms either a high pressure region on the blade with the newly formed TEV, which leads to a decrease in the power coefficient, or a low pressure region on the blade with the LEV, which greatly reduces the input power.

6.2   Future works

This thesis provides the basic understanding of the aerodynamics and the starting of a VAWT and a preliminary study of implementing optimal control on blade pitch angles to enhance turbine efficiency. However, there are still many interesting topics that have not been investigated. We comment on the possible continuation of the research presented in this thesis.

First, the interaction of multiple blades in VAWT could be investigated systematically. Although, blades do not generate much power in the downwind half of a cycle due to a low incoming velocity (Ferreira et al., 2006), the interaction between shed vortices and downwind blades could induce fluctuating loading on the turbine structure. In order to design a robust VAWT, it is essential to understand this blade-vorticity interaction.

Flow around two-counter-rotating VAWT could also be investigated. Shown by Dabiri (2011)

and Kinzel et al. (2012), two-counter-rotating VAWT have potentially higher power output per unit land area and a shorter velocity recovery distance than individual VAWT. It would be interesting to understand the mechanism of this enhancement in power output density in order to design a VAWT wind farm.

Moreover, the starting capability of VAWT could also improved by applying optimal control on blade pitch angle. In this thesis, we have shown in Chapter 4 that the highest starting torque can be generated by pitching blades with their own optimal pitch angles. It would be interesting to apply optimal control to generate the largest torque over the full starting process.

Finally, investigation on implementing optimal control to reduce the input power of a single-bladed motor-driven VAWT could be further extended to a multi-bladed motor-driven VAWT in order to taking account the effect of multiple-blades.

Appendix A

Extension of the alternative form of non-inertial Navier-Stokes equations to two successively rotating frames

Based on the derivation in section 2.1, we can easily extend the alternative form of the incompressible Navier-Stokes equations to two successively the rotating frames. Again, we consider incompressible flows external to a rigid wing (figure A.1) undergoing arbitrary motion, which is now the combination of one unsteady translation and two successive rotations. One rotation with an angular velocity $\boldsymbol{\Omega_1}(\mathbf{t})$ about a point O_1. On top of this rotating frame 1, there is the other rotation with a relative angular velocity $\boldsymbol{\Omega}_2(t)$ about a point O_2. Again, $\boldsymbol{x}_s$ are the coordinates of the points on the surface of the body. The distance between the Newtonian inertial frame and the rotating frame 1 is $\mathbf{R}_1(t)$ and the distance between the rotating frame 1 and the rotating frame 2 is $\mathbf{R}_2(t)$. The subscripts n, r_1 , and r_2 denote variables or differentiations in the Newtonian inertial frame, rotating frame 1, and the rotating frame 2, respectively.

From section 2.1, the relations of the position, velocity, vorticity, and acceleration vectors between
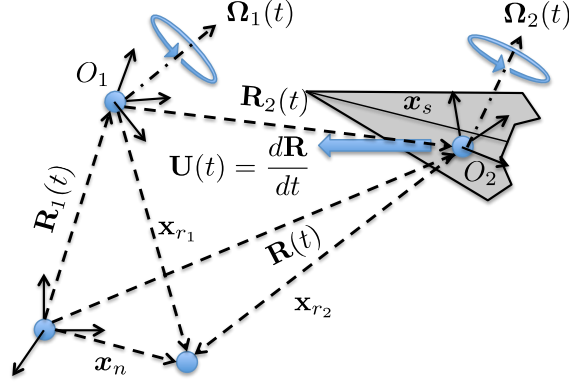
Figure A.1: Rotating coordinates for accelerating wing with two successive rotating frames.

the inertia frame and the rotating frame 1 are as follow:

$$\mathbf{x}_n = \mathbf{x}_{r_1} + \mathbf{R}_1(t) \ , \tag{A.1}$$

$$\mathbf{u}_n = \mathbf{u}_{r_1} + \boldsymbol{\Omega}_1(t) \times \mathbf{x}_{r_1} + \mathbf{U}_n(t) \ , \tag{A.2}$$

$$\boldsymbol{\omega}_n = \boldsymbol{\omega}_{r_1} + 2\boldsymbol{\Omega}_1(t) \ , \tag{A.3}$$

$$\mathbf{a}_n = \mathbf{a}_{r_1} + \left(\frac{d\boldsymbol{\Omega}_1}{dt}(t)\right)_{r_1} \times \mathbf{x}_{r_1} + 2\boldsymbol{\Omega}_1(t) \times \mathbf{u}_{r_1} + \boldsymbol{\Omega}_1(t) \times \boldsymbol{\Omega}_1(t) \times \mathbf{x}_{r_1}$$

$$+ \left(\frac{d\mathbf{U}_n}{dt}(t)\right)_{r_1} + \boldsymbol{\Omega}_1(t) \times \mathbf{U}_n(t) \ , \tag{A.4}$$

where $\mathbf{U}_n(t) = \left(\frac{d\mathbf{R}_1}{dt}(t)\right)_n$ again is the velocity of the rotating frame 1 relative to the Newtonian inertial frame.

Considering the rotations are successive, i.e., $\left(\frac{d\mathbf{R}_2}{dt}\right)_{r_1} = 0$, the relations of the position, velocity, and acceleration vectors between the rotating frame 1 and the rotating frame 2 are as follow:

$$\mathbf{x}_{r_1} = \mathbf{x}_{r_2} + \mathbf{R}_2(t) \ , \tag{A.5}$$

$$\mathbf{u}_{r_1} = \mathbf{u}_{r_2} + \boldsymbol{\Omega}_2(t) \times \mathbf{x}_{r_2} \ , \tag{A.6}$$

$$\boldsymbol{\omega}_{r_1} = \boldsymbol{\omega}_{r_2} + 2\boldsymbol{\Omega}_2(t) \ , \tag{A.7}$$

$$\mathbf{a}_{r_1} = \mathbf{a}_{r_2} + \left(\frac{d\boldsymbol{\Omega}_2}{dt}(t)\right)_{r_2} \times \mathbf{x}_{r_2} + 2\boldsymbol{\Omega}_2(t) \times \mathbf{u}_{r_2} + \boldsymbol{\Omega}_2(t) \times \boldsymbol{\Omega}_2(t) \times \mathbf{x}_{r_2} \ . \tag{A.8}$$

Moreover,

$$\left(\frac{d\mathbf{U}_n}{dt}(t)\right)_{r_1} = \left(\frac{d\mathbf{U}_n}{dt}(t)\right)_{r_2} + \mathbf{\Omega}_2(t) \times \mathbf{U}_n(t) \ . \tag{A.9}$$

From equations (A.1) to (A.9), we can obtain the relation of the position and velocity vectors in the inertial frame and the rotating frame 2 easily:

$$\mathbf{x}_n = \mathbf{x}_{r_2} + \mathbf{R}_1(t) + \mathbf{R}_2(t) \ , \tag{A.10}$$

$$\mathbf{u}_n = \mathbf{u}_{r_2} + (\mathbf{\Omega}_1(t) + \mathbf{\Omega}_2(t)) \times \mathbf{x}_{r_2} + \mathbf{\Omega}_1(t) \times \mathbf{R}_2(t) + \mathbf{U}_n(t) \tag{A.11}$$

$$\boldsymbol{\omega}_n = \boldsymbol{\omega}_{r_2} + 2\left(\mathbf{\Omega}_1(t) + \mathbf{\Omega}_2(t)\right) \ , \tag{A.12}$$

$$\mathbf{a}_n = \mathbf{a}_{r_2} + \frac{d}{dt}\left((\mathbf{\Omega}_1(t) + \mathbf{\Omega}_2(t)) \times \mathbf{x}_{r_2} + \mathbf{U}_n(t) + \mathbf{\Omega}_1(t) \times \mathbf{R}_2(t)\right)_{r_2}$$

$$+ 2\left(\mathbf{\Omega}_1(t) + \mathbf{\Omega}_2(t)\right) \times \mathbf{u}_{r_2} + (\mathbf{\Omega}_1(t) + \mathbf{\Omega}_2(t)) \times ((\mathbf{\Omega}_1(t) + \mathbf{\Omega}_2(t)) \times \mathbf{x}_{r_2})$$

$$+ (\mathbf{\Omega}_1(t) + \mathbf{\Omega}_2(t)) \times (\mathbf{U}_n(t) + \mathbf{\Omega}_1(t) \times \mathbf{R}_2(t)) \ . \tag{A.13}$$

Therefore the dimensionless Navier-Stokes equation in the rotating frame 2 becomes

$$\left(\frac{\partial \mathbf{u}_{r_2}}{\partial t}\right)_{r_2} + (\mathbf{u}_{r_2} \cdot \nabla)\mathbf{u}_{r_2} = -\nabla p + \frac{1}{Re}\nabla^2\mathbf{u}_{r_2} - \frac{d}{dt}\left((\mathbf{\Omega}_1(t) + \mathbf{\Omega}_2(t)) \times \mathbf{x}_{r_2} + \mathbf{U}_n(t) + \mathbf{\Omega}_1(t) \times \mathbf{R}_2(t)\right)_{r_2}$$

$$- 2\left(\mathbf{\Omega}_1(t) + \mathbf{\Omega}_2(t)\right) \times \mathbf{u}_{r_2} - (\mathbf{\Omega}_1(t) + \mathbf{\Omega}_2(t)) \times ((\mathbf{\Omega}_1(t) + \mathbf{\Omega}_2(t)) \times \mathbf{x}_{r_2})$$

$$- (\mathbf{\Omega}_1(t) + \mathbf{\Omega}_2(t)) \times (\mathbf{U}_n(t) + \mathbf{\Omega}_1(t) \times \mathbf{R}_2(t)) \ . \tag{A.14}$$

The boundary conditions for equation (A.14) are

$$
\begin{cases}
\mathbf{u}_{r_2} \longrightarrow -\mathbf{U}_n(t) - (\mathbf{\Omega}_1(t) + \mathbf{\Omega}_2(t)) \times \mathbf{x}_{r_2} \\
\qquad\qquad -\mathbf{\Omega}_1(t) \times \mathbf{R}_2(t) \\
\boldsymbol{\omega}_{r_2} \longrightarrow -2\left(\mathbf{\Omega}_1(t) + \mathbf{\Omega}_2(t)\right) \\
p \longrightarrow p_\infty \\
\end{cases}
\qquad \text{as } |\mathbf{x}_{r_2}| \longrightarrow \infty
$$

$$
\mathbf{u}_{r_2} = 0 \qquad\qquad\qquad\qquad \text{on the surface of the body, i.e., } \mathbf{x}_{r_2} = \mathbf{x}_s \ .
$$

$$(A.15)$$

Similarly, substituting equations (2.7), (2.8), (A.11), and (A.12) to equations (A.14) and (A.15), equation (A.14) becomes

$$
\left(\frac{\partial \mathbf{u}_n}{\partial t}\right)_{r_2} = -\nabla\Pi + (\mathbf{u}_n - \mathbf{u}_a(\mathbf{x}_{r_2}, t)) \times \boldsymbol{\omega}_n - \frac{1}{Re}\nabla \times \boldsymbol{\omega}_n \ , \tag{A.16}
$$

where $\mathbf{u}_a(\mathbf{x}_{r_2}, t)$ is again the inertial (laboratory) velocity of any given point in the rotating frame 2 given by

$$
\begin{aligned}
\mathbf{u}_a(\mathbf{x}_{r_2}, t) &= (\mathbf{\Omega}_1(t) + \mathbf{\Omega}_2(t)) \times \mathbf{x}_{r_2} + \mathbf{U}_n(t) + \mathbf{\Omega}_1(t) \times \mathbf{R}_2(t) \\
&= \mathbf{U}_n(t) + \mathbf{\Omega}_1(t) \times \mathbf{x}_{r_1} + \mathbf{\Omega}_2(t) \times \mathbf{x}_{r_2} \\
&= \mathbf{u}_U(t) + \sum_i \mathbf{u}_{\Omega_i}(\mathbf{x}_{r_i}, t) \ ,
\end{aligned}
\tag{A.17}
$$

where $\mathbf{u}_U(t) = \mathbf{U}_n(t)$ is the relative velocity due to translation, $\mathbf{u}_{\Omega_i}(\mathbf{x}_{r_i}, t) = \mathbf{\Omega}_i(t) \times \mathbf{x}_{r_i}$ is the relative velocity due to the rotation, and Π is a modified pressure given by

$$
\Pi = p + \frac{1}{2}|\mathbf{u}_n - \mathbf{u}_a(\mathbf{x}_{r_2}, t)|^2 - \frac{1}{2}|\mathbf{u}_a(\mathbf{x}_{r_2}, t)|^2 \ . \tag{A.18}
$$

The boundary conditions become

$$\begin{cases} \mathbf{u}_n \longrightarrow 0 \\[2mm] \boldsymbol{\omega}_n \longrightarrow 0 \qquad \text{as } |\mathbf{x}_{r_2}| \longrightarrow \infty \\[2mm] \Pi \longrightarrow p_\infty \end{cases} \qquad \text{(A.19)}$$

$$\mathbf{u}_n = \mathbf{u}_a(\mathbf{x}_s, t) \quad \text{on the surface of the body, i.e., } \mathbf{x}_{r_2} = \mathbf{x}_s \ .$$

We can see that equations (A.16) and (A.19) have the same form of equations (2.9) and (2.12) but with different $\mathbf{u}_a(\mathbf{x}, t)$. With an modification in $\mathbf{u}_a(\mathbf{x}, t)$, the alternative form of the non-inertial, incompressible Navier-Stokes equations can easily be extended to two successive rotating frames.

Appendix B

Derivation of the adjoint nonlinear term

In this section, detailed derivation of adjoint nonlinear term is shown. By comparing equations (2.44) and (2.50),

$$
C^T N^\dagger \left(q^\dagger, q - q_a(\mathbf{X}, \mathbf{a}), \gamma\right) = (C^T C) \left[\left(\frac{\partial N \left(q - q_a(\mathbf{X}, \mathbf{a}), \gamma\right)}{\partial \gamma} \right)^T q^\dagger \right] = (C^T C) \left[q^{\dagger^T} \left(\frac{\partial N \left(q - q_a(\mathbf{X}, \mathbf{a}), \gamma\right)}{\partial \gamma} \right) \right]
$$

$$
= (C^T C) \left[q^{\dagger^T} \left(N \left(q - q_a(\mathbf{X}, \mathbf{a}), \frac{\partial \gamma}{\partial \gamma} \right) + N \left(\frac{\partial q}{\partial \gamma}, \gamma \right) \right) \right] \ . \tag{B.1}
$$

Since $\mathbf{A} \cdot (\mathbf{B} \times \mathbf{C}) = \mathbf{C} \cdot (\mathbf{A} \times \mathbf{B}) = \mathbf{B} \cdot (\mathbf{C} \times \mathbf{A})$,

$$
C^T N^\dagger \left(q^\dagger, q - q_a(\mathbf{X}, \mathbf{a}), \gamma\right) = (C^T C) \left[\left(\frac{\partial \gamma}{\partial \gamma} \right)^T N \left(q^\dagger, q - q_a(\mathbf{X}, \mathbf{a})\right) + \left(\frac{\partial q}{\partial \gamma} \right)^T N \left(\gamma, q^\dagger\right) \right] \ . \tag{B.2}
$$

Moreover, $\frac{\partial \gamma}{\partial \gamma} = I$ and $\frac{\partial q}{\partial \gamma} = C(C^T C)^{-1}$ so that

$$
C^T N^\dagger \left(q^\dagger, q - q_a(\mathbf{X}, \mathbf{a}), \gamma\right) = (C^T C) N \left(q^\dagger, q - q_a(\mathbf{X}, \mathbf{a})\right) - C^T N \left(q^\dagger, \gamma\right) \ . \tag{B.3}
$$

Therefore,

$$
N^\dagger \left(q^\dagger, q - q_a(\mathbf{X}, \mathbf{a}), \gamma\right) \equiv C N \left(q^\dagger, q - q_a(\mathbf{X}, \mathbf{a})\right) - N \left(q^\dagger, \gamma\right) \ . \tag{B.4}
$$

Bibliography

Ahuja, S. and Rowley, C. W. (2010). Feedback control of unstable steady states of flow past a flat plate using reduced-order estimators. *Journal of Fluid Mechanics*, 645:447–478.

Alfonsi, G. (2009). Reynolds-averaged Navier-Stokes equations for turbulence modeling. *Applied Mechanics Reviews*, 62(4). 040802.

Allet, A., Hallé, S., and Paraschivoiu, I. (1999). Numerical simulation of dynamic stall around an airfoil in Darrieus motion. *Journal of Solar Energy Engineering*, 121(1):69–76.

Anderson, E. and Szewczyk, A. (1997). Effects of a splitter plate on the near wake of a circular cylinder in 2 and 3-dimensional flow configurations. *Experiments in Fluids*, 23(2):161–174.

Araya, D. B. (2016). *Aerodynamics of vertical-axis wind turbines in full-scale and laboratory-scale experiments*. PhD thesis, California Institute of Technology.

Araya, D. B., Craig, A. E., Kinzel, M., and Dabiri, J. O. (2014). Low-order modeling of wind farm aerodynamics using leaky Rankine bodies. *Journal of Renewable and Sustainable Energy*, 6(6). 063118.

Araya, D. B. and Dabiri, J. O. (2015). A comparison of wake measurements in motor-driven and flow-driven turbine experiments. *Experiments in Fluids*, 56(7):1–15.

Baker, J. (1983). Features to aid or enable self starting of fixed pitch low solidity vertical axis wind turbines. *Journal of Wind Engineering and Industrial Aerodynamics*, 15(1):369–380.

Barsky, D., Posa, A., Rahromostaqim, M., Leftwich, M. C., and Balaras, E. (2014). Experimental

and computational wake characterization of a vertical axis wind turbine. In *32nd AIAA Applied Aerodynamics Conference, Atlanta, GA. AIAA paper 2014-3141*.

Beri, H. and Yao, Y. (2011a). Effect of camber airfoil on self starting of vertical axis wind turbine. *J. Environ. Sci. Technol*, 4(3):302–312.

Beri, H. and Yao, Y. (2011b). Numerical simulation of unsteady flow to show self-starting of vertical axis wind turbine using Fluent. *Journal of Applied Sciences*, 11:962–970.

Bloor, M. S. (1964). The transition to turbulence in the wake of a circular cylinder. *Journal of Fluid Mechanics*, 19(02):290–304.

Bremseth, J. and Duraisamy, K. (2016). Computational analysis of vertical axis wind turbine arrays. *Theoretical and Computational Fluid Dynamics*, pages 1–15.

Chang, W., Giraldo, F., and Perot, B. (2002). Analysis of an exact fractional step method. *Journal of Computational Physics*, 180(1):183–199.

Chen, C.-C. and Kuo, C.-H. (2013). Effects of pitch angle and blade camber on flow characteristics and performance of small-size Darrieus VAWT. *Journal of Visualization*, 16(1):65–74.

Choi, H., Jeon, W.-P., and Kim, J. (2008). Control of flow over a bluff body. *Annu. Rev. Fluid Mech.*, 40:113–139.

Choi, J., Colonius, T., and Williams, D. R. (2015). Surging and plunging oscillations of an airfoil at low Reynolds number. *Journal of Fluid Mechanics*, 763:237–253.

Colonius, T. and Taira, K. (2008). A fast immersed boundary method using a nullspace approach and multi-domain far-field boundary conditions. *Computer Methods in Applied Mechanics and Engineering*, 197(25):2131–2146.

Corke, T. C. and Thomas, F. O. (2015). Dynamic stall in pitching airfoils: aerodynamic damping and compressibility effects. *Annual Review of Fluid Mechanics*, 47:479–505.

Dabiri, J. O. (2011). Potential order-of-magnitude enhancement of wind farm power density via counter-rotating vertical-axis wind turbine arrays. *Journal of Renewable and Sustainable Energy*, 3. 043104.

Dickinson, M. H., Lehmann, F.-O., and Sane, S. P. (1999). Wing rotation and the aerodynamic basis of insect flight. *Science*, 284(5422):1954–1960.

Dominy, R., Lunt, P., Bickerdyke, A., and Dominy, J. (2007). Self-starting capability of a Darrieus turbine. *Proceedings of the Institution of Mechanical Engineers, Part A: Journal of Power and Energy*, 221(1):111–120.

Dunne, R. and McKeon, B. J. (2014). Dynamic separation on a pitching and surging airfoil as a model for flow over vertical axis wind turbine blades. In *32nd AIAA Applied Aerodynamics Conference, Atlanta, GA. AIAA paper 2014-3142*.

Dunne, R. and McKeon, B. J. (2015a). Dynamic stall on a pitching and surging airfoil. *Experiments in Fluids*, 56(8):1–15.

Dunne, R. and McKeon, B. J. (2015b). A study of separation on airfoils undergoing combined pitch, surge and combined motions. In *33rd AIAA Applied Aerodynamics Conference, Dallas, TX. AIAA paper 2015-2882*.

Dunne, R., Tsai, H.-C., Colonius, T., and McKeon, B. J. (2015). Leading edge vortex development on pitching and surging airfoils: A study of vertical axis wind turbines. In *Int. Conf. Wake Jets Separated Flows, Stockholm, Sweden*.

Duraisamy, K. and Lakshminarayan, V. (2014). Flow physics and performance of vertical axis wind turbine arrays. In *32nd AIAA Applied Aerodynamics Conference, Atlanta, GA. AIAA paper 2014-3139*.

Ferreira, C. S., van Bussel, G., and Van Kuik, G. (2007). 2D CFD simulation of dynamic stall on a vertical axis wind turbine: verification and validation with PIV measurements. In *45th AIAA Aerospace Sciences Meeting and Exhibit/ASME Wind Energy Symposium*.

Ferreira, C. S., van Bussel, G. J., and van Kuik, G. A. (2006). Wind tunnel hotwire measurements, flow visualization and thrust measurement of a VAWT in skew. *Transactions-American Society of Mechanical Engineers Journal of Solar Energy Engineering*, 128(4):487.

Ferreira, C. S., van Kuik, G., van Bussel, G., and Scarano, F. (2009). Visualization by PIV of dynamic stall on a vertical axis wind turbine. *Experiments in Fluids*, 46(1):97–108.

Fiedler, A. and Tullis, S. (2009). Blade offset and pitch effects on a high solidity vertical axis wind turbine. *Wind Engineering*, 33(3):237–246.

Flinois, T. L. and Colonius, T. (2015). Optimal control of circular cylinder wakes using long control horizons. *Physics of Fluids (1994-present)*, 27(8). 087105.

Glezer, A. and Amitay, M. (2002). Synthetic jets. *Annual Review of Fluid Mechanics*, 34(1):503–529.

Greenblatt, D., Harav, A. B., and Mueller-Vahl, H. (2013). Mechanism of dynamic stall control on a vertical axis wind turbine. *AIAA paper 2013-851*.

Greenblatt, D. and Wygnanski, I. J. (2000). The control of flow separation by periodic excitation. *Progress in Aerospace Sciences*, 36(7):487–545.

Hansen, M. and Sresen, D. (2001). CFD model for vertical axis wind turbine. In *Wind Energy for the New Millennium-Proceedings of the European Wind Energy Conference, Copenhagen, Denmark*.

Hill, N., Dominy, R., Ingram, G., and Dominy, J. (2009). Darrieus turbines: the physics of self-starting. *Proceedings of the Institution of Mechanical Engineers, Part A: Journal of Power and Energy*, 223(1):21–29.

Hwang, I. S., Min, S. Y., Jeong, I. O., Lee, Y. H., and Kim, S. J. (2006). Efficiency improvement of a new vertical axis wind turbine by individual active control of blade motion. In *Smart Structures and Materials*, pages 617311–617311. International Society for Optics and Photonics.

Joe, W. T., Colonius, T., and MacMynowski, D. G. (2010). Optimized waveforms for feedback control of vortex shedding. In *Active Flow Control II*, pages 391–404. Springer.

Joe, W. T., Colonius, T., and MacMynowski, D. G. (2011). Feedback control of vortex shedding from an inclined flat plate. *Theoretical and Computational Fluid Dynamics*, 25(1-4):221–232.

Kim, D. and Choi, H. (2006). Immersed boundary method for flow around an arbitrarily moving body. *Journal of Computational Physics*, 212(2):662–680.

Kinzel, M., Mulligan, Q., and Dabiri, J. O. (2012). Energy exchange in an array of vertical-axis wind turbines. *Journal of Turbulence*, 13(1).

Kirke, B. K. (1998). *Evaluation of self-starting vertical axis wind turbines for stand-alone applications*. PhD thesis, Griffith University Cold Coast.

Langelaan, J. W. (2009). Gust energy extraction for mini and micro uninhabited aerial vehicles. *Journal of Guidance, Control, and Dynamics*, 32(2):464–473.

Lee, T. and Gerontakos, P. (2004). Investigation of flow over an oscillating airfoil. *Journal of Fluid Mechanics*, 512:313–341.

Lissaman, P. (1983). Low-Reynolds-number airfoils. *Annual Review of Fluid Mechanics*, 15(1):223–239.

Lissaman, P. (2005). Wind energy extraction by birds and flight vehicles. In *43rd AIAA Aerospace Sciences Meeting and Exhibit, Reno, NV. AIAA paper 2005-241*.

McCroskey, W., Carr, L., and McAlister, K. (1976). Dynamic stall experiments on oscillating airfoils. *AIAA Journal*, 14(1):57–63.

Mertens, S., van Kuik, G., and van Bussel, G. (2003). Performance of an H-Darrieus in the skewed flow on a roof. *Transactions-American Society of Mechanical Engineers Journal of Solar Energy Engineering*, 125(4):433–440.

Michael, S., Eberhard, B., and Peter, A. M. (1994). Self-excited oscillations in the wake of two-dimensional bluff bodies and their control. *Journal of Fluid Mechanics*, 271:17–53.

Morris, W. J. and Rusak, Z. (2013). Stall onset on aerofoils at low to moderately high reynolds number flows. *Journal of Fluid Mechanics*, 733:439–472.

Nobile, R., Vahdati, M., Barlow, J., and Mewburn-Crook, A. (2011). Dynamic stall for a vertical axis wind turbine in a two-dimensional study. *Wind Energy Applications*, 15:4225–4232.

Nocedal, J. and Wright, S. (2006). *Numerical optimization.* Springer Science & Business Media.

Paraschivoiu, I. and Allet, A. (1988). Aerodynamic analysis of the Darrieus wind turbines including dynamic-stall effects. *Journal of Propulsion and Power*, 4(5):472–477.

Paraschivoiu, I. and Beguier, C. (1998). Visualization, measurements and calculations of dynamic stall for a similar motion of VAWT. In *Proceedings of the European Wind Energy Conference, Herning, Denmark.*

Paraschivoiu, I., Trifu, O., and Saeed, F. (2009). H-Darrieus wind turbine with blade pitch control. *International Journal of Rotating Machinery*, 2009.

Pawsey, N. C. K. (2002). *Development and evaluation of passive variable-pitch vertical axis wind turbines.* PhD thesis, The University of New South Wales.

Peng, Z. and Zhu, Q. (2009). Energy harvesting through flow-induced oscillations of a foil. *Physics of Fluids (1994-present)*, 21(12). 123602.

Peskin, C. S. (1972). Flow patterns around heart valves: a numerical method. *Journal of Computational Physics*, 10(2):252–271.

Pinier, J. T., Ausseur, J. M., Glauser, M. N., and Higuchi, H. (2007). Proportional closed-loop feedback control of flow separation. *AIAA Journal*, 45(1):181–190.

Polak, E. (1970). *Computational methods in optimization: A unified approach.* Academic Press.

Raju, R., Mittal, R., and Cattafesta, L. (2008). Dynamics of airfoil separation control using zero-net mass-flux forcing. *AIAA Journal*, 46(12):3103–3115.

Roh, S.-C. and Kang, S.-H. (2013). Effects of a blade profile, the reynolds number, and the solidity on the performance of a straight bladed vertical axis wind turbine. *Journal of Mechanical Science and Technology*, 27(11):3299–3307.

Roma, A. M., Peskin, C. S., and Berger, M. J. (1999). An adaptive version of the immersed boundary method. *Journal of Computational Physics*, 153(2):509–534.

Shewchuk, J. R. (1994). An introduction to the conjugate gradient method without the agonizing pain. Technical report, CMU-CS-94-125, Department of Computer Science, Carnegie-Mellon University.

Siegel, S. G., Cohen, K., and McLaughlin, T. (2006). Numerical simulations of a feedback-controlled circular cylinder wake. *AIAA journal*, 44(6):1266–1276.

Strykowski, P. and Sreenivasan, K. (1990). On the formation and suppression of vortex 'shedding' at low Reynolds numbers. *Journal of Fluid Mechanics*, 218:71–107.

Taira, K. and Colonius, T. (2007). The immersed boundary method: a projection approach. *Journal of Computational Physics*, 225(2):2118–2137.

Taira, K., Rowley, C. W., and Colonius, T. (2010). Feedback control of high-lift state for a low-aspect-ratio wing. In *48th AIAA Aerospace Sciences Meetings, Orlando, FL, AIAA Paper 2010-357*.

Tokumaru, P. and Dimotakis, P. (1991). Rotary oscillation control of a cylinder wake. *Journal of Fluid Mechanics*, 224:77–90.

Tsai, H.-C. and Colonius, T. (2014). Coriolis effect on dynamic stall in a vertical axis wind turbine at moderate Reynolds number. In *32nd AIAA Applied Aerodynamics Conference, Atlanta, GA. AIAA paper 2014-3140*.

Tsai, H.-C. and Colonius, T. (2016). Coriolis effect on dynamic stall in a vertical axis wind turbine. *AIAA Journal*, 54(1):216–226.

Untaroiu, A., Wood, H. G., Allaire, P. E., and Ribando, R. J. (2011). Investigation of self-starting capability of vertical axis wind turbines using a computational fluid dynamics approach. *Journal of Solar Energy Engineering*, 133(4). 041010.

Wang, S., Ingham, D. B., Ma, L., Pourkashanian, M., and Tao, Z. (2010). Numerical investigations on dynamic stall of low Reynolds number flow around oscillating airfoils. *Computers & Fluids*, 39(9):1529–1541.

Williams, D. R., Kerstens, W., and Quach, V. (2011). Drag-power measurements of a plunging wing in an oscillating freestream. In *41st AIAA Fluid Dynamics Conference and Exhibit, Honolulu, HI*.

Zhu, Q. (2011). Optimal frequency for flow energy harvesting of a flapping foil. *Journal of Fluid Mechanics*, 675(20):495–517.

Zhu, Q. and Peng, Z. (2009). Mode coupling and flow energy harvesting by a flapping foil. *Physics of Fluids (1994-present)*, 21(3). 033601.